MODELLING TUBULAR BRAIDED COMPOSITES USING GEOMETRICAL, MICRO-COMPUTED TOMOGRAPHY, AND FINITE ELEMENT ANALYSIS METHODS

Ali Gholami

A DISSERTATION SUBMITTED TO
THE FACULTY OF GRADUATE STUDIES
IN PARTIAL FULFILLMENT OF THE REQUIREMENTS
FOR THE DEGREE OF
DOCTOR OF PHILOSOPHY

GRADUATE PROGRAM IN MECHANICAL ENGINEERING
YORK UNIVERSITY
TORONTO, ONTARIO

February 2024

Abstract

This thesis investigates various modelling approaches for two-dimensional Tubular Braided Composite (TBC) structures. Because of TBCs' flexible nature, modelling them properly is challenging and usually involves some assumptions. However, having an accurate modelling procedure would help researchers and industries obtain more accurate simulation results before manufacturing or using TBCs. In this research, the gap in the modelling of TBCs will be addressed.

Some equations are available in the literature to generate geometrical models of TBCs. However, the intricate nature of the equations involved makes creating accurate geometrical models challenging. This research introduces a user-friendly and open-source software, TBC-Gen, which streamlines the modelling process, eliminating the need for extensive knowledge of the underlying equations. Moreover, some modifications have been applied to the equations to enhance the precision of TBC simulations. Comparative analyses are conducted between TBC-Gen outputs, results from other software, and physical TBC samples to investigate the accuracy of the TBC-Gen results.

Micro-computed tomography (μCT) proves to be a precise method for scanning TBCs. This study employs μCT to scan various TBCs with different patterns, dimensions, and materials. Different image processing techniques have been developed to extract essential parameters (minor and major yarn and mandrel diameter, center point, orientation, and cross-sectional area of yarns) from the scanned models. Also, an innovative segmentation and splitting algorithm is implemented for overlapping yarns. Subsequently, two yarns from the scanned TBCs are extracted, and their paths are plotted. A simulated yarn path is fitted to the extracted path, and a new parameter is introduced

to the geometrical model to enhance the fitness of the yarn paths. The error between the fitted geometrical model and the segmented yarn path is less than 1%.

The TBC-Gen program is then utilized to design different geometrical models, and Finite Element Simulations (FEM) are developed to analyze their behaviour under tensile tests. Periodic Boundary Conditions (PBC) are applied to optimize computational efficiency. The impact of braid angle on TBC displacement during tensile testing is investigated by simulating seven models with similar geometries but varying braid angles (30°-70°). Additionally, three TBCs with similar geometries but different patterns are simulated, and their displacements are reported. The result shows that the displacement of simulated TBCs increases as the braid angle increases. Also, the Hercules pattern shows the most displacement and the Diamond pattern shows the least displacement under a similar tensile test. The FEM results are further validated by simulating the setup of an experimental test and comparing the outcomes against both experimental and Classical Laminate Plate Theory (CLPT) results. The FEM results are closer than the CLPT results to the experimental results.

This comprehensive research not only advances TBC modelling methodologies but also validates their accuracy through a combination of advanced imaging techniques, innovative algorithms, and rigorous simulations, contributing valuable insights to the field of composite materials. The TBC-Gen program developed in this study can help other researchers and industries generate geometrical models without a deep understanding of the details of the equations. It can also be used for educational and visualization purposes.

Acknowledgement

I would like to express my sincere gratitude to my supervisor and mentor, Professor Garrett Melenka, for the unwavering support and invaluable guidance throughout the challenging journey of my Ph.D. Professor Melenka's expertise, encouragement, and commitment have been instrumental in shaping the trajectory of my research and academic endeavours.

I am deeply thankful to the members of my doctoral committee, Professor Aleksander (Alex) Czekanski and Professor Zheng Hong (George) Zhu, for their insightful feedback, constructive criticism, and scholarly input that significantly enriched the quality of my thesis. Their collective expertise has been crucial in refining the depth and breadth of my work.

I extend my heartfelt thanks to my colleagues and fellow researchers at Melenka Lab, who have shared their expertise, ideas, and feedback. Their collaborative spirit has fostered a supportive academic community that has enhanced the overall research experience.

Lastly, my deepest appreciation goes to my family and friends for their unwavering encouragement, understanding, and patience throughout this academic journey. Their emotional support has been a source of strength, motivating me to overcome challenges and persevere in my pursuit of knowledge.

Table of Contents:

List of Tables

List of Figures

Chapter 1. Introduction

1.1 Research Motivation

This research focuses on investigating 2D Tubular Braided Composites (TBCs), an area that has received limited attention compared to its 3D counterparts. Existing literature primarily emphasizes 3D braided composites, leaving a notable gap in understanding 2D braids despite their commonality and accessibility.

An open-source software named TBC-Gen will be introduced in this research. Researchers and industries can use TBC-Gen to easily and quickly generate geometrical models of TBCs. Another contribution of this research is developing a Finite Element modelling (FEM) of braided composites where the effect of geometrical variables and the patterns of the TBCs on the mechanical properties of the TBCs are studied. Also, the geometry of manufactured TBCs is studied comprehensively by scanning them by a μCT device. Different image processing techniques have been developed in this research to extract the data from the scanned images. The extracted data from μCT images are compared against geometrical models, and the existing error is reported.

Current equations for generating braided composites are complex and require a thorough understanding of braids and associated variables. Some equations in the literature inaccurately represent the actual patterns of braided composites, necessitating modification. To address this gap, this research aims to develop a user-friendly, open-source application with refined mathematical equations for improved precision in representing actual models.

While geometrical models for TBCs have been proposed, the literature lacks reported accuracy assessments. Researchers using these equations need more certainty about how accurately the models represent TBCs. Recognizing this, the current study comprehensively examines the error between micro-computed tomography (μCT) and the mathematical yarn path of the braided composite, providing valuable insights into model inaccuracies. The goal is to empower researchers with a clearer understanding of existing models' precision and limitations, aiding informed decision-making in their application.

The μCT models of TBCs contain valuable information that can be analyzed using various image-processing techniques. Extracting parameters such as the cross-section area of yarns, mandrel diameter, yarn diameters, center point, orientations, and yarn count in each braided composite is essential. Due to braided composites' complex and flexible nature, segmenting overlapping yarns in cross-section images is often challenging, necessitating a segmentation process. This research focuses on extracting yarn and braided composite parameters, including developing a segmentation algorithm for specific cases.

Utilizing the Finite Element Method (FEM) for 2D TBCs enhances individuals understanding of these materials' behaviour. FEM, based on modified geometrical models, serves as a robust tool for analyzing TBC performance under varying conditions. This study involves the development of diverse FEM simulations for TBCs with different sizes and patterns, exploring the impact of braided composites and braid patterns under tensile tests. The results of these FEM simulations are compared with experimental and analytical data for validation.

1.2 Thesis Objectives

This research aims to investigate modelling methods for TBCs. Geometrical modelling methods will be assessed, and a user-friendly program will be introduced for modelling purposes. Additionally, μCT methods will be employed to generate experimental models, with various image processing techniques utilized to extract parameters. A Finite Element Method (FEM) simulation will be developed to simulate the behaviour of TBCs under different conditions. The project has three objectives outlined below, aligning with the overall research goal.

Objective 1: ***Create an open-source, user-friendly program for generating precise geometrical models using equations that describe the overall form of TBCs***: in this objective, the geometrical model equations will be modified so that they will follow the actual TBC models. Then, an easy-to-use program will be developed, and the edited equations will be incorporated. The program will be designed under MATLAB software packages, and it does not require the user to have significant knowledge about the modelling equations of the TBCs.

Objective 2: ***Conduct a thorough error analysis of TBC model yarn paths. Generate experimental models using μCT and compare their yarn paths with the corresponding mathematical models. Also, analyze the μCT models and extract their parameters using an image processing technique.*** In this objective, the models generated by μCT will be examined by different software and image processing techniques, and yarn paths of yarns will be extracted. The yarn path of a TBC with similar geometry will be generated using the program developed in the previous objective. An objective function will be defined between the μCT yarn path and the simulated yarn path to optimize the parameters that will minimize the Mean Square Error (MSE) between these two models. A new parameter will be defined and incorporated into the equations to improve the fitness of the simulated yarn path. The Particle Swarm Optimization (PSO) will be used to optimize the parameters of the fitted yarn. The parameters that minimize the MSE are the optimized parameters, and the relevant MSE will be reported. The reported MSE will give a better understanding of the accuracy of the geometrical model and the amount of incorporated error in the geometrical models.

Objective 3: ***Develop Finite Element Models for TBCs with different geometry and patterns based on geometrical models developed in objective one and verify the results.*** This objective aims to create simulation models for various TBCs and investigate their behaviour under different conditions. Geometrical models necessary for FEM simulations will be generated using the program developed in Objective 1. Diverse TBCs, characterized by distinct geometrical parameters and patterns, will be created and subjected to simulation.

A tensile test will be designed to ensure accuracy, and an optimal mesh size will be determined through a systematic mesh study. Additionally, implementing Periodic Boundary Conditions (PBC) will be explored to enhance computational efficiency. The focus will be on assessing the impact of the braid angle, a critical geometrical parameter in TBCs, on the displacement observed during a tensile test. Various TBCs with differing braid angles will be simulated to examine this effect. Furthermore, different TBC patterns will be simulated to investigate their influence on displacement.

The simulation results will be compared with experimental findings and analytical results from relevant studies, comprehensively evaluating the simulated models.

1.3 Thesis Outline

To attain the objectives above, the thesis is structured into seven chapters. Chapter 2 delves into an extensive review of current literature on 2D, and 3D braided composite materials, examining relative geometrical models, the application of the µCT method in composite materials and other fields, as well as the Finite Element Method (FEM) and analytical modelling of composite materials and related areas of study.

Chapter 3 focuses on generating geometrical models for 2D TBCs. Various patterns of TBCs are introduced, accompanied by the equations necessary for modelling each pattern and its parameters. The chapter presents an accessible application, TBC-Gen, designed to create these geometrical models without requiring users to possess detailed knowledge of TBCs. Sample models featuring diverse geometrical variables and sizes are presented, and the results produced by TBC-Gen are compared with those from other software. A version of this Chapter was published and presented as: *Gholami, Ali, and Garrett W. Melenka. "Generating geometrical models for tubular braided composites." CSME Conf. Charlottetown, PE, Canada. 2021*.

Chapter 4 outlines the segmentation of yarns from both simulated and µCT models. A simulated geometrical model is generated using the TBC-Gen software, and its cross-sectional images are analyzed for yarn segmentation. Various algorithms for segmenting single and overlapping yarns are introduced. The chapter also analyzes cross-section images from a µCT-scanned TBC, applying segmentation algorithms and extracting yarn paths. A version of this Chapter was published and presented as: *Gholami, Ali, and Garrett W. Melenka. "Extracting parameters of µCT scanned open mesh tubular braided composite materials' yarn using image processing techniques" CSME Conf. Sherbrooke, QC, Canada. 2023*.

In Chapter 5, revised equations for designing TBCs are presented. The segmentation algorithms developed in Chapter 4 are employed to extract clockwise and counterclockwise yarn paths from µCT-scanned TBCs. Mandrel diameter and braid angle are extracted using new algorithms, and an inverse problem is formulated to fit a simulated yarn path to the extracted path. Particle Swarm Optimization (PSO) algorithms are employed to solve the inverse problem, with the Mean Squared Error (MSE) between the two yarn paths reported as a fitness metric. A version of this Chapter was published as: *Gholami, Ali, and Garrett W. Melenka. "Studying the geometrical models of* *tubular braided composite using micro-computed tomography and particle swarm optimization." Composites Part B: Engineering 260 (2023): 110758.*

Chapter 6 focuses on the development and presentation of Finite Element Modeling (FEM) for TBCs. The TBC-Gen generates simulated geometrical models, and a mesh study determines the optimal mesh size. Periodic Boundary Conditions (PBC) are applied. Seven TBCs with similar geometrical properties are designed with varying braid angles. FEM simulations conducted in COMSOL Multiphysics include a tensile test, revealing the effect of braid angle on displacement.

Additionally, three TBCs with different patterns but similar geometrical properties undergo simulation to study the pattern type's impact on displacement. The chapter concludes with a comparison of FEM results against experimental and analytical models. A version of this Chapter was published as: *Gholami, Ali, and Garrett W. Melenka. "Finite element analysis of 2-D tubular braided composite based on geometrical models to study mechanical performances." Mechanics of Advanced Materials and Structures 29.28 (2022): 7542-7558.*

Chapter 7 summarizes and concludes the research outcomes. It also explores potential future avenues for research as the next steps in this field.

Chapter 2. Literature Review

2.1 Introduction to Composite Materials

Composite materials constitute two or more materials combined with different mechanical properties. The combination of these materials provides improved mechanical properties from individual materials. One of these materials is the reinforcing component, and the other is called the matrix. Common reinforcing materials are fibers, particles, or flakes, while matrix materials are usually continuous. Common examples of composite materials are concrete reinforced with steel bars, epoxy reinforced by graphite fibers, two thin skins of metal bonded to a plastic core creating a sandwich panel, composite honeycombs, etc. Composite materials are not limited only to synthetic materials. Natural composite materials are like woods, where the lignin matrix is reinforced by fibers or bones, bone-salt plates play the reinforcing phase, and the soft collagen is the matrix [1]. Because of the unique characteristics that composite materials can obtain, they are preferred in advanced industries such as aerospace. The improved unique characteristics may include strength, stiffens, fatigue, impact resistance, thermal conductivity, and corrosion resistance.

Carbon fiber, fiberglass, Kevlar, quartz, and polyester are commonly used in composite material manufacturing as reinforcing materials. Thermal set resins such as polyester, vinyl ester, epoxy, polyurethane, and phenolic are also used as matrices in composite materials. The fiber-to-resin ratio can be between 80/20 and 70/30, where the optimal ratio can be selected based on the need and application of the desired composite material. The higher the fiber content in the composite, the higher the strength and stiffness [2].

The composite materials consist of many advantages: [3], [4]

- **High Strength-to-Weight Ratio**: Composite materials are known for their exceptional strength-to-weight ratio. They offer a combination of lightweight properties with high strength, allowing for the construction of strong and durable structures significantly lighter than those made from traditional materials. This advantage is particularly valuable in industries such as aerospace, automotive, and sports equipment manufacturing, where weight reduction is critical for enhanced performance and fuel efficiency.
- **Tailored Mechanical Properties**: Composite materials can customize and tailor their mechanical properties to meet specific application requirements. By selecting different combinations of fibers and matrices, engineers can design composites with desired characteristics such as tensile strength, stiffness, and impact resistance. This flexibility allows for optimizing material properties and improving performance and functionality in various fields.
- **Corrosion and Chemical Resistance**: Unlike metals, which are prone to corrosion and chemical degradation, composite materials exhibit excellent resistance to these environmental factors. This advantage makes composites suitable for applications in aggressive environments such as marine, chemical processing, and offshore industries. By using composites, companies can achieve longer service life, reduced maintenance costs, and increased durability of structures.
- **Design Flexibility**: Composite materials offer immense design freedom because they can be moulded into complex shapes and structures. This flexibility allows engineers to create components that are not easily achievable with traditional materials. Utilizing techniques like filament winding, resin infusion, or automated lay-up processes, composites can be

formed into intricate geometries, improving functionality, streamlined aesthetics, and optimized performance.

- **Fatigue and Impact Resistance**: Composites possess excellent fatigue and impact resistance properties. They can absorb and dissipate energy upon impact, making them ideal for applications that require impact resistance, such as automotive bumpers, aircraft structures, and sporting goods. The fatigue resistance of composites also allows for prolonged service life under cyclic loading conditions, reducing the need for frequent maintenance and replacement.
- **Thermal and Electrical Insulation**: Certain composite materials exhibit excellent thermal and electrical insulation properties. This advantage is valuable in applications where electrical conductivity needs to be controlled or heat dissipation or insulation is required. Composites can insulate electrical components, circuit boards, and high-temperature environments, ensuring safety and optimal performance.
- **Environmental Sustainability**: Composite materials offer environmental advantages, making them increasingly attractive in today's eco-conscious world. They often require fewer raw materials during manufacturing than traditional materials, reducing energy consumption and lowering carbon footprint. Furthermore, advancements in composite recycling technologies enable the recovery and reuse of constituent materials, promoting a more sustainable and circular economy.

Braided composites can be manufactured in two-dimensional (2D) and three-dimensional (3D) forms. In 2D braided composites, only two sets of yarns are woven around the mandrel's axis, and there is no yarn in the other direction. However, in 3D braided composites, there is an additional yarn in the direction of the mandrel radios [4]. Figure 2-1 shows a sample of 3D and 2D composite material.

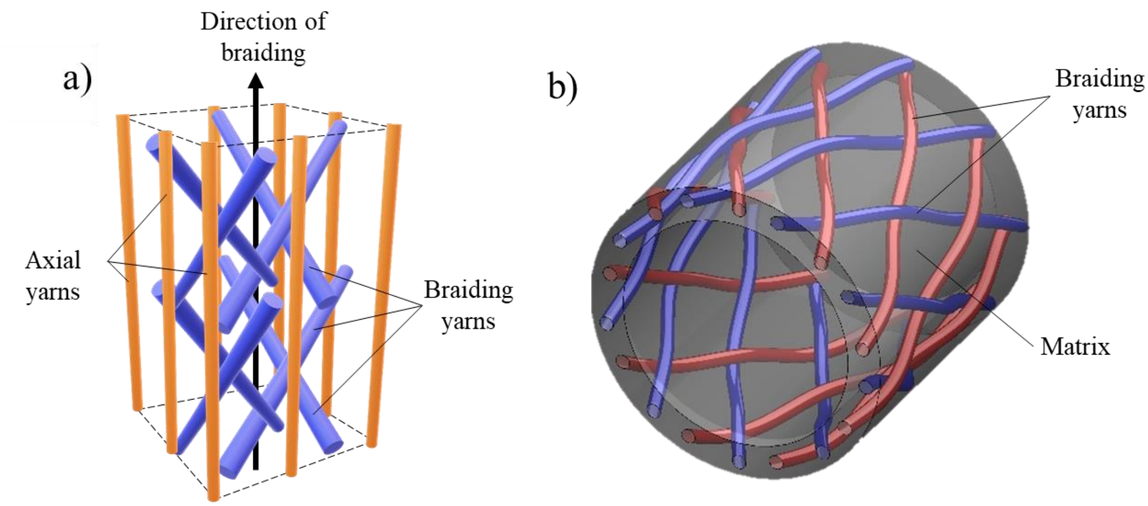

Figure 2-1 A sample of braided yarn. a) a 3D braided composite, b) a 2D Tubular braided composite

This chapter presents an academic literature review about braided composites and their modelling methods. An introduction will encompass the various types of tubular braided composites (TBCs) and their distinctive characteristics. Subsequently, the chapter will comprehensively examine different geometrical models applied to TBCs. Following this, the use of Micro Computed Tomography (μCT) in braided composites will be explored, focusing on its applications. Moving forward, the discussion will shift toward the literature on Finite Element Method (FEM) analyses concerning braided composites, encompassing analytical methods employed in studying these materials. A thorough assessment of FEM models based on μCT data across various industries will also be conducted. Towards the conclusion, the findings and insights extracted from the reviewed works will be synthesized, and gaps in the current body of literature will be highlighted.

2.2 Braided Composites

Braided composites are continuous fiber-based reinforced materials which are used in various industries, from aerospace, automotive, petroleum and building to medical treatments, sporting and marine (poles and boom, winch drums and shafting, etc.) [5]–[7]. For more than 200 years, braiding has been used to produce textile fabrics [5]. Braided composites have significant advantages compared to conventional laminate composites, such as better out-of-plan stiffness, strength, toughness properties, net shape fabrication, lower fabrication cost, impact and delamination resistance, and high performance [8][9].

The application of braided composites has matured significantly, and as a result, many studies have been done to facilitate the manufacturing process and increase the efficiency of braided composites. There are different types of braided composite: two-dimensional, three-dimensional, and multidirectional, and they can be produced as flat or tubular shapes. In two-dimensional braided composites, yarns are interlaced only in one plane, and the preform can be manufactured flat or tubular. In a triaxial two-dimensional braided composite, additional yarns are interwoven between two-dimensional braids and directed alongside the axial braided composite [10].

Like all kinds of composite materials, braided composites consist of two parts: reinforcement material known as fibers and binding material known as matrix. Also, the fibrous structure before resin impregnation is known as a preform. The combination of these two materials provides the condition neither can provide individually. Strength, stiffness, toughness, damage resistance, wear resistance, corrosion resistance, fatigue life and thermal insulation are properties that are improved once materials are used as a composite material. Some of the mentioned improvements can be made by changing the design and properties of composite materials [10].

Another form of composite is laminate composite, in which layers of fibrous composite materials are joined to provide the designed properties. Braided composites are tougher than laminate composites because of braided composites' interlaced structures [11]. However, braid composites have lower in-plane strength, specifically in the braid direction, because of the undulation in the braid fiber paths [12].

2D braided composites can be produced using a Maypole braider. One way to categorize braided composites is based on the assembly pattern of yarns. Different patterns of braided composites will be made depending on the arrangement and movement of carriers. In all braided composite patterns, there is a repeating pattern known as a representative or repeating unit cell that distinguishes braiding types from each other.

The patterns of the braided composites are diamond (one tow passing above and then below the other tows, 1/1), regular (two tows passing above and then below the other tows, 2/2), Hercules (three tows passing above and then below the other tows 3/3), and triaxial. Different forms of braided composites are shown in Figure 2-2. In addition, braided composites are produced in open and closed mesh configurations. Open-mesh configurations have a low fiber volume fraction (total volume percentage of fiber in the structure) because of large neat (pure) resin areas. While in closed-mesh configurations, the yarns are touching each other, and there is no space between them. Another critical manufacturing variable is the braid angle. The braid angle is each yarn's angle with the braid's longitudinal axis. Different braid angles may result in various mechanical properties, such as longitudinal elastic, transverse, and shear modulus. In addition to braid angle, width, height, and undulation length are other geometrical parameters affecting braided composites' shape and mechanical properties [6]. A unit cell of a regular braided composite and geometrical parameters are shown in Figure 2-3.

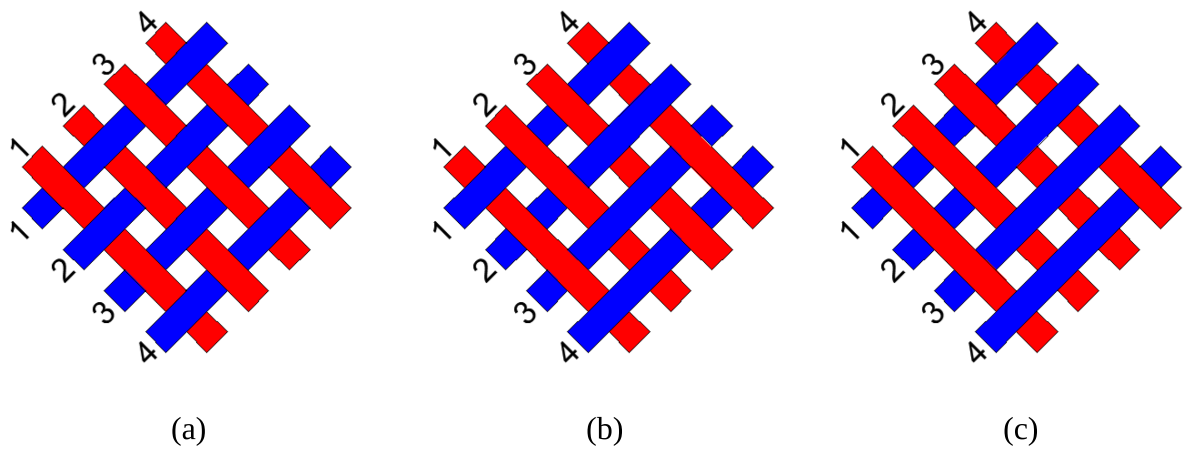

Figure 2-2 Different patterns of braided composite (a): Diamond (one by one), (b): Regular (two by two), (c) Hercules (three by three)

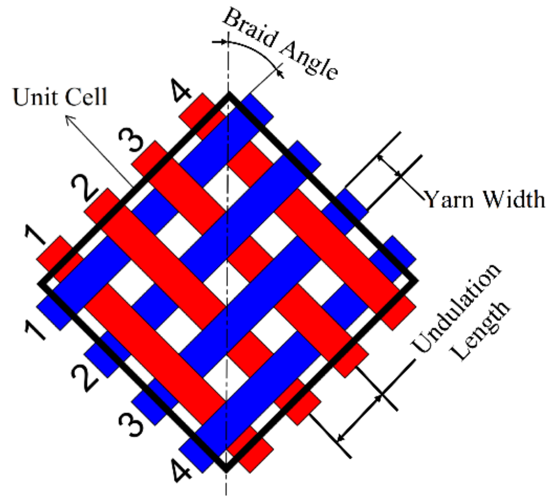

Figure 2-3 Geometrical variables of a TBC's Regular (2x2) unit cell.

The braid angle (θ) is the most important and sensitive among all the geometrical parameters. Researchers have shown that the braid angle directly affects the properties of the braided composites. The increase in the braid angle causes an increase in the thickness of the braided tows, which will increase the thickness of the TBC [13]–[15].

Depending on mandrel diameter, width of yarns and number of yarns, the braid angle of the preform would be different. Each preform has a range in which the braid angle can change by changing parameters. However, there is a lower and upper limit for this range known as tension and compression jam angle, which means the braid angle cannot change anymore in that direction. Using Equation 2-1, the jam angle can be calculated [10].

$$\cos(\theta_{jammed}) = \frac{W_y \sin(\gamma)}{2R_m \sin\left(\frac{2\pi \sin(\gamma)}{N_c}\right)} \quad \text{Equation 2-1}$$

where, W_y is the yarn width, γ is the half-cone angle between the braid guide ring and deposition plan, R_m is the mandrel radius and N_c is the number of yarn carriers. The plots of the jam angle of four braids with different yarn widths are shown in Figure 2-4 a). In this figure, the plots of jam angles for four different yarn widths are plotted. The horizontal axis shows the diameter of the braid, and the vertical axis shows the angle. For example, the jam angle of a braid with a diameter of braid = 20 mm and the yarn width = 2 mm is 58°. Figure 2-4 b) and c) show a Regular unjammed TBC and a jammed braid TBC, respectively. The unjammed TBC is known as open-mesh TBC, too, as there is an open space between yarns. Similarly, the jammed TBCs are known as closed-mesh TBCs, where yarns touch each other.

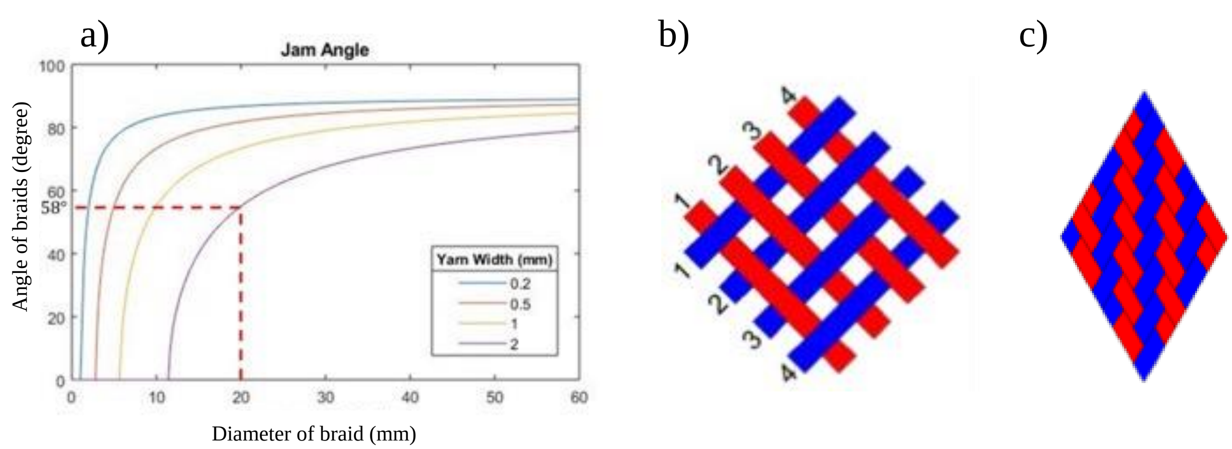

Figure 2-4 a) The plot of the Jammed angle of four TBCs, b) a Regular unjammed (open-mesh) TBC, c) a jammed (closed-mesh) TBC.

2.3 Geometrical Modelling of Braided Composites

Creating the geometrical model of TBCs is a challenging task because of its flexible and soft nature. Figure 2-5 shows a 3D model of a 2D TBC created by µCT. As one can see from this figure, the location of yarns is not in their ideal shape, and they are distorted. Because of the flexible nature of yarns and the manual process of manufacturing these composites, these distortions are widespread, making it harder to model them.

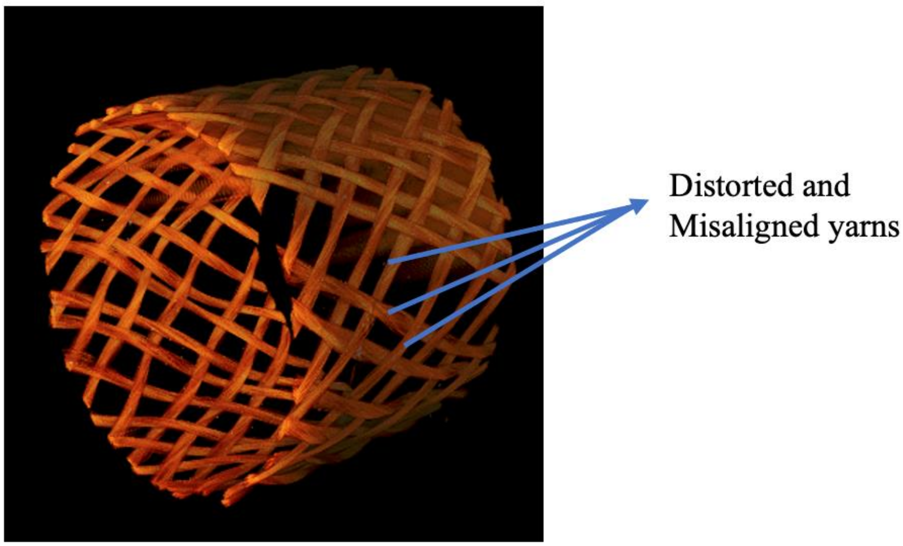

Figure 2-5 A 3D model of a 2D TBC created by µCT. The yarns are distorted and are not in their ideal shape because of TBC's flexible nature.

Liao and Adanur [16] developed a geometric model for woven and braided structures in 3D space. These authors used the Computer Aided Geometric Design (CAGD) technique to generate the models. This research swept a simple 2D cross-section along a 3D yarn path. These models were developed using C++ and OpenGL in Diamond and Regular patterns. This research does not discuss the procedure for computing the coordinates of the yarn paths.

TBCs have several variables, such as variable geometry, variable constituents (fibers and matrix materials), and the non-uniform feature of braided composites. The modelling of braided composites is not straightforward due to the numerous variables that define their construction. Also, the available equations are usually too complicated to be used and need to be updated to better pertain to the patterns of TBC.

Tate et al. [17] studied the braid angle's effect on the fatigue performance of Regular biaxial carbon/epoxy braided composites. They used static tests to evaluate the tensile strength, modulus, and Poisson's ratio of the braided composites. Finally, they conclude that tensile properties are sensitive to the braid angle. Once the braid angle was altered from 25 degrees to 45 degrees, the percentage in ultimate tensile strength (UTS), tensile modulus, and Poisson's ratio decreased by 75%, 70%, and 96%, respectively.

Several studies have tried to provide more mathematically accurate models for tubular braided composites. Alpyildiz [18] proposed a 3-D geometrical model for tubular braids. The author considered the braiding yarn's crimp and the tubular braid structure's curvature in the model. The provided model worked with different braid structures, braid angles, the number of yarns in a set, yarn, and mandrel diameter.

However, there are several assumptions in the simulated model used in Alpyildiz's research, and they are as follows:

- Yarns are assumed to be non-compressible and have a uniform elliptical cross-section through the whole path on the braided composites.
- It is assumed that the undulation path of the yarn braids follows a sinusoidal curve, and along the yarn length, they follow a helical path with the radius of r_0 around the mandrel with the radius of R.
- It is assumed that no yarn slippage is in the structure of braiding yarns.

Rawal et al. [19] developed geometrical models in both cylindrical and conical mandrels with diamond, regular and triaxial forms. They used the Virtual Reality Modeling Language (VRML) to simulate the model. Finally, the model was verified against the results of a virtual experiment.

Melenka et al. [15] provided a geometrical model that can create different patterns of TBC. This model is generated based on the manufacturing process of TBCs. The authors also use these models to develop an analytical model to calculate the elastic properties of the TBCs with different patterns. Finally, the results of the analytical model were compared against FEM and Experimental results.

Kyosev [20] provided an overview of the 3D modelling of braided structures. In this research, different studies in the field of modelling of TBCs are reviewed, and their advantages and gaps are discussed. The author reports that the models reported in [16], [18], [19] are not feasible to manufacture by any "classical normal" maypole braiding machine with horn gears. The models have considered the orientation of the ridges to be perpendicular to the product axis. However, in manufacturing machines, the orientation of ridges should be parallel to the product axis.

In the above research done to develop a geometrical model for TBCs that could capture all three patterns, some gaps need to be addressed:

- The cross-section of the TBCs is assumed to be a specific shape (ellipse or circle), and they do not change along the yarn path. However, in reality, the TBC does not follow a regular shape, and the yarn paths are usually distorted due to the flexible nature of the TBCs.
- In the models, it is assumed that the orientation of ridges is perpendicular to the axis of the TBC. When looking at the cross-section images of models created by these methods, all the clockwise or counterclockwise yarns stand either on the cross-section's inner or outer

side. However, the clockwise and contour clockwise yarns change their position from the inner side to the outer side throughout the cross-section.

- Creating these models is complicated and requires the user to define model geometries. Therefore, an easy-to-use program is necessary to let users develop their models with different variables and patterns easily and quickly.

2.4 Micro-Computed Tomography in Braided Composites

Different methods can be used to generate geometrical models of TBC. One method is creating geometrical models using mathematical equations. The advantages of this method are its rapid process and low cost for developing different models. However, the main disadvantages of this method are that it assumes that the yarns are in perfect shape and ignores distortion of them. Also, the cross-section of the yarns is assumed to have a regular shape, ignoring the compression of the yarns.

Photomicrography is a method used to capture photographs through a microscope, enabling the generation of TBC models. Byun [19] utilized photomicrography to predict the TBC's geometrical characteristics and three-dimensional engineering constants. The crimp yarn angle and fiber-volume fraction were derived from the geometrical model and compared with experimental test results in this research. However, this method has limitations, as it only provides 2D cross-sectional images of the braided composite and cannot generate 3D models or scan the internal structures of the material.

One powerful tool to analyze braided composites is micro-computed tomography (μCT). It can obtain comprehensive geometrical information such as the fiber tows, detailed information about the structure of the braids, inner and surface voids, individual fibers and fiber coatings geometry of braided composites. μCT is a non-destructive imaging method that can acquire high-resolution three-dimensional images. The 3-D model created in μCT is based on sticking cross-sectional images up to each other. The reconstructed μCT scanned images are created of small 3-D volume elements known as voxels. In μCT scans, the minimum voxel size can be as low as 0.1 μm [23].

In μCT tests, the sample is placed between the X-ray source and the X-ray detector. As a result, the sample will attenuate part of the X-ray sent to the detector. The X-ray's attenuation depends on the sample's density and thickness. In other words, the denser the sample, the more X-ray attenuation. Therefore, fewer X-rays will pass to the detector, making the relevant section of the recorded image darker. In the μCT test, the sample holder can turn with a predefined step size and be moved vertically to scan different sample sections. The images are then imported into an image processing software to create the cross-sectional images alongside a 3-D model of the scanned sample. The schematic of the μCT test is shown in Figure 2-6 [24].

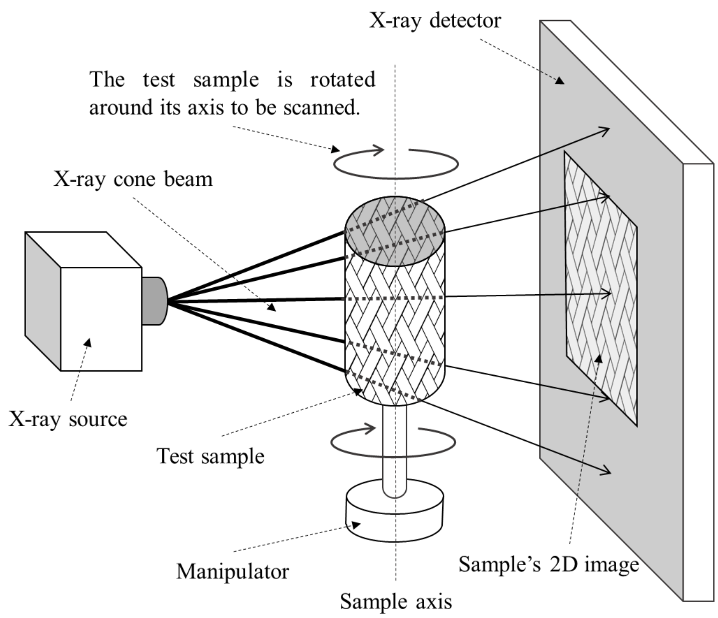

Figure 2-6 The fundamental schematic of the micro-CT test used for scanning the tubular braided composite.

In a μCT test, based on the density of the test piece, part of the X-ray is attenuated and moves toward the detector. The following equation measures the diminished arrays: [24]

$$I_x = I_0 e^{-\mu x} \quad \text{Equation 2-2}$$

where I_0 is the incident X-ray intensity, x is the material thickness, and μ is the linear attenuation coefficient (LAC) in cm^{-1} and its value depends on the X-ray energy and atomic number of the scanned material. The attenuation of the X-ray transmitted through a material is shown in Figure 2-7. As one can see from this figure, the initial X-rays will be attenuated exponentially as they go through the thickness of the material. The thicker and denser the material, the less energy transmitted through it.

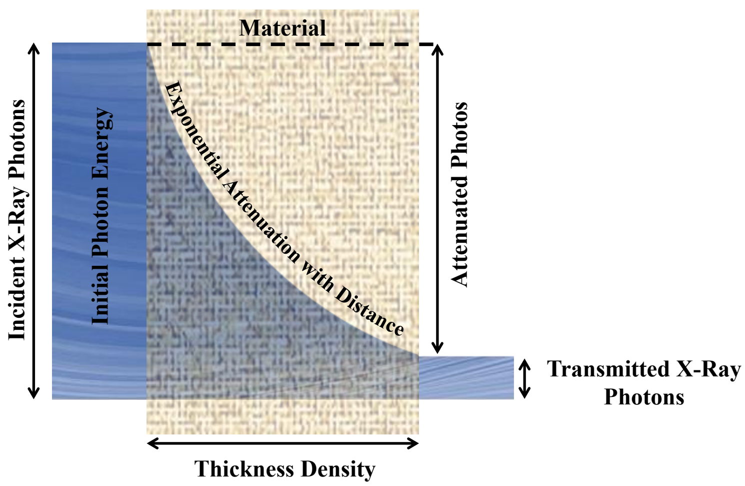

Figure 2-7 Exponential attenuation of X-ray after transmitting through a material

Bale et al. [25] statistically analyzed the shape and positioning of fiber tow of two ceramic-matrix textile composites in the 3-D woven architecture. The authors used statistics analysis of the shape and positioning of the fiber tows obtained by X-ray μCT to generate virtual, individually distinct specimens. The extracted data from the images were the coordinates of the centroid of a tow, area, aspect ratio, and the orientation of its cross-sections. This research did not consider analyzing TBC and extracting its parameters. Melenka et al. [23] used μCT to analyze porosity/void in braided composites and extract the geometrical parameters of the strand. This research provided a method for creating 3D models of TBCs that can be used to assess their quality and consistency.

Wang et al. [26] discussed the microstructure of 3D braided composites and provided a modelling approach based on the Free Form Deformation (FFD) theory. They used μCT to obtain the experimental model of a dry braided composite and MIMICS software to model the braid composite. The geometrical parameters they considered were braiding angle, interlacing angle and interval distance. In this research, SkyScan 1076 device was used to carry out the CT test. Twelve k carbon yarns were used in the experiments; however, to increase the contrast between yarns, observe the interfaces clearly and get better resolution of the cross-sectional shapes, four glass fiber bundles were used among carbon fibers. TexGen software, an open-source modelling tool, was used to create a computer-based simulation. Finally, the absolute and relative errors to verify the performance of their model against μCT results were calculated. However, this research did not study FEM on the created model.

Zhang et al. [27] studied the effect of the load-bearing direction on the progressive bending damage of a 3D five-directional braided composite. This research employed a Three-point bending test, and two types of 3D braided composites, longitudinal and transverse, were experimentally tested. Toray T700 Carbon fiber yarns were used to produce the 3D braided composite, and TDE-85 epoxy was injected to manufacture the braid. For each type of braided composite, three samples were fabricated and tested. The acoustic emission (AE) technique also monitored damage behaviour during the three-point bending test. In this research, μCT was used to detect the internal damage initiation and damage evolution and distribution characteristics of the 3D braided composite. The result recorded by AE was verified by the results obtained from μCT. The results showed that in longitudinal braided composite, the primary dominant damage was caused by fiber and yarn. While in transverse braided composite, the predominant failure was fiber slip, interface debonding, matrix cracking and fiber fracture. The study in this research was limited to 3D braided composites, and 2D braided composites were not studied.

Ya et al. [28] used μCT to analyze a three-dimensional full five-directional braided composite. There were fifteen glass fiber yarns between carbon fiber braids, thirteen of which axial and two braiding yarns. Due to the different densities of glass fiber and carbon fiber yarns, the μCT results showed enough contrast between the two types of yarns, and it was possible to separate them from each other. The glass fiber yarns were used for cross-section analysis in three different regions. The results showed that different regions of the braided composite would cause a change in cross-sections of braiding and axial yarns.

Liu et al. [29] used μCT to create representative volume cells (RVCs) of a 3D orthogonal weave composite. Using this process, the authors succeeded in capturing varied cross-section and non-symmetric undulation paths of the yarns, enhancing the accuracy of predicting the damage and failure process. A FEM was developed based on the idealized (parameterized) model and the real (μCT) model was compared against experimental results. The results show that the predicted output of the FEM based on μCT was closer to the experimental results. This study does not cover the analysis of 2D TBC.

Croom et al. [30] studied braided SiC/SiC composite strain behaviour using μCT and Volumetric Digital Image Correlation (V-DIC). The main advantage of V-DIC compared to DIC is the volumetric analysis of the braided composite. These two methods can be used to compare and validate advanced FEA models for TBC. This advantage will result in 3D analyses of the specimen, while in DIC, only the surface of the specimen is analyzed. By measuring the hoop strain, it was concluded that it changes significantly in the axial direction and reaches its maximum in yarn crossovers. The loading of the experiment was increased until the failure happened. The failure of the braided composite initiated from the cross-over points. These points were defined as maximum strain points. Only four specimens were tested in this research, while more experimental data are required to verify the results.

Yu et al. [31] developed an image processing technique based on edge detection and morphological operations to detect yarn cross-sections and yarn paths of 2-D woven composite images obtained from the μCT technique. This technique was able to calculate the distribution of pores within each cross-section. This technique cannot automatically detect and segment overlapping yarn cross-sections, which need to be segmented manually. The generated 3-D model is finally meshed using the advancing-front technique for Finite Element Modeling.

Jia et al. [32] used a combination of image processing and deep learning techniques for segmenting yarns of 2-D woven composites scanned by the μCT technique. First, they detected weft and matrix boundaries and then obtained warp edges using the curved fitting method. Symmetric images were used to train a convolutional neural network for analyzing an asymmetric image. The segmented model is then combined with an advancing-front technique to create a mesh to be inputted into FEM software.

Lomov et al. [32] developed a geometrical model for flat braided composite using the braid topology and the minimum energy principle. In this geometrical model, side crimp and yarn twisting are caused by the skewness of the braid. Also, the X-ray scans of glass braided materials were used to verify the proposed model. The voltage of the scans was 55kV, the current was 0.15 mA, and the sample size was 32×15.5×0.98 mm. The pixel size of the scanned images was 45 μm. The braid angles extracted from the μCT scan and the camera photos were compared together for verification. In this research, the quantitative data of μCT images were not extracted.

Table 2-1 summarizes the research done on the μCT scan of braided composite. As one can see, the current literature focuses on 3D braided composite, and limited research has been done on the 2D braided composite. Therefore, a comprehensive study on using μCT images to extract the parameters of 2D TBCs (such as area, inner diameter, braid angle, yarn path, the orientation of the yarn cross-section, the minor and major diameter of the yarn cross-section, and the center points of the yarn cross-sections) is needed.

Table 2-1 Literature focusing on μCT scan of braided composite.

Paper	**Type of composite material**	**Type of matrix**	**Type of fiber**	**Braid geometry (2D or 3D)**	**Out-put**	**Used software**
Bale et al. [25]	Flat braided composite	SiC	Silicon Carbide (SiC)	3-D	Yarn segmentation	Avizo v6.1
Melenka et al. [23]	Tubular Braided Composite (Diamond)	Epoxy resin	Kevlar 49	2-D	Porosity/void Geometry of fiber	SimpleWare
Wang et al. [26]	Tubular Braided Composite	N/A	Carbon fiber	3-D	Presenting a modeling approach	MIMICS
Zhang et al. [27]	Rectangular braids	Epoxy resin	Carbon fiber	3-D	Damage analysis	NRecon
Ya et al. [28]	Five directional Braided composite	Resin	Carbon fiber/ Glass fiber	3-D	Predicting mechanical properties	MIMICS
Liu et al. [29]	Five directional braided composites	epoxy TDE-85	Carbon fiber (Glass fiber as a tracer)	3-D	Geometrical variabls	MIMICS
Lomov et al [32]	Flat braided composite		Glass	2D	Geometrical variables	N/A

2.5 Finite Element Modelling (FEM) of Braids

One method for generating the simulation of TBCs is using Digital Image Correlation (DIC) [20]. DIC is a non-contact optical technique used to measure full-field displacements and strains on the surface of an object undergoing deformation. It is widely used in various fields, including material science, engineering, biomechanics, and geotechnical studies. The DIC method analyzes digital images captured during an experiment or test at different times. The basic principle is to track the movement of small subsets or regions of interest (ROIs) within the images and measure their displacements and deformations over time. While the usage of DIC has several advantages, including the ability to determine displacement and deformation in any direction and at any point [21], the main disadvantage of this method for creating 3D models for TBCs is its limitation to only scan the surface of the test piece, not the inside [22]. FEM does not have this limitation, and it can analyze the materials thoroughly.

Using finite element modelling, Xu et al. [37] analyzed flat braided composites. They modelled carbon fiber braided composite with different braid angles (19°, 30°, and 37°) and studied the effect of braid angle on the mechanical properties of the braided composite. They considered unit cells in each case and applied periodic boundary conditions (PBC) to their model. Additionally, these researchers compared the mechanical properties of biaxial and triaxial braided composite with different patterns (Diamond, Regular, Hercules) against laminate composite properties resulting from Classical Laminate Theory (CLP). This paper concluded that all the modelled samples show the same behaviour. The numerical results were compared against experimental results to verify the model. However, this study was for flat braided composite, which does not include tubular braided composite, especially with a small diameter.

Li et al. [36] developed a 3-dimensional five-directional rectangular braided composite finite element model. In this research, Carbon fiber (T300), Epoxy resin, and phenolic resin materials were used as fiber and matrix. Their model considered cross-section deformation and surface contact in the braiding process. Also, the effect of braiding parameters on the mechanical properties was investigated. In this research, the cross-section of braiding yarns was assumed to be a hexagon, and for axial yarns, it is considered to be an octagon. Also, the braided structure was supposed to be uniform, and the yarns were also in the jam angle. A unit cell was selected and analyzed in this research, and periodicity conditions were imposed on its boundaries. FEM analysis was done by ANSYS parametric design language (APDL). The yarn path is also assumed to be straight, and no undulation is applied to it. Finally, the simulated analysis results under tensile loading in the X and Z directions and shear loading under the X-Y plane are compared with the experiment and theoretical solutions to verify the simulation. The analysis shows that the composite's axial yarns are the main bear-loading component, and stress concentrates at the crossing point of yarns, which is the weakest part of the reinforcement.

Zhang et al. [37] used the FEM method to simulate braided composite tubes to study the energy absorption of braided composites to improve the crashworthiness of components. In this research, ABAQUS/Explicit was used to model the braided composite tube and analysis was applied in a unit cell. The 2D triaxial braided composite was made of fiberglass, and epoxy resin was used as the material in designing the FEM. The cross-section of each yarn is assumed to be rectangular and remains constant along the entire yarn path. The axial yarns were also assumed to be completely straight, and braiding yarns were considered to follow a straight path. Finally, simulated results were validated by comparing them with experimental test results.

Zhou et al. [38] presented a finite element analysis on transverse impact responses of tubular braided composite. They applied their model into three braid angles: 15°, 30° and 45°, and the outputs of the model were the impact damage, deformation and stress distribution. Finally, they concluded that stress propagation in lower braiding angles was faster than in higher braiding angles. The FEA model's results were compared against experimental load-displacement curves and energy absorption results for verification. The novelty of this work was studying the impact behaviour of the 3-D tubular braided composite under transverse direction and finding the impact of braiding variables on that. In this research, the matrix was considered to be isotropic, and yarn tows were transversely isotropic.

Ji et al. [39] computed the effective elastic properties of braided composites. In this paper, an experiment was conducted on a beam structure with a foam core covered by two layers of biaxial reinforced braided composite. Also, the authors used the FEM technique to study the behaviour of braided composite in different braided angles (from 20 degrees to 55 degrees with a 5-degree step size increment). They recorded Young's moduli, shear moduli and Poisson's ratios at each braid angle. Additionally, they studied the relationship between elastic constant and fiber volume fraction for a braided composite with a 60-degree braid angle. In their study, the matrix material is assumed to be isotropic, and braiding yarns are assumed to be transversely isotropic. They analyzed a single unit cell in their research and observed that stress concentration mainly occurs at the edges of the yarn. They concluded that the longitudinal Young's modulus, E_{22}, decreases with the increase of braiding angle, and the transverse Young's modulus, E_{11}, increases with the braiding angle. However, Young's modulus in the through-thickness direction, E_{33}, only increases slightly. Also, the in-plane shear modulus, G_{12}, increases with the braiding and reaches its maximum at a 45-degree braid angle. However, the through-thickness shear moduli, G_{23}, and G_{13}, increase insignificantly with the increase of the braiding angle. All of Poisson's ratios vary in a nonlinear manner with the rise of the braiding angle. Finally, they have an experimental bending test to verify the result of their simulation model. It should be noted that their model did not consider the contact behaviour of yarns.

Shigang et al. [40] did a statistical analysis of the volume fraction and positioning of the void defect in the 3D orthogonal woven architecture based on 2D microtomography images. The void volume fraction of the 3D geometrical model in this research was reported to be 0.44%. Based on the data obtained, a virtual specimen sharing similar statistical characteristics of the C/C (carbon fiber reinforced carbon) composite and the void defects are generated. A FEM simulation is developed based on the generated model, and the result of the simulation is compared against a three-point bending experiment to verify the result.

Zhang et al. [41] proposed a technique to analyze TBC by combining MATLAB and Abaqus software packages. They used the representative volume element (RVE) model comprised of dry fibers and matrix for their analysis. In this research, the cross-sections of yarns are assumed to be elliptical. The geometrical model was designed in MATLAB software and then imported to the Abaqus solver for analysis. The reason for combining these two software packages was to propose a labour-saving technique that is less time-consuming since it overcomes the difficulty in generating a periodic mesh for the RVE model.

Different braids with various braiding angles were designed and imported to the FEM solver, and the predicted tensile modulus was compared against experimental and previous model results proposed by the same research group [42]. The results showed that the traditional methods worked better in terms of accuracy, but the proposed method is less time-consuming.

Gou et al. [43] proposed a method to consider the symmetric conditions of a unit cell of a braided composite and analyzed the reduced unit cell by half, quarter and eighth size. Relative boundary conditions for thermal analysis were derived and applied based on each rotation transformation. Braided composites with different fiber volume fractions and braiding angles were analyzed, and the corresponding thermal conductivities were calculated. The same braided composites were investigated with adiabatic (a temperature difference is imposed on boundary planes in the calculation direction) boundary conditions, and the results are compared against the proposed boundary conditions to evaluate the difference between the two methods. Also, the numerical results are compared to experimental results to validate the proposed method.

Wang et al. [44] provided a FEM analysis based on a geometrical model. They created a rectangular braided composite by GenTex software, an open-source software package that used a mapping method to convert the rectangular model into a tubular form. They used voxel mesh for the model imported to the FEM software package and presented the result in the form of displacement and stress. Also, they changed some geometrical parameters (pitch length, mandrel diameter, number of carriers and circumferential numbers) of the model. They studied the effect of these parameters on the longitudinal elastic moduli.

Dong et al. [45] provided a model for measuring the thermal conductivity of 3-D braided composite by using FEM. They analyzed the representative volume element (RVE) and the full-scale structure level of a 3-D braided composite. The results of RVE were more accurate and closer to the experimental results. However, it was more time-consuming. On the other hand, the full-scale method shows more accurate results, but it was more time-consuming compared to RVE. The main reason for the difference between these two methods is that different unit cells in different positions would have various thermal conductivity. In the RVE method, this difference is ignored; in the full scale, all braided composite sections are considered.

Chen and Aliabadi [46] proposed a mesh-free-based method for micromechanical modelling and homogenizing elastic properties of twill woven composite to predict their displacement and stress/strain behaviour. In their model, the minimum unit cell (mUC), which is 1/16 of a full unit cell, is used, and the boundary conditions are applied by using an equivalence approach. In the meshfree method, nodes were used to discretize the problem, but in contrast to the FEM method, the nodes were not connected to form elements. Then, the researchers compared the result of their proposed method with FEM results which were in good accordance with each other. Finally, the sensitivity of the model was analyzed by performing a numerical investigation for three types of parameters: the number of field nodes, the number of background cells, and the support domain scaling factor.

Zhang et al. [47] developed a mesoscale voxel-based FEM for analyzing the effect of the voxel size on the 3D angle-interlock woven composites subjected to axial tensile loading. They used five different mesh sizes in their analysis and concluded that the effect of mesh size on evaluating mechanical elastic properties is insignificant. However, it is essential to study the damage behaviour. In this research ABAQUS software package is used for FEM analysis.

Ghaedsharaf et al. [48] proposed a modelling method for predicting the geometrical shape of the biaxial braids. Sixty-one fibers were used as an optimal number of fibers in each yarn. A FEM was developed on ABAQUS software using the geometrical model, and a 1 N tensile load was applied to the model. The truss elements are used for modelling fibers of TBC, and the actual properties of fibers are used in the analysis. Then, two cross-sections of the models were selected and compared against the two cross-sections obtained from the μCT model. The outer diameters of these two models were compared together, with 2.06% and 1.58% errors between the two measurements. The inner void of the models was compared visually, and the 3D models were used to compare the waviness of the models visually. Both models show 19 degrees for the braid angle. These researchers studied the diamond and regular patterns. In this research, the yarn path of the models was not analyzed, and the cross-section of the yarns was detected manually. Also, only two cross-section images were analyzed, and other parameters of the braids, such as inner diameter, minimum and maximum diameters of all yarns, and center points of the yarns, were not reported.

Wang et al. [49] used a Finite Element Simulation method to generate an annular braided composite yarn path. For each yarn, nine virtual fibers were assumed and modelled. An annular braided composite was manufactured using a vertical braiding machine to validate the model. Twenty images were taken by camera from the actual annular braid, and the braid angle and the yarn spacing were measured from each image. Similarly, the simulation's braid angle and yarn spacing were measured and compared with the result of the actual braid for validation.

The summary of the reviewed papers is tabulated in Table 2-2.

Table 2-2 Summary of the literature in Finite Element Modeling

Paper	**Type of Composite**	**Material**	**Software**	**Mesh**	**Output**
Xu et al. [50]	flat braided composite	Carbon fiber	N/A	tetrahedron	Elastic Properties
Li et al. [36]	3D five directional	Carbon fiber	ANSYS	parabolic tetrahedral	Elastic Properties
Zhang et al. [37]	2D triaxial	fiber glass	ABAQUS	N/A	Displacement, Energy absorption
Zhou et al. [38]	3-D TBC	Carbon fiber	N/A	Eight-node brick element	impact damage, deformation and stress distribution
Ji et al. [39]	braided textile composites	Carbon fiber	ABAQUS	3D hexagon 8-node	Elastic properties
Shigang et al. [40]	3D orthogonal woven composite	Carbon fiber	ABAQUS	hexahedral element with eight nodes	Mises stress, Deflection
Zhang et al. [41]	3D four-directional	Carbon fiber	MATLAB and Abaqus	periodic mesh	Tensile modulus

Wang et al [42]	3D four-directional	Carbon fiber	ABAQUS	four-node tetrahedron	Elastic properties
Gou et al. [43]	3D four-directional	Carbon fiber	ANSYS	SOLID 70 (eight node)	Thermal Conductivity
Wang et al. [44]	3D TBC	Carbon fiber	N/A	N/A	Elastic properties
Dong et al. [45]	3D braided composite	Carbon fiber	ABAQUS/Standard (ver. 6.12)	tetrahedral	Thermal Conductivity
Chen and Aliabadi [46]	twill woven composite	Carbon fiber	ABAQUS	meshfree-based models	Elastic properties
Zhang et al. [47]	3D Angle-Interlock Woven Composites	Carbon fiber	ABAQUS/Standard	voxel-based model	Effect of mesh size on elastic behaviors, global stress-strain curves, local stress distribution and progressive damage process
Ghaedsharaf et al. [48]	biaxial braids	Carbon fiber	ABAQUS	Truss Element	
Wang et al. [49]	annular axis braided	Carbon fiber	Abaqus/CAE	N/A	Obtain the yarn path

One of the controversial topics in Finite Element Analysis studies is verification and validation. Verification and Validation (V&V) is a method for creating computer models that may be used to generate engineering predictions with a high level of certainty. Validation in FEM is the process of determining if simulation findings are representative of real-world outcomes. In other words, validation is determining the degree to which a model accurately represents the real world from the standpoint of the model's intended purposes. Verification is the process of ensuring that the finite element analysis (FEA) was carried out correctly. Verification, in other words, ensures that a model implementation accurately reflects the developer's conceptual definition of the model and its solution. Validation and verification are two methods to ensure that a product is safe to use [51].

2.6 Analytical Models

Analytical models provide another tool for analyzing braided composites. The results of this research can be used to validate the accuracy of the FEM simulations for braided composites. Additionally, the results of both models will be compared against an experimental result to compare the accuracy of each model. A number of research studies have been done in this field, and some of them are reviewed below.

Melenka and Carey [7] proposed a numerical model to predict the mechanical properties of braided composites with different patterns. They used the volume-averaging stiffness model for considering yarn undulations and the orientation of braid yarns within the braid structure. They also validated their model with experimental results and compared them with FEA and other analytical models. Additionally, they provided software (Braid CAM) [52] to facilitate the implementation of braided composites for engineering design and applications.

Quek et al. [53] developed an analytical model to calculate the effective linear elastic stiffness of 2D triaxial flat braided composites and considered initial unintended microstructural imperfections in the calculated stiffness. Volume averaging calculates the contribution from each tow on representative unit cell. For validation, the result of the model is compared against experimental and FEA results.

Fang and Liang [54] studied the literature on researching modelling three-dimensional braided textile composites and discussed numerical modelling used to analyze 3D braided composites. Different meso-geometrical models were reviewed, and their power to accurately present numerical results is also provided. Furthermore, different mesh generation techniques were used to discretize the complex geometries. Various FEM used to predict damage development and failure of 3D composite materials are also reviewed in this research.

Melenka and Carey [33] provided a methodology to analyze the strain field and assess the mechanical properties of the unit cell of diamond and regular tubular braided composite. They used the contactless 3-D DIC technique to capture the tension and experimental tensile test results. They studied the effect of braid angle and braid pattern on the final mechanical properties.

2.7 FEM Based on µCT Models

Because of the high resolutions and accuracy of the models created by micro–Computed Tomography (µCT), they provide excellent geometrical models to be used to develop a FEM. The accurate input model for creating a FEM simulation will help to have better results with higher accuracy and precision. µCT based FEM is used in different fields, and some of the research papers are reviewed below.

Ge et al. [55] presented a trans-scale method coupled with Micro-CT to investigate the strength and damage behaviour of 3D braided composites with pore defects. The authors developed a progressive damage model to describe the damage initiation and evolution of constitutes of 3D braided composites across different scales. The meso-scale simulation results agreed with the experimental data, and different damage modes, such as yarn damage, matrix cracking, and interface debonding, were recognized with the increasing tensile load. The damage also appeared around the pore defects and then developed to the weak region in the matrix.

Li et al. [56] investigated the impact shear fracture mechanisms in 3D braided composites through computed tomography (CT) and finite element analyses (FEA). The study analyzed the influence of braiding parameters on damage modes such as fiber tows fracture, debonding, resin cracks, and inter-yarn delaminations under impact shear loading. The research reported that braiding structural parameters predominantly determine the failure mode, ultimately impacting energy absorption capacity. A meso-structure geometrical model based on the braided preform structure is developed to calculate stress distribution and simulate shear damage modes. Comparative analysis between FEA and micro-CT observations demonstrates consistency in capturing impact shear damage morphologies and revealing energy absorption mechanisms.

Li et al. [57] explored the damage mechanisms of three-dimensional (3D) rotary-five-directional (3DR5d) braided composites. The study establishes a parametric finite element model, incorporating realistic yarn cross-sections based on Micro-CT scans. A systematic approach for damage prediction is developed, enabling analysis of damage behaviours, tensile mechanical properties, and damage evolution of 3DR5d braided composites. The impact of braiding angles and fiber volume fractions on mechanical properties and damage mechanisms is investigated via parametric analysis. Findings reveal that decreasing braiding angle and increasing fiber volume fractions enhance the strength and modulus of 3DR5d braided composites. Additionally, transverse shear emerges as a dominant factor in the tension-induced failure of these composites.

The papers mentioned above discussed the application of µCT based FEM on braided composite materials, and in all of them, the 3D braided composites are studied. There is no study in the literature focusing on the 2D TBCs.

µCT based FEM has other applications too. One of the most popular applications of µCT based FEM is in the medical industry. Because of the irregular shape of medical specimens and the high precision required for the inputted geometrical models, µCT is used for this purpose frequently. Figure 2-8 shows the workflow of creating a FEM based on the µCT model.

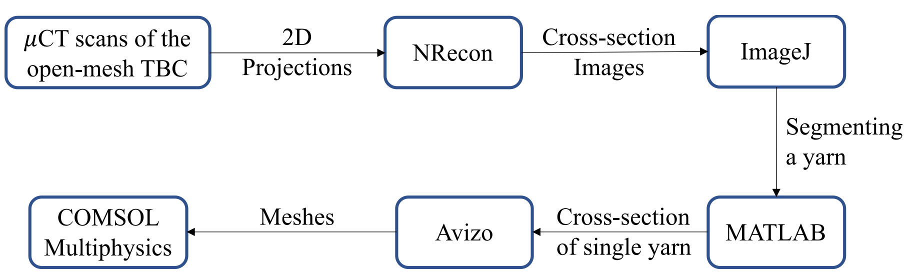

Figure 2-8 Workflow of creating a µCT FEM

2.7.1 Medical Applications of µCT Based on FEM

Hambli [58] developed a FEM for simulating the fracture of human trabecular bone under compressive load. The model is based on continuum damage mechanics and can predict the ultimate stress and strain at fracture. The study used an isotropic micro-CT FEM at the bone tissue level and coupled it with a damage law to simulate the progressive fracturing process of bone tissue. In this paper, Skyscan 1072 was used to analyze the samples, and the spatial resolution of the scanned images was 20 µm. The FE model was created and meshed using an in-house developed MATLAB program. The model was validated with experimental results performed on 23 human trabecular specimens. The compression experiments were done on samples, and Instron, model 4411, was used for this purpose. This work aimed to predict the fracture behaviour of human trabecular bone, which can have implications for understanding bone diseases and injuries, designing medical implants, and developing treatments for bone fractures.

Shefelbine et al. [59] described a non-invasive and quantitative method to evaluate fracture callus stiffness during healing using µCT and FEA. The method was developed and validated using plastic phantoms of various cross-sections and known material properties and was then applied to fractured rat femurs after 3 and 4 weeks of healing. The ANSYS software was used for developing the FEM simulation. The µCT scan was done at 40 kV source voltage, 180 µA source current, and 100 µm resolution. The µCT scans provided 3D geometry and material properties for the FEA models. The predicted callus rigidity from FEA correlated significantly better with experimental torsional rigidity than other measures of healing progress. The study suggests that FEA could be a valuable tool for assessing the mechanical properties of the callus in fracture healing studies.

Verdonschot et al. [60] proposed a method for generating 3D finite element models of restored human teeth. The method involves using micro-CT imaging to capture high-resolution images of the tooth and the restorative material and then using image processing techniques to generate a FEM. The Scanco MircorCT 20 device was used for the µCT scan of the tooth. The scan grid was 1024 × 1024 with 13 µm resolution. The scan slice thickness was 25 µm, and 770 images were captured from the molar with 10 msec exposure time. The authors used in-house software for generating the 3D models out of µCT scans. The Mental preprocessor was used to convert the model into volume elements and perform the FE analysis. The authors demonstrated their method's effectiveness by analyzing stress distribution in different types of restored teeth and predicting their failure modes.

Jaecques et al. [61] discussed the importance of understanding the mechanical properties of native bone tissue and engineered tissue constructs for successful bone replacement treatments. It suggests that µCT-based FEM can be a valuable tool for analyzing the stress and strain state in native bone tissue and tissue constructs. The paper provides two case studies to illustrate the utility of this approach: peri-implant bone adaptation analysis through µCT scanning and biomechanical optimization of bone scaffolds. The paper showed the potential for optimizing the mechanical properties of bone scaffolds to match those of native trabecular bone.

The above research showed that the µCT has various medical applications in developing FEM simulation. This technique has been used with high resolutions to create an accurate simulation model. One can conclude that µCT is good at developing models for flexible and irregular shapes parts like Tubular Braided Composites.

2.7.2 Material Applications of µCT Based on FEM

Lee et al. [62] described the microstructural and mechanical properties of nickel foam struts fabricated by electroplating on a chemically removable template. The 3D microstructures of the Ni foams were obtained using µCT, and the microstructural features were quantified statistically.

Microstructure evolution and mechanical properties during Ni-foam compression were investigated using µCT and the FEM. The µCT scans were done by a Nikon XT H 160 Micro-CT device. The beam energy was 155 kV, the beam current 157 µA, and 1440 projections were captured. The AVIZO software was used to render the stacked images into a 3D model. 4-node tetrahedron elements were used to reconstruct the 3D models used for FE analysis. The study found that compression caused transverse buckling of the struts, reducing the stress and increasing the calculated energy absorption efficiency. The paper provides insights into the deformation behaviour and energy absorption characteristics of open-cell Ni-foams, which could be helpful in their practical applications.

D'Andrea et al. [63] used µCT-based FEM to investigate the mechanical properties of two classes of robocast glass scaffolds, focusing on accounting for geometrical defects introduced during manufacturing. The scaffolds had a fiber distribution along two perpendicular directions on parallel layers with a 90-degree tilting between two adjacent layers. The resolution of the scanned µCT was 5 µm. Fiji software was used to create the 3D model of the scanned images and quantify porosities and voids. Also, the FE Analysis was done using the open-source multigrid finite element code ParOSol. The FEM had element sizes of 10 µm, and 77 to 105 million elements were used for the elastic analyses and 34 to 40 million for the strength analysis. The domain size used for elastic analysis was 1200 × 1200 × 800 pixels. The study found that imperfections in the scaffolds, such as micro-porosity, fiber length interruption, and fiber detaching, substantially impacted elastic and strength properties. In addition, micro-pores acted as stress concentrators promoting fracture initiation and propagation, while fiber detachment reduced the scaffold properties substantially along the direction perpendicular to the fiber plane.

Basista et al. [64] presented a methodology for using µCT in the numerical modelling of metal-ceramic composites. The paper provided detailed instructions on FEM creation. First, the proposed method was demonstrated through two case studies, which showed its application in determining processing-induced residual stresses in hot-pressed Cr/Al2O3 and NiAl/Al2O3 particulate composites. Then, it determined the J-integral for an interpenetrating phase composite made of porous alumina preform infiltrated with molten copper.

Shigang et al. [65] overviewed image-based modelling techniques for heterogeneous materials. The authors reviewed a variety of image-based modelling techniques such as FEM, lattice models, phase field method, level set methods, and artificial intelligence-based methods. They discuss the advantages and limitations of each method and provide examples of their applications in different fields, such as material science, mechanics, and biomedical engineering. The authors highlighted the importance of image-processing techniques for generating accurate 3D models of heterogeneous materials. They emphasized the need for further development of image-based modelling techniques to understand the behaviour of complex materials better.

Khormani et al. [66] presented an approach for determining the compressive strength of concrete specimens. The authors obtained high-resolution 3D images of the internal structure of concrete specimens using X-ray computed tomography and applied FEM simulations to predict the compressive strength. The study results showed that the proposed approach was able to accurately predict the compressive strength with an average error of 6.35% and a coefficient of determination of 0.96. The study demonstrates the potential of non-destructive testing techniques in accurately assessing the properties of concrete, which has important implications for the construction industry.

In summary, the applications of μCT based FEM is expanding to other fields and different software and image processing techniques are represented to showcase the new applications.

2.8 Research Gap

According to the reviewed literature, some gaps exist in the literature on modelling 2D TBCs. First, there is no easy-to-use and user-friendly application for creating geometrical models. The current equations for modelling TBCs are complex, and the users require a strong background in understanding the details of TBCs. However, an easy-to-use application can resolve this issue. This gap will be addressed in Chapter 3.

Additionally, very little literature covers simulations of 2D TBCs. Most of the literature is focused on the simulation of 3D braided composite. 2D TBCs have some specific advantages, like being more accessible for manufacturers and less expensive, which are important to study and simulate to improve their applications. In this research, a comprehensive Finite Element Modeling (FEM) will be developed to study the behaviour of TBCs and the effect of different geometrical parameters and patterns on the mechanical properties of TBCs. This gap is addressed in Chapter 6.

Finally, μCT methods have been used to analyze different types of materials and have shown significant results. However, few works analyze 2D TBCs using μCT. μCT is one of the most accurate methods for modelling materials, and it can reveal many valuable details of the scanned objects. Using μCT on 2D TBCs can add a significant contribution to the field. Also, there is no comprehensive image processing study on μCT scanned images of 2D TBC, and the data extraction of these materials still needs more attention. In this study, different TBCs with different patterns, sizes and materials are scanned by μCT, and an image processing technique has been developed to extract the information of the TBCs, including but not limited to the yarn center, minor and major diameter of the yarn, inner and outer diameter of the TBC. These gaps are addressed in Chapters 4 and 5.

2.9 Conclusion

This research will study the modelling of 2D TBC, and solutions for improving its procedures will be provided. Based on the literature review, a user-friendly application is necessary. This application will help industry and academia better understand the shape of TBCs and use them for education and industrial purposes. Also, the created models will be imported into COMSOL Multiphysics to create FEM simulations under different conditions. The results of the FEM will be compared against available analytical and experimental results. The effect of pattern and braid angle will be studied, too. The developed FEM in this research for a Kevlar 49 TBC is compared against experimental results in the literature, and the error between these two models was 18%. This model was developed using a Curve model. The error between the experimental and the Curved model was 46% which was greater than the FEM results developed in this study.

Then, the image processing techniques will be used to extract the parameters of the µCT scanned images. These techniques will help to segment the yarns and extract geometrical parameters like the inner and outer diameter of the composite material. Also, the area cross-section of the yarns, center point, orientation, and minor and major diameter are extracted. The extracted yarn path is compared against the mathematical one to report the error. In this research, a new parameter as rotation angle, is introduced for the first time, and by using it, the fitness of the simulation yarn path is improved significantly. An inverse problem will be designed for that purpose, and a curve with an error of less than 1% will be fitted to the experimental results.

This study offers a valuable resource to fellow researchers and industry professionals by providing a simulation tool for TBC manufacturing and an easy-to-use and open-source program (TBC-Gen) for modelling geometrical models of TBC. This simulation tool has the potential to significantly cut costs and save time while enhancing the overall product quality. Also, the TBC-Gen is the first free and open-source program for researchers to generate their desired TBC models quickly and efficiently. Besides researchers, this program can be used for educating students and personnel to showcase the effect of parameters on the overall shape of the TBC and visualize them before manufacturing.

Additionally, the presented error analysis sheds light on the inherent error level in the geometric model. This information can guide decision-making, enabling users to determine whether to rely on the geometric model or opt for more costly and time-intensive methods such as micro-CT for analysis.

2.10 References

[1] A. K. Kaw, *Mechanics of composite materials*. CRC press, 2005.

[2] "Performance Composites Inc." [Online]. Available: https://www.performancecomposites.com/about-composites-technical-info/122-designing-with-fiberglass.html#:~:text=The typical composite materials can,biaxial cloth or triaxial cloth.

[3] R. R. Nagavally, "Composite materials-history, types, fabrication techniques, advantages, and applications," *Int. J. Mech. Prod. Eng*, vol. 5, no. 9, pp. 82–87, 2017.

[4] T.-D. Ngo, *Composite and Nanocomposite Materials: From Knowledge to Industrial Applications*. BoD–Books on Demand, 2020.

[5] X. Gao, L. Yuan, Y. Fu, X. Yao, and H. Yang, "Prediction of mechanical properties on 3D braided composites with void defects," *Compos B Eng*, vol. 197, p. 108164, Sep. 2020, doi: 10.1016/J.COMPOSITESB.2020.108164.

[6] C. Ayranci and J. Carey, "2D braided composites: A review for stiffness critical applications," *Compos Struct*, vol. 85, no. 1, pp. 43–58, Sep. 2008, doi: 10.1016/J.COMPSTRUCT.2007.10.004.

[7] G. W. Melenka and J. P. Carey, "Development of a generalized analytical model for tubular braided-architecture composites," *J Compos Mater*, vol. 51, no. 28, pp. 3861–3875, Dec. 2017, doi: 10.1177/0021998317695421.

[8] J. Carey, A. Fahim, and M. Munro, “Design of braided composite cardiovascular catheters based on required axial, flexural, and torsional rigidities,” *J Biomed Mater Res*, vol. 70B, no. 1, pp. 73–81, Jul. 2004, doi: 10.1002/jbm.b.30017.

[9] L. Xu, S. J. Kim, C.-H. Ong, and S. K. Ha, “Prediction of material properties of biaxial and triaxial braided textile composites,” *J Compos Mater*, vol. 46, no. 18, pp. 2255–2270, Aug. 2012, doi: 10.1177/0021998311431353.

[10] J. P. Carey, *Handbook of advances in braided composite materials: Theory, production, testing and applications*. Woodhead Publishing, 2016.

[11] G. W. Melenka, C. M. Pastore, F. K. Ko, and J. P. Carey, “Advances in 2-D and 3-D braided composite material modeling,” in *Handbook of Advances in Braided Composite Materials: Theory, Production, Testing and Applications*, 2016, pp. 321–363. doi: 10.1016/B978-0-08-100369-5.00009-X.

[12] S. R. Swanson and L. V. Smith, “Comparison of the biaxial strength properties of braided and laminated carbon fiber composites,” *Compos B Eng*, vol. 27, no. 1, pp. 71–77, Jan. 1996, doi: 10.1016/1359-8368(95)00008-9.

[13] M. Gautam, V. Potluri, and S. Ogin, “NECKING BEHAVIOUR OF FLATTENED TUBULAR BRAIDED COMPOSITES,” 2015.

[14] P. J. Falzon and I. Herszberg, “Mechanical performance of 2-D braided carbon/epoxy composites,” *Compos Sci Technol*, vol. 58, no. 2, pp. 253–265, Jan. 1998, doi: 10.1016/S0266-3538(97)00133-4.

[15] G. W. Melenka and J. P. Carey, “Development of a generalized analytical model for tubular braided-architecture composites,” *J Compos Mater*, vol. 51, no. 28, pp. 3861–3875, Dec. 2017, doi: 10.1177/0021998317695421/ASSET/IMAGES/LARGE/10.1177_0021998317695421-FIG17.JPEG.

[16] T. Liao and S. Adanur, “A Novel Approach to Three-Dimensional Modeling of Interlaced Fabric Structures,” *http://dx.doi.org/10.1177/004051759806801109*, vol. 68, no. 11, pp. 841–847, Nov. 1998, doi: 10.1177/004051759806801109.

[17] J. S. Tate, A. D. Kelkar, and J. D. Whitcomb, “Effect of braid angle on fatigue performance of biaxial braided composites,” *Int J Fatigue*, vol. 28, no. 10, pp. 1239–1247, Oct. 2006, doi: 10.1016/J.IJFATIGUE.2006.02.009.

[18] T. Alpyildiz, “3D geometrical modelling of tubular braids,” *Textile Research Journal*, vol. 82, no. 5, pp. 443–453, Nov. 2011, doi: 10.1177/0040517511427969.

[19] A. Rawal, S. Gupta, H. Saraswat, and A. Sibal, “Geometrical modeling of near-net shape braided preforms,” *Textile Research Journal*, vol. 85, no. 10, pp. 1055–1064, Jun. 2015, doi: 10.1177/0040517514559587.

[20] Y. Kyosev, “Generalized geometric modeling of tubular and flat braided structures with arbitrary floating length and multiple filaments,” *Textile Research Journal*, vol. 86, no. 12, pp. 1270–1279, Jul. 2016, doi: 10.1177/0040517515609261.

[21] J.-H. Byun, “The analytical characterization of 2-D braided textile composites,” *Compos Sci Technol*, vol. 60, no. 5, pp. 705–716, Apr. 2000, doi: 10.1016/S0266-3538(99)00173-6.

[22] G. W. Melenka, E. Lepp, B. K. O. Cheung, and J. P. Carey, "Micro-computed tomography analysis of tubular braided composites," *Compos Struct*, vol. 131, pp. 384–396, Nov. 2015, doi: 10.1016/j.compstruct.2015.05.057.

[23] S. Y. Chung, J. S. Kim, D. Stephan, and T. S. Han, "Overview of the use of micro-computed tomography (micro-CT) to investigate the relation between the material characteristics and properties of cement-based materials," *Constr Build Mater*, vol. 229, p. 116843, Dec. 2019, doi: 10.1016/J.CONBUILDMAT.2019.116843.

[24] H. Bale, M. Blacklock, M. R. Begley, D. B. Marshall, B. N. Cox, and R. O. Ritchie, "Characterizing Three-Dimensional Textile Ceramic Composites Using Synchrotron X-Ray Micro-Computed-Tomography," *Journal of the American Ceramic Society*, vol. 95, no. 1, pp. 392–402, Jan. 2012, doi: 10.1111/j.1551-2916.2011.04802.x.

[25] Y. Wang, Z. Liu, N. Liu, L. Hu, Y. Wei, and J. Ou, "A new geometric modelling approach for 3D braided tubular composites base on Free Form Deformation," *Compos Struct*, vol. 136, pp. 75–85, Feb. 2016, doi: 10.1016/J.COMPSTRUCT.2015.09.036.

[26] P. fei Zhang, W. Zhou, H. fei Yin, and Y. jing Shang, "Progressive damage analysis of three-dimensional braided composites under flexural load by micro-CT and acoustic emission," *Compos Struct*, vol. 226, Oct. 2019, doi: 10.1016/j.compstruct.2019.111196.

[27] J. Ya, Z. Liu, and Y. Wang, "Micro-CT Characterization on the Meso-Structure of Three-Dimensional Full Five-Directional Braided Composite," *Applied Composite Materials*, vol. 24, no. 3, pp. 593–610, Jun. 2017, doi: 10.1007/s10443-016-9528-x.

[28] Y. Liu, I. Straumit, D. Vasiukov, S. V. Lomov, and S. Panier, "Prediction of linear and non-linear behavior of 3D woven composite using mesoscopic voxel models reconstructed from

X-ray micro-tomography,” *Compos Struct*, vol. 179, pp. 568–579, Nov. 2017, doi: 10.1016/j.compstruct.2017.07.066.

[29] B. P. Croom, P. Xu, E. J. Lahoda, C. P. Deck, and X. Li, “Quantifying the three-dimensional damage and stress redistribution mechanisms of braided SiC/SiC composites by in situ volumetric digital image correlation,” *Scr Mater*, vol. 130, pp. 238–241, Mar. 2017, doi: 10.1016/j.scriptamat.2016.12.021.

[30] G. Yu, Y. Jia, C. Dong, X. Gao, F. Wang, and Y. Song, “Geometric parameters characterization of minicomposite and modulus prediction of 2D composite based on X-ray computed tomography,” *Ceram Int*, Jul. 2021, doi: 10.1016/J.CERAMINT.2021.07.219.

[31] Y. Jia, G. Yu, J. Du, X. Gao, Y. Song, and F. Wang, “Adopting traditional image algorithms and deep learning to build the finite model of a 2.5D composite based on X-Ray computed tomography,” *Compos Struct*, vol. 275, p. 114440, Nov. 2021, doi: 10.1016/J.COMPSTRUCT.2021.114440.

[32] S. V. Lomov, R. S. Parnas, S. Bandyopadhyay Ghosh, I. Verpoest, and A. Nakai, “Experimental and Theoretical Characterization of the Geometry of Two-Dimensional Braided Fabrics,” *http://dx.doi.org/10.1177/004051750207200810*, vol. 72, no. 8, pp. 706–712, Aug. 2002, doi: 10.1177/004051750207200810.

[33] G. W. Melenka and J. P. Carey, “Experimental analysis of diamond and regular tubular braided composites using three-dimensional digital image correlation,” *J Compos Mater*, vol. 51, no. 28, pp. 3887–3907, Dec. 2017, doi: 10.1177/0021998317695418.

[34] J. Górszczyk, K. Malicki, and T. Zych, “Application of Digital Image Correlation (DIC) Method for Road Material Testing,” *Materials*, vol. 12, no. 15, Aug. 2019, doi: 10.3390/MA12152349.

[35] N. McCormick and J. Lord, “Digital Image Correlation,” *Materials Today*, vol. 13, no. 12, pp. 52–54, Dec. 2010, doi: 10.1016/S1369-7021(10)70235-2.

[36] D. Li, D. Fang, N. Jiang, and Y. Xuefeng, “Finite element modeling of mechanical properties of 3D five-directional rectangular braided composites,” *Compos B Eng*, vol. 42, no. 6, pp. 1373–1385, Sep. 2011, doi: 10.1016/J.COMPOSITESB.2011.05.042.

[37] P. Zhang, L.-J. Gui, Z.-J. Fan, Q. Yu, and Z.-K. Li, “Finite element modeling of the quasi-static axial crushing of braided composite tubes,” *Comput Mater Sci*, vol. 73, pp. 146–153, Jun. 2013, doi: 10.1016/j.commatsci.2013.01.026.

[38] H. Zhou, W. Zhang, T. Liu, B. Gu, and B. Sun, “Finite element analyses on transverse impact behaviors of 3-D circular braided composite tubes with different braiding angles,” *Compos Part A Appl Sci Manuf*, vol. 79, 2015, doi: 10.1016/j.compositesa.2015.09.012.

[39] X. Ji *et al.*, “Multi-scale simulation and finite-element-assisted computation of elastic properties of braided textile reinforced composites,” *J Compos Mater*, vol. 48, no. 8, pp. 931–949, Apr. 2014, doi: 10.1177/0021998313480198.

[40] A. Shigang, Z. Xiaolei, M. Yiqi, P. Yongmao, and F. Daining, “Finite Element Modeling of 3D Orthogonal Woven C/C Composite Based on Micro-Computed Tomography Experiment,” *Applied Composite Materials*, vol. 21, no. 4, pp. 603–614, Aug. 2014, doi: 10.1007/s10443-013-9353-4.

[41] L. Zhang, D. Hu, R. Wang, Y. Zeng, and C. Cho, “Establishing RVE model composed of dry fibers and matrix for 3D four-directional braided composites,” *J Compos Mater*, vol. 53, no. 14, pp. 1917–1931, Jun. 2019, doi: 10.1177/0021998318815735.

[42] R. Wang, L. Zhang, D. Hu, and C. Cho, “Evaluation of three unit cell models in predicting the mechanical behaviour of 3D four-directional braided composites,” *J Compos Mater*, vol. 51, no. 27, pp. 3757–3767, Nov. 2017, doi: 10.1177/0021998317692657.

[43] J. J. Gou, W. Z. Fang, Y. J. Dai, S. Li, and W. Q. Tao, “Multi-size unit cells to predict effective thermal conductivities of 3D four-directional braided composites,” *Compos Struct*, vol. 163, pp. 152–167, Mar. 2017, doi: 10.1016/j.compstruct.2016.12.034.

[44] Y.-B. Wang, Z.-G. Liu, L. Hu, and Z. Wu, “Predicting the Elastic Modulus of 3D Braided Composite Tubes Using Geometrical Mapping Approach,” *21st International Conference on Composite Materials, Xi’an*, 2017.

[45] K. Dong, J. Zhang, L. Jin, B. Gu, and B. Sun, “Multi-scale finite element analyses on the thermal conductive behaviors of 3D braided composites,” *Compos Struct*, 2016, doi: 10.1016/j.compstruct.2016.02.029.

[46] Y. H. Chen and M. H. Aliabadi, “Meshfree-based micromechanical modelling of twill woven composites,” *Compos B Eng*, p. 108190, May 2020, doi: 10.1016/j.compositesb.2020.108190.

[47] D. Zhang *et al.*, “Finite Element Analysis of Mesh Size Effect of 3D Angle-Interlock Woven Composites Using Voxel-Based Method,” *Applied Composite Materials*, vol. 25, no. 4, pp. 905–920, Aug. 2018, doi: 10.1007/s10443-018-9723-z.

[48] M. Ghaedsharaf, J. E. Brunel, and L. L. Lebel, "Fiber-level numerical simulation of biaxial braids for mesoscopic morphology prediction validated by X-ray computed tomography scan," *Compos B Eng*, vol. 218, p. 108938, Aug. 2021, doi: 10.1016/J.COMPOSITESB.2021.108938.

[49] X. Wang, G. Zhang, X. Shi, and C. Zhang, "Modeling method of irregular cross section annular axis braided preform based on finite element simulation:," *https://doi.org/10.1177/15589250211037243*, vol. 16, p. 155892502110372, Jul. 2021, doi: 10.1177/15589250211037243.

[50] K. Xu, X. Qian, D. Duan, B. Chen, and L. Guo, "A novel macro-meso finite element method for the mechanical analysis of 3D braided composites," *Mechanics of Materials*, vol. 126, pp. 163–175, Nov. 2018, doi: 10.1016/J.MECHMAT.2018.08.007.

[51] "Finite Element Method (FEM) Model Verification and Validation for Bridges, Buildings and other Structures with Resensys Wireless SenSpot TM Sensors Measurements", Accessed: Jun. 12, 2022. [Online]. Available: https://www.engineering.com/DesignSoftware/DesignSoftwareArticles/ArticleID/11356/ Verifying-Your-Finite-

[52] G. W. Melenka and J. P. Carey, "Braid CAM: Braided composite analytical model," *SoftwareX*, vol. 7, pp. 23–27, Jan. 2018, doi: 10.1016/J.SOFTX.2017.12.004.

[53] S. C. Quek, A. M. Waas, K. W. Shahwan, and V. Agaram, "Analysis of 2D triaxial flat braided textile composites," *Int J Mech Sci*, vol. 45, no. 6–7, pp. 1077–1096, Jun. 2003, doi: 10.1016/J.IJMECSCI.2003.09.003.

[54] G. Fang and J. Liang, “A review of numerical modeling of three-dimensional braided textile composites,” *J Compos Mater*, vol. 45, no. 23, pp. 2415–2436, Nov. 2011, doi: 10.1177/0021998311401093.

[55] L. Ge, H. Li, J. Zhong, C. Zhang, and D. Fang, “Micro-CT based trans-scale damage analysis of 3D braided composites with pore defects,” *Compos Sci Technol*, vol. 211, p. 108830, Jul. 2021, doi: 10.1016/J.COMPSCITECH.2021.108830.

[56] Y. Li, B. Sun, and B. Gu, “Impact shear damage characterizations of 3D braided composite with X-ray micro-computed tomography and numerical methodologies,” *Compos Struct*, vol. 176, pp. 43–54, Sep. 2017, doi: 10.1016/J.COMPSTRUCT.2017.04.067.

[57] Z.-J. Li, H.-L. Dai, Z.-G. Liu, and Y. Wang, “Micro-CT based parametric modeling and damage analysis of three-dimensional rotary-five-directional braided composites under tensile load,” *Compos Struct*, vol. 309, p. 116734, Apr. 2023, doi: 10.1016/J.COMPSTRUCT.2023.116734.

[58] R. Hambli, “Micro-CT finite element model and experimental validation of trabecular bone damage and fracture,” *Bone*, vol. 56, no. 2, pp. 363–374, Oct. 2013, doi: 10.1016/J.BONE.2013.06.028.

[59] S. J. Shefelbine *et al.*, “Prediction of fracture callus mechanical properties using micro-CT images and voxel-based finite element analysis,” *Bone*, vol. 36, no. 3, pp. 480–488, Mar. 2005, doi: 10.1016/J.BONE.2004.11.007.

[60] N. Verdonschot, J. Stolk, and C. M. Kreulen, “Generation of 3-D Finite Element Models of Restored Human Teeth Using Micro-CT Techniques Oropharyngeal candidiasis as a maker for HIV infection View project Interface Mechanics in Hip Replacements View project,”

2001, Accessed: Apr. 08, 2023. [Online]. Available: https://www.researchgate.net/publication/11837381

[61] S. V. N. Jaecques *et al.*, “Individualised, micro CT-based finite element modelling as a tool for biomechanical analysis related to tissue engineering of bone,” *Biomaterials*, vol. 25, no. 9, pp. 1683–1696, Apr. 2004, doi: 10.1016/S0142-9612(03)00516-7.

[62] J. H. Lee, G. Y. Lee, J. J. Rha, J. H. Kim, and J. H. Cho, “Analysis of Microstructure Evolution and Mechanical Properties during Compression of Open-Cell Ni-Foams with Hollow Struts Using Micro-CT and FEM,” *Materials 2022, Vol. 15, Page 124*, vol. 15, no. 1, p. 124, Dec. 2021, doi: 10.3390/MA15010124.

[63] L. D’Andrea *et al.*, “Mechanical Properties of Robocast Glass Scaffolds Assessed through Micro-CT-Based Finite Element Models,” *Materials 2022, Vol. 15, Page 6344*, vol. 15, no. 18, p. 6344, Sep. 2022, doi: 10.3390/MA15186344.

[64] M. Basista, W. Węglewski, K. Bochenek, Z. Poniżnik, and Z. Nowak, “Micro-CT Finite Element Analysis of Thermal Residual Stresses and Fracture in Metal-Ceramic Composites,” *Adv Eng Mater*, vol. 19, no. 8, p. 1600725, Aug. 2017, doi: 10.1002/ADEM.201600725.

[65] S. Ai, W. Song, and Y. Chen, “Stress field and damage evolution in C/SiC woven composites: Image-based finite element analysis and in situ X-ray computed tomography tests,” *J Eur Ceram Soc*, vol. 41, no. 4, pp. 2323–2334, Apr. 2021, doi: 10.1016/J.JEURCERAMSOC.2020.12.026.

[66] M. Khormani, V. R. Kalat Jaari, I. Aghayan, S. H. Ghaderi, and A. Ahmadyfard, “Compressive strength determination of concrete specimens using X-ray computed

tomography and finite element method," *Constr Build Mater*, vol. 256, p. 119427, Sep. 2020, doi: 10.1016/J.CONBUILDMAT.2020.119427.

Chapter 3. Generating Geometrical Models for Tubular Braided Composites

A version of this Chapter was published and presented as:

Gholami, Ali, and Garrett W. Melenka. "Generating geometrical models for tubular braided composites." CSME Conf. Charlottetown, PE, Canada. 2021.

Abstract—This paper develops a program named TBC-Gen to generate geometrical models of Tubular Braided Composites (TBCs). TBC-Gen is a free and open-source program that does not require the user to deal with the relevant equations or have a deep knowledge of the manufacturing of TBCs. The MATLAB and SolidWorks software packages are combined to generate the solid models. The step-by-step process for generating different 2D TBC patterns and the relevant models are shown. The program's output is compared against that of commercial software and micro-computed tomography results.

Keywords: Tubular Braided Composite; Geometrical Model

3.1 Introduction

Composite materials constitute two or more materials with different mechanical properties. Combining these materials improves mechanical properties that none can provide individually [1]. Braided composites are continuous fiber-based reinforced materials used in various industries, from aerospace, automotive, petroleum, and building to medical treatments, sporting and marine [2], [3], [4]. They can be used in a rope to reinforce hoses, pipes, or medical catheters [5]. For more than 200 years, braiding has been used to produce textile fabrics [2]. Braided composites have significant advantages compared to conventional laminate composites, such as better out-of-plane stiffness, strength, toughness properties, net-shape fabrication, lower fabrication cost, impact and delamination resistance, and high performance [6], [7]. Because of these advantages, the studies in analyzing and manufacturing braided composite and their application are increasing significantly.

There are different types of braided composite: two-dimensional, three-dimensional, and multidirectional. Each of these types can be produced as flat or tubular shapes. In two-dimensional braided composites, yarns are interlaced only in one plane, and the preform can be flat or tubular. Two-dimensional (2D) braided composites can be produced using a Maypole braider. In a triaxial two-dimensional braided composite, additional yarns are interwoven between two-dimensional braids and directed alongside the axial braided composite [8]. One way to categorize 2-D braided composites is based on the assembly pattern of yarns. Different patterns of braided composites will be made depending on the arrangement and movement of carriers. The patterns of the braided composites are diamond (one tow passing above and then below the other tows, 1/1) Figure 3-1 a), regular (two tows passing above and then below the other tows, 2/2) Figure 3-1 b), and Hercules (three tows passing above and then below the other tows 3/3) Figure 3-1 c).

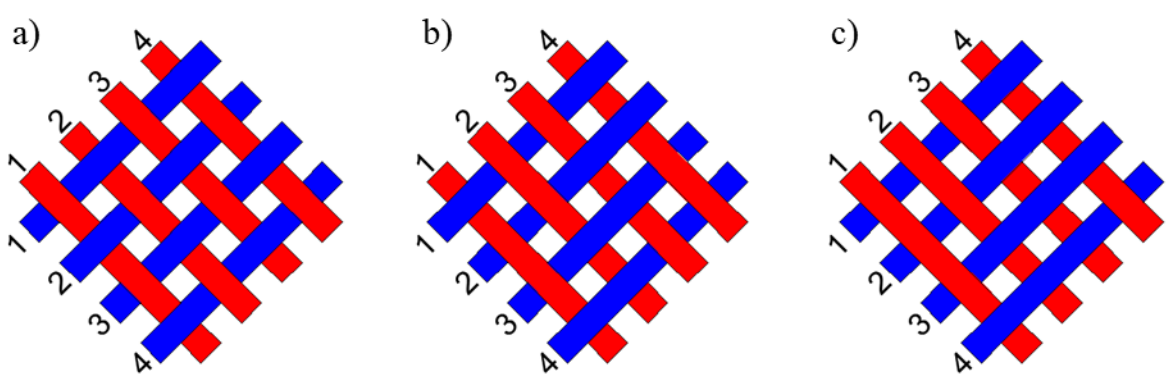

Figure 3-1 Different pattern of braided composite (a): 2-D Diamond (one by one), (b): 2-D Regular (two by two), (c) 2-D Hercules (three by three)

Tubular Braided Composites (TBC) have several variables, such as variable geometry, variable constituents, and non-uniform features of braided composites. Thus, the characterization of braided composites is not an easy task. However, knowing the mechanical properties is paramount to optimize the TBC's current application and introduce new applications. Also, more accurate geometrical models are needed to obtain the mechanical properties of braided composites accurately. Some geometrical variables of a regular braided composite pattern within a unit cell are shown in Figure 3-2. The shown variables are braid angle, yarn width, and undulation length. Braid angle is the most critical geometrical variable that significantly affects the mechanical properties of the TBC. Other parameters that affect the TBC's mechanical properties, such as the radius of the mandrel and the number of yarns, will be introduced in the following sections.

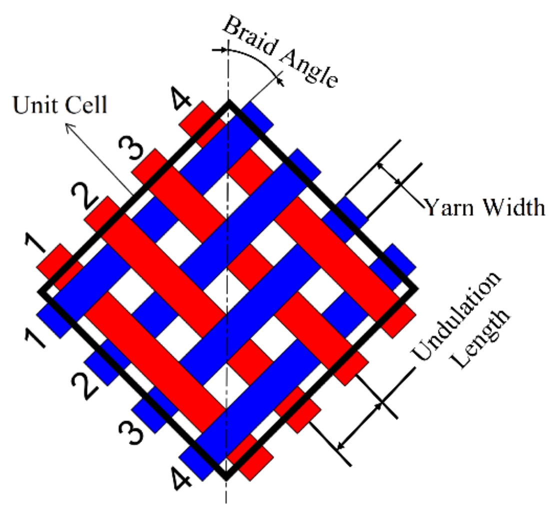

Figure 3-2 A unit cell of a regular braided composite pattern showing geometrical variables.

Several studies have tried to provide more mathematically accurate models for tubular braided composites. Liao and Adanur [9] developed an external and an internal three-dimensional circular braid model. They used the Frenet frame technique to sweep the cross-section over the yarn path. Rawal and Potluri [10], [11] developed an algorithm to produce three-dimensional braided preforms over different mandrel cross-sections: cylinder, square prism, cones with a circular and elliptical cross-section, and square pyramid. The yarn paths are modelled as straight lines, and undulation is ignored in their model. Alpyildiz [12] proposed a 3-D geometrical model for tubular braids. The researcher considered the braiding yarn's crimp together with the tubular curvature of the tubular braid structure in the model. The provided model worked with different braid structures, braid angles, the number of yarns in a set, yarn, and mandrel diameter. Rawal et al. [13] developed geometrical models in both cylindrical and conical mandrels with diamond, regular and triaxial forms. They used the Virtual Reality Modeling Language (VRML) to simulate the model. Finally, the model was verified against the results of a virtual experiment.

This paper will introduce the TBC-Gen program for designing and illustrating the geometrical model of TBC. The developed algorithm can be used as a step for generating a comprehensive geometrical model for future finite element modelling (FEM). Even though the geometrical models are made based on several assumptions that will add errors to the simulation results, having them will make a good benchmark against other experimental geometrical models like micro-computed Tomography (μCT).

3.2 Geometrical Equations

While the geometrical equations must be as accurate as possible and easy to implement, they should be realistic enough to provide precise models simulating the tubular braided composite's actual shape and behaviour. However, creating a geometrical model without making assumptions is not possible. For the geometrical model used in this paper, the following assumptions have been made [11]:

- The cross-section of the yarn is assumed to be circular with r radius

- The braid paths do not slip and keep the constant sinusoidal pattern throughout the braid length
- There is no compression on the yarns, so the yarn cross-sections are constant
- The longitudinal yarn in triaxial braided composites is straight

The assumptions above consider TBC's overall characteristics; however, they ignore some specifications, such as the flexible nature of yarn paths and variant cross-section shapes. Other methods like μCT, which can provide an actual experimental model, can be used to consider these specifications.

Depending on the braided composite pattern, different equations would be needed to model it. However, since all the patterns follow a uniform helical path along the mandrel, the helical path equations for different patterns would be the same. A left-hand (clockwise from top view) helix's general equations for a yarn path around a cylindrical mandrel are shown in Equation 3-1.

$$X_{cw} = R\cos\theta$$
$$Y_{cw} = R\sin\theta \qquad \text{Equation 3-1}$$
$$Z_{cw} = R\theta\cot\alpha$$

Where X_{cw}, Y_{cw}, and Z_{cw} are coordination points in x, y, and z directions, R is the helix's radius, θ is the winding angle, and α is the braid angle. For having the right-hand (counterclockwise from the top view) helical path, the sign of the Y should be changed, as shown in Equation 3-2.

$$X_{ccw} = R\cos\theta$$
$$Y_{ccw} = -R\sin\theta \qquad \text{Equation 3-2}$$
$$Z_{ccw} = R\theta\cot\alpha$$

A sample of clockwise and counterclockwise helix path with helix radius (R) = 10 mm, braid angle (α) = 45°, and winding angle (θ) between 0 and 4π, are shown in Figure 3-3.

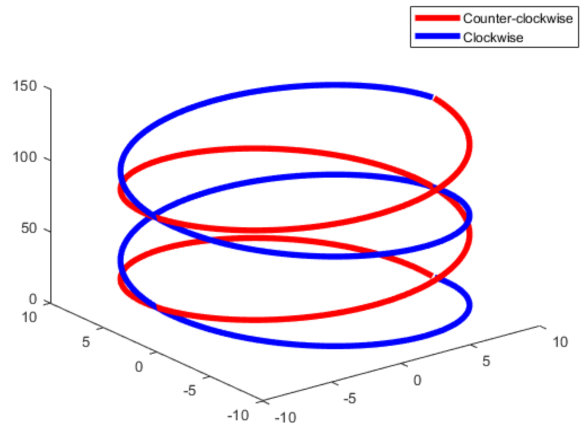

Figure 3-3 A clockwise and counterclockwise helix with R = 10 mm, α = 45°, and 0<θ≤4π

The helix shown in Figure 3-3 is for two periods (4π). To calculate the height of the helix, one needs to calculate the maximum Z, which, in this case it, would be $10\,mm\ \times 4\pi \times\ \cot 45° = 125.66\,mm$.

On the other hand, each yarn path follows a sinusoidal path based on its braiding pattern. The equation relating the number of yarns, the radius of the strand, and the winding angle to the sinusoidal yarn path is shown in Equation 3-3 [11].

$$S(\theta) = r \sin\left(\frac{N\theta}{2}\right) \qquad \text{Equation 3-3}$$

Where r is the radius of the yarn and N is the total number of yarns. The undulation path of a sinusoidal path with $r = 0.5\,mm$, $N = 2$, and $0 < \theta \leq 2\pi$ is shown in Figure 3-4.

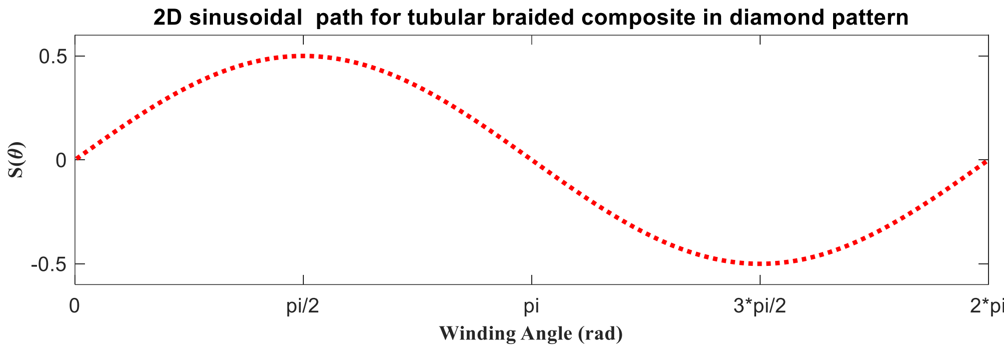

Figure 3-4 General sinusoidal path of yarn path with r=0.5 mm, N=2, and 0<θ≤2π

For a complete set of tubular braided composite, two sets of sinusoidal equations are required for counterclockwise and clockwise directions ($S_1(\theta)$ and $S_2(\theta)$). To do so, a π phase shift should be considered for the equations.

For having the complete yarn path of braided composite, with helix shape and including the undulations, Equation 3-1 and Equation 3-2 should be mixed with the relevant version of equations Equation 3-3. By doing so, Equation 3-4 and Equation 3-5 are created for counterclockwise and clockwise yarn paths, respectively.

$$\begin{aligned} X_i &= \left(R + S_1(\theta)\right)\cos(\theta + (i-1)\beta) && i = 1,2 \ldots n \\ Y_i &= \left(R + S_1(\theta)\right)\sin(\theta + (i-1)\beta) && i = 1,2 \ldots n \\ Z_i &= R\theta\tan\alpha && i = 1,2 \ldots n \end{aligned} \qquad \text{Equation 3-4}$$

$$\begin{aligned} X_i &= \left(R + S_2(\theta)\right)\cos(\theta + (i-1)\beta) && i = 1,2 \ldots n \\ Y_i &= -\left(R + S_2(\theta)\right)\sin(\theta + (i-1)\beta) && i = 1,2 \ldots n \\ Z_i &= R\theta\tan\alpha && i = 1,2 \ldots n \end{aligned} \qquad \text{Equation 3-5}$$

Where n is the total number of yarns at each direction (i.e., $n = N/2$) and β is the shift angle and is calculated as the angle between each two strands (i.e., $\beta = 2\pi/n$). These equations are the same for all patterns of TBC. The only factors that make the difference between yarn patterns are $S_1(\theta)$ and $S_2(\theta)$ which will be discussed in the next sections.

3.2.1 Diamond Pattern

The diamond pattern is the most straightforward pattern of the tubular braided composite because the whole path is sinusoidal, and no flat section is incorporated into the path. The $S_1(\theta)$ and $S_2(\theta)$ which represent counter-clockwise and clockwise sinusoidal paths, are as follows:

$$S_1(\theta) = r\sin\left(\frac{N\theta}{2} + \frac{\pi}{2}\right) \quad \text{Equation 3-6}$$

$$S_2(\theta) = r\sin\left(\frac{N\theta}{2} + \frac{3\pi}{2}\right) \quad \text{Equation 3-7}$$

A sample of the sinusoidal path of diamond pattern with $r = 0.5\ mm$, $N = 2$, and $0 < \theta \leq 2\pi$ is shown in Figure 3-5.

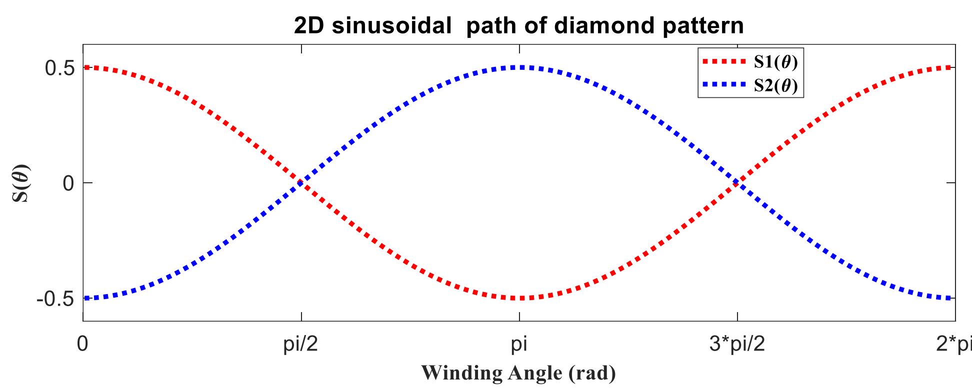

Figure 3-5 Counterclockwise (red) and clockwise (blue) undulation path of diamond pattern

A sample of diamond braided composite yarn path (counterclockwise and clockwise) with pattern and $N = 32$, $R = 10\ mm$, $r = 0.5\ mm$, and $\alpha = 45°$ is shown in Figure 3-6 (only one of the yarn at each direction is shown for more clarity).

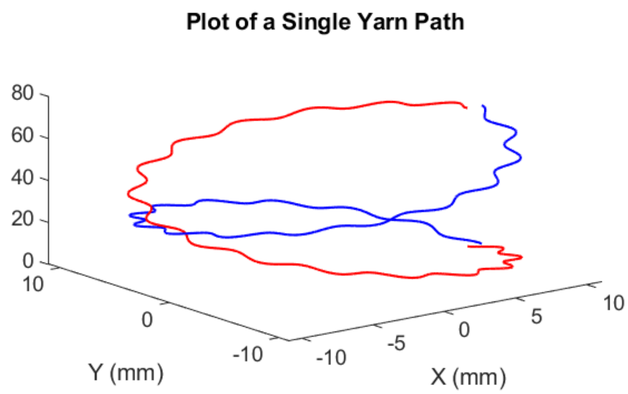

Figure 3-6 Clockwise (blue) and counterclockwise (red) yarn path of diamond patterns with N=32, R=10 mm, r=0.5 mm, and α=45°

3.2.2 Regular Pattern

The shape of the regular pattern is based on the diamond pattern. In the regular pattern, each yarn passes over two yarns, moving in the other direction and under two others. Because of that, they involved a flat section for the distance between yarns. The transient area-going from the top of two yarns to the under the two following and vice versa- is still covered by the sinusoidal equations shown in the previous section. A sample of a regular yarn path with $r = 0.5\ mm$, $N = 2$, and $0 < \theta \leq 4\pi$ is shown in Figure 3-7.

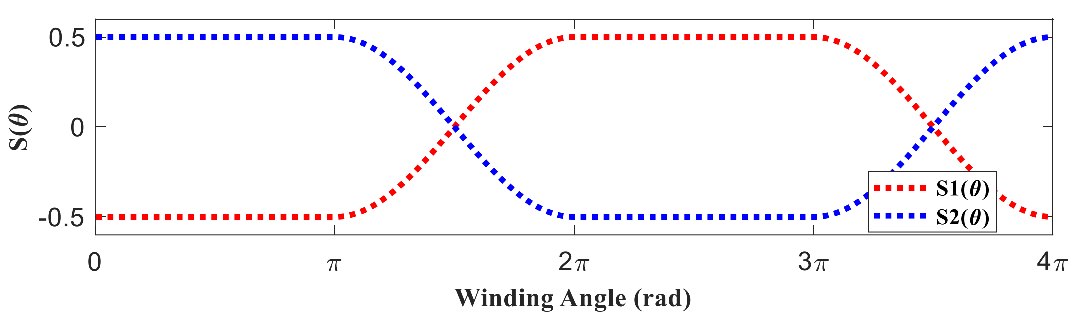

Figure 3-7 Counterclockwise (red) and clockwise (blue) undulation path of regular pattern with r=0.5 mm, N=2, and 0<θ≤4π

The counter-clockwise and clockwise equations for the undulation path of the regular pattern are shown in Equation 3-8 and Equation 3-9, respectively.

$$S_1(\theta_j) = \begin{cases} r & ; 0 \le \theta_j < \beta/2 \\ -r \sin\left(\frac{N\theta_j}{2} + \frac{\pi}{2}\right) & ; \beta/2 \le \theta_j < \beta \\ -r & ; \beta \le \theta_j < 3\beta/2 \\ r \sin\left(\frac{N\theta_j}{2} + \frac{\pi}{2}\right) & ; 3\beta/2 \le \theta_j < 2\beta \end{cases} \quad \text{Equation 3-8}$$

$$S_2(\theta_j) = \begin{cases} -r & ; 0 \le \theta_j < \beta/2 \\ -r \sin\left(\frac{N\theta_j}{2} + \frac{3\pi}{2}\right) & ; \beta/2 \le \theta_j < \beta \\ r & ; \beta \le \theta_j < 3\beta/2 \\ r \sin\left(\frac{N\theta_j}{2} + \frac{3\pi}{2}\right) & ; 3\beta/2 \le \theta_j < 2\beta \end{cases} \quad \text{Equation 3-9}$$

Where $j = 0,1,2, \dots length(\theta)$.

By combining equations Equation 3-8 and Equation 3-9 with Equation 3-4 and Equation 3-5, respectively, the yarn path of the regular pattern will be achieved. A sample of braid yarn with a regular pattern, with $N = 16$, $\alpha = 30°$, $R = 10\ mm$, and $r = 0.5\ mm$ is shown in Figure 3-8 (only one of the yarns at each direction is shown for more clarity).

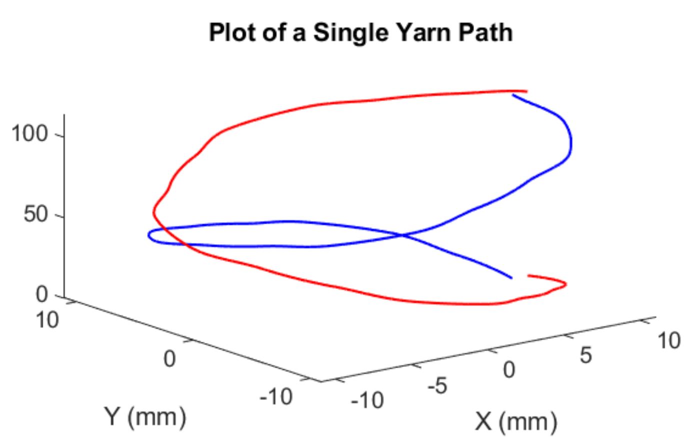

Figure 3-8 One clockwise (blue) and one counter-clockwise (red) yarn of a designed regular braid with N=16, α=30°, R=10 mm, and r=0.5 mm

3.2.3 Hercules Pattern

Hercules's pattern resembles regular and diamond patterns in sinusoidal and flat sections. However, since in the Hercules pattern, a yarn passes above three yarns and then goes under the following three yarns, the straight section is two times longer than the Regular pattern. A sample of the counterclockwise and clockwise undulation path of the Hercules pattern with $r = 0.5\ mm$, $N = 2$, and $0 < \theta \leq 6\pi$ is shown in Figure 3-9. As one can see, the flat sections are twice as long as the regular pattern. The sinusoidal undulations are the same as regular and diamond patterns.

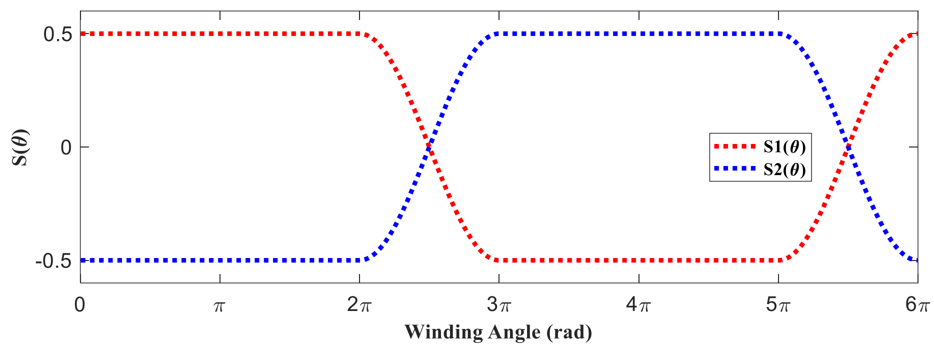

Figure 3-9 Counterclockwise (red) and clockwise (blue) undulation path of Hercules pattern with r=0.5 mm, N=2, and 0<θ≤6π

The counterclockwise and clockwise equations for the Hercules pattern's undulation path are shown in Equation 3-10 and Equation 3-11, respectively.

$$S_1(\theta_j) = \begin{cases} r & ; 0 \leq \theta_j < \beta/2 \\ r & ; \beta/2 \leq \theta_j < \beta \\ r\sin\left(\frac{N\theta_j}{2} + \frac{\pi}{2}\right) & ; \beta \leq \theta_j < 3\beta/2 \\ -r & ; 3\beta/2 \leq \theta_j < 2\beta \\ -r & ; 2\beta \leq \theta_j < 5\beta/2 \\ r\sin\left(\frac{N\theta_j}{2} + \frac{\pi}{2}\right) & ; 5\beta/2 \leq \theta_j < 3\beta \end{cases} \qquad \text{Equation 3-10}$$

$$S_2(\theta_j) = \begin{cases} -r & ; 0 \leq \theta_j < \beta/2 \\ -r & ; \beta/2 \leq \theta_j < \beta \\ r\sin\left(\frac{N\theta_j}{2} + \frac{3\pi}{2}\right) & ; \beta \leq \theta_j < 3\beta/2 \\ r & ; 3\beta/2 \leq \theta_j < 2\beta \\ r & ; 2\beta \leq \theta_j < 5\beta/2 \\ r\sin\left(\frac{N\theta_j}{2} + \frac{3\pi}{2}\right) & ; 5\beta/2 \leq \theta_j < 3\beta \end{cases} \qquad \text{Equation 3-11}$$

Similar to regular pattern equations, by combining Equation 3-10 and Equation 3-11 by equations Equation 3-4 and Equation 3-5, the equations for the Hercules pattern will be achieved. A sample of Hercules pattern with $N = 8$, $\alpha = 60°$, $R = 10\ mm$, and $r = 0.5\ mm$ is shown in Figure 3-10 (only one of the yarn at each direction is shown for more clarity).

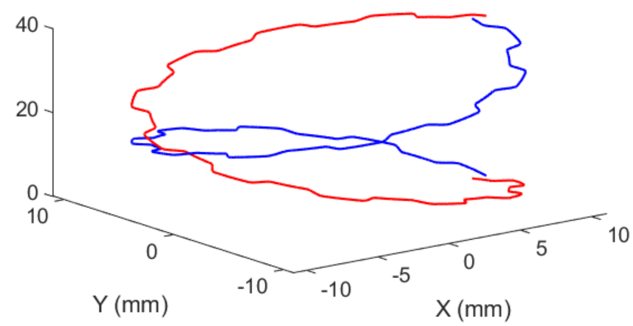

Figure 3-10 One clockwise (blue) and one counterclockwise (red) of a designed Hercules braid yarn path with N=8, α=60°, R=10 mm, and r=0.5 mm

3.3 TBC-Gen Program for Generating TBC Yarn Paths

Working with yarn path equations is complex, and implementing them is time-consuming. Also, it requires the user to have a good understanding of the fundamental math of complex equations. Because several variables are used in the equations, the user might not understand the effect of each parameter on the shape of the TBCs. To resolve these issues, a program named TBC-Gen is designed for this research using the MATLAB software package (R2020B, The MathWorks Inc, Natick, Ma, USA) to generate all the different patterns discussed in the previous sections. The TBC-Gen can generate different TBC models with various shapes and formats. The user of this program does not have to have a deep knowledge of the TBC manufacturing process and mathematical equations. It is easy to use for everyone with different backgrounds.

TBC-Gen needs five input geometrical variables to design the yarn path. Number of yarns, braid angle (in degree), the diameter of the mandrel in mm (inner diameter of the tubular braid, it should also be considered that the diameter of the mandrel is $2(R - r)$), the diameter of the strand $(2r)$ in mm, and the number of turns or height of the tubular braid in mm (only one of these two variables is required to be inputted, the other variable will be calculated based on the inputted value). This program can produce all three yarn patterns, i.e. Diamond, Regular, and Hercules. The user can select to see the single path of clockwise or counterclockwise yarn or both simultaneously. The updated path will automatically be displayed in the plot section as the user changes the parameters. The complete TBC path is displayed in a separate window, as shown in Figure 3-11 (b). Finally, the XYZ center points of the designed yarn path for counterclockwise and clockwise directions and a properties file, including the input parameters, the designed pattern, and date and time, can be exported as three separated text files by clicking on "Write to .txt file" button.

Created clockwise or counterclockwise yarn paths can be uploaded to the program, and the model can be generated and displayed in the program. The user can either upload the XYZ values, and the program will display the yarn paths associated with the data points, or they can upload the properties file, where the properties used to generate those yarn paths are stored. The program will create the data points based on the input properties. Figure 3-11 (a) shows the program's designed user interface.

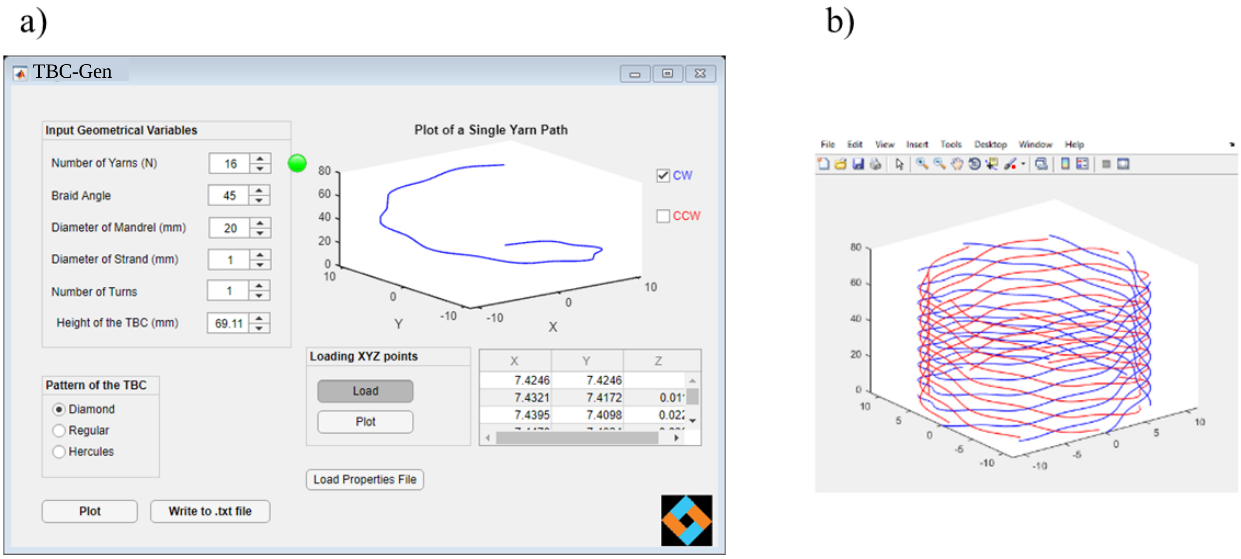

Figure 3-11 a) The interface of the TBC-Gen software for generating yarn path, b) The complete set of clockwise and counterclockwise yarn paths generated by TBC-Gen.

3.4 Generating the Solid Geometrical Model

The SolidWorks software (version 2020, Dassault Systèmes SOLIDWORKS Corp., Massachusetts, USA) is used to create the geometrical model by adding a cross-section to the designed yarn path in the previous section. One clockwise and one counterclockwise yarn path generated in MATLAB is imported into SolidWorks. The generated text file in the developed MATLAB program is imported into SolidWorks as the "Curve though XYZ Points…" function. After importing both yarn paths, two separate circular cross-sections are sketched in the XY plan while the circle's center coincides with the yarn path. Using the "Sweep" function, the cross-section sweeps the designed path and creates the yarn solid geometrical model. Finally, using the "Circular Pattern," n number of yarns are patterned around the TBC's axis for each counter-clockwise and clockwise direction. A sample TBC solid geometrical model from each pattern is shown in Figure 3-12. A diamond TBC with $N = 32$, $r = 0.5\ mm$, $R = 10\ mm$, and $\alpha = 45°$ is shown in Figure 3-12 a), a regular pattern TBC with $N = 36$, $r = 1\ mm$, $R = 15\ mm$, and $\alpha = 45°$ is shown in

Figure 3-12 b); and a Hercules TBC with $N = 64$, $r = 0.5\ mm$, $R = 10\ mm$, and $\alpha = 60°$ is shown in Figure 3-12 c)

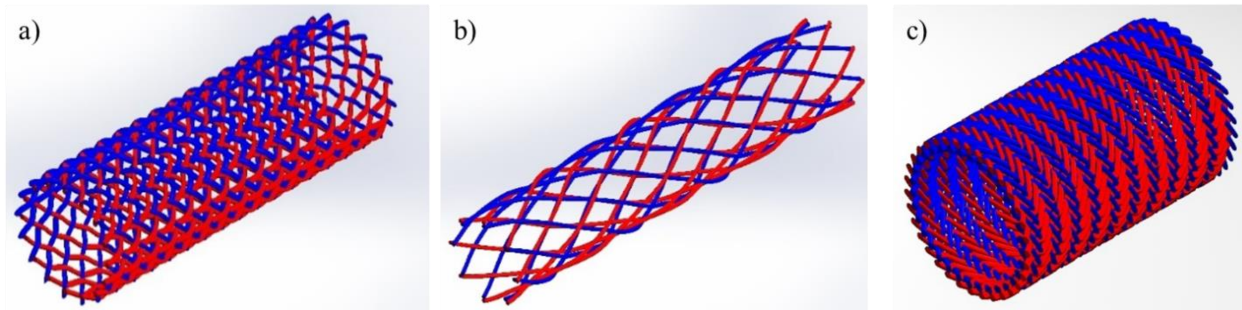

Figure 3-12 3-D solid model of a TBC, a) Diamond pattern with N=32, r=0.5 mm, R=10 mm, and α=45°, b) Regular with N=16, r=0.5 mm, R=10 mm, and α=30°, and c) Hercules with N=64, r=0.5 mm, R=10 mm, and α=60°

For validation of the developed model in this paper, a regular TBC with 16 yarns, braid angle = 35°, mandrel radius 10 mm, strand radius = 0.5 mm, and length of the TBC = 98.7 mm is designed in both the developed model in this paper and a commercial software package, TexMind Braided software [14]. The output results of the two software are shown in Figure 3-13. The visual comparison between the two models shows a good agreement between the two models.

a)

b)

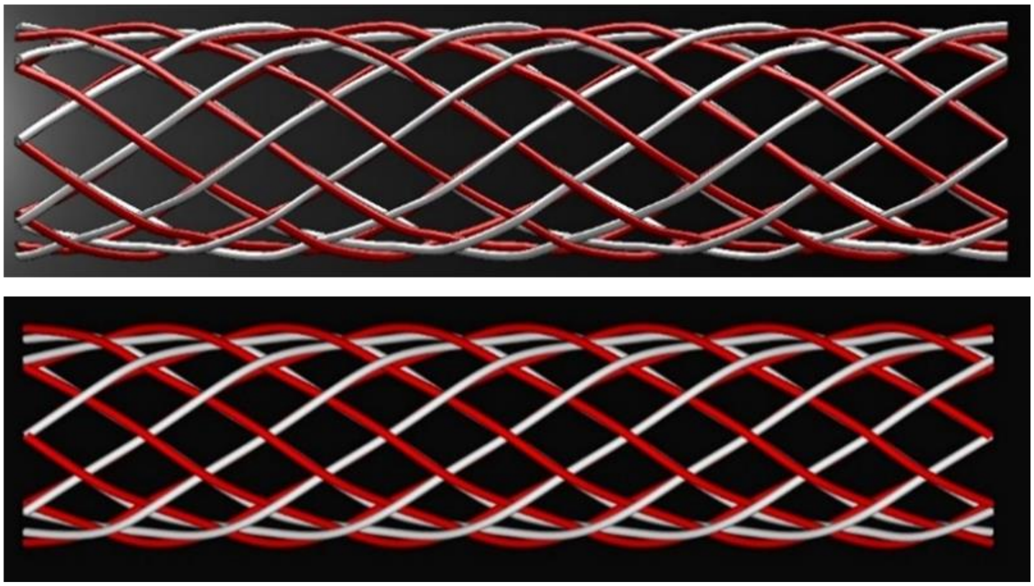

Figure 3-13 Comparing the result of the generated geometrical TBC model designed by the algorithm developed in this paper a), with the results of the same TBC designed in TexMind Braided software commercial software b). (N= 16, α = 35°, R = 10.5 mm, r = 0.5 mm, and

An actual TBC with the regular pattern is scanned with μCT, and the obtained image is shown in Figure 3-14 a). The parameters of this TBC are $N = 48$, $r = 0.44\ mm$, $R = 10\ mm$, and $\alpha = 40.53°$. These parameters are used to create the geometrical model of the TBC using the developed program in this paper, and the resulting image is shown in Figure 3-14 b). While the braid's overall shape is the same, as seen from the μCT image in Figure 3-14 b), some of the yarns are not located at their ideal path and are distorted significantly. Other assumptions made in generating geometrical equations are adding more errors to it. Further analysis is required for a quantitative comparison between the two models and the amount of error added because of the geometrical model's assumptions.

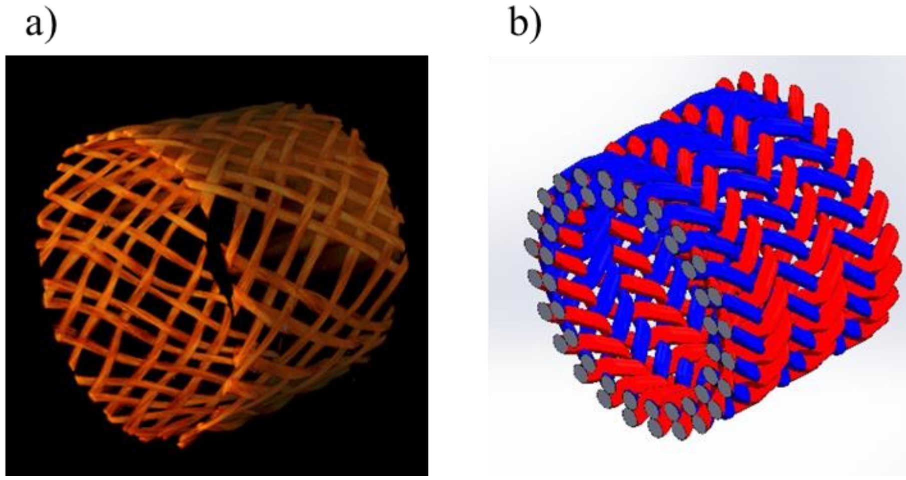

Figure 3-14 Comparison of a regular TBC's actual and simulation model. a) μCT image of a regular TBC with b) its geometrical model with N=48, r=0.44 mm, R=10 mm, and α=40.53°

3.5 Conclusion

This paper developed a program for generating TBC's geometrical model. MATLAB and SolidWorks were used to create the geometrical model. The results of this program were compared with the results of another software. Both results were in good accordance. Also, the program's result was compared against the result of a μCT image of an actual TBC. The error caused by the assumptions made while developing equations was obvious when comparing them.

The generated geometrical model can help the researchers and the industry better understand the TBC. This geometrical model can also be used (partially or entirely) to generate Finite Element Models (FEM) to study TBC's behaviour in different conditions. By developing such a simulation model, new applications for TBC will be introduced, and the current applications can be optimized.

3.6 References

[1] A. K. Kaw, *Mechanics of composite materials*. CRC press, 2005.

[2] C. Ayranci and J. Carey, “2D braided composites: A review for stiffness critical applications,” *Compos Struct*, vol. 85, no. 1, pp. 43–58, Sep. 2008, doi: 10.1016/J.COMPSTRUCT.2007.10.004.

[3] G. W. Melenka and J. P. Carey, “Development of a generalized analytical model for tubular braided-architecture composites,” *J Compos Mater*, vol. 51, no. 28, pp. 3861–3875, Dec. 2017, doi: 10.1177/0021998317695421.

[4] J. Carey, A. Fahim, and M. Munro, “Design of braided composite cardiovascular catheters based on required axial, flexural, and torsional rigidities,” *J Biomed Mater Res*, vol. 70B, no. 1, pp. 73–81, Jul. 2004, doi: 10.1002/jbm.b.30017.

[5] Y. Kyosev, *Recent developments in braiding and narrow weaving*. 2016.

[6] Z. M. Huang, “The mechanical properties of composites reinforced with woven and braided fabrics,” *Compos Sci Technol*, vol. 60, no. 4, pp. 479–498, Mar. 2000, doi: 10.1016/S0266-3538(99)00148-7.

[7] L. Xu, S. J. Kim, C.-H. Ong, and S. K. Ha, “Prediction of material properties of biaxial and triaxial braided textile composites,” *J Compos Mater*, vol. 46, no. 18, pp. 2255–2270, Aug. 2012, doi: 10.1177/0021998311431353.

[8] J. P. Carey, *Handbook of advances in braided composite materials: Theory, production, testing and applications*. Woodhead Publishing, 2016.

[9] Tianyi Liao and S. Adanur, “3D Structural Simulation of Tubular Braided Fabrics for Net-Shape Composites,” *Textile Research Journal*, vol. 70, no. 4, pp. 297–303, Apr. 2000, doi: 10.1177/004051750007000403.

[10] A. Rawal, P. Potluri, and C. Steele, “Prediction of Yarn Paths in Braided Structures Formed on a Square Pyramid,” *Journal of Industrial Textiles*, vol. 36, no. 3, pp. 221–226, Jan. 2007, doi: 10.1177/1528083707072354.

[11] A. Rawal, P. Potluri, and C. Steele, “Geometrical Modeling of the Yarn Paths in Three-dimensional Braided Structures,” *Journal of Industrial Textiles*, vol. 35, no. 2, pp. 115–135, Oct. 2005, doi: 10.1177/1528083705057574.

[12] T. Alpyildiz, “3D geometrical modelling of tubular braids,” *Textile Research Journal*, vol. 82, no. 5, pp. 443–453, Mar. 2012, doi: 10.1177/0040517511427969.

[13] A. Rawal, S. Gupta, H. Saraswat, and A. Sibal, “Geometrical modeling of near-net shape braided preforms,” *Textile Research Journal*, vol. 85, no. 10, pp. 1055–1064, Jun. 2015, doi: 10.1177/0040517514559587.

[14] Y. Kyosev, Y. Kyosev, and Schilgerius, *Topology-based modeling of textile structures and their joint assemblies*. Springer, 2019.

Chapter 4. Extracting Parameters of µct Scanned Open Mesh Tubular Braided Composite Materials' Yarn Using Image Processing Techniques

A version of this Chapter was published and presented as:

Gholami, Ali, and Garrett W. Melenka. "Extracting parameters of µCT scanned open mesh tubular braided composite materials' yarn using image processing techniques" CSME Conf. Sherbrooke, QC, Canada. 2023.

Abstract—In this paper, we present a segmentation algorithm for Tubular Braided Composite (TBC) materials that is demonstrated through its application on a simulated geometrical model. We also conduct a micro-computed tomography (µCT) scan on an open-mesh TBC and analyze and segment its images using the proposed method. Finally, we discuss the benefits and limitations of this approach.

Keywords-component: Tubular Braided Composite (TBC), Segmentation, Image Processing

4.1 Introduction

Tubular Braided Composites (TBC) are a group of composite materials characterized by an intertwined arrangement that enhances their structural integrity and makes them more damage-resistant. Some advantages of TBCs are out-of-plane strength, toughness, the ability to create complex shapes without excess material waste, reduced cost of manufacturing, and improved ability to withstand impacts and prevent separation of layers [1], [2]. Two sets of yarns are used to manufacture TBCs: clockwise and counterclockwise yarns. TBCs are usually produced in three patterns: Diamond, Regular, and Hercules [3]. The shapes of these patterns are shown in Figure 4-1.

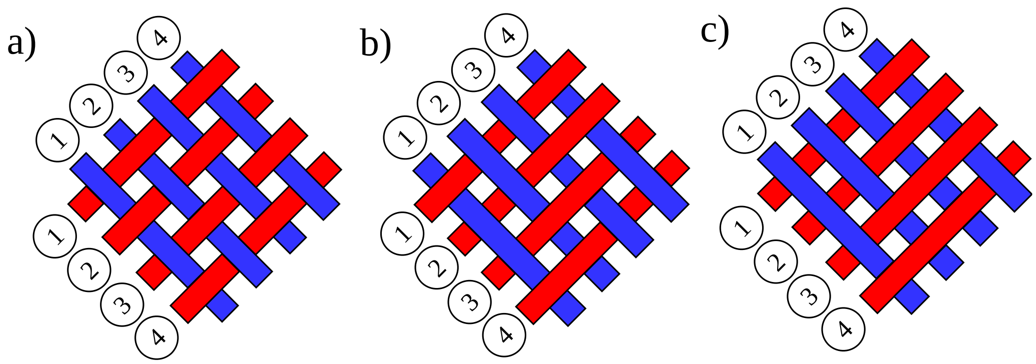

Figure 4-1 The patterns of the TBC, a) Diamond (one-by-one), b) Regular (two-by-two), and c) Hercules (three-by-three)

Another way to categorize TBCs is by defining them as open-mesh and closed-mesh. In open-mesh TBCs, there is a space between yarns, while in closed-mesh, the yarns are touching each other without a gap. Figure 4-2 shows a sample of open-mesh and closed-mesh TBCs.

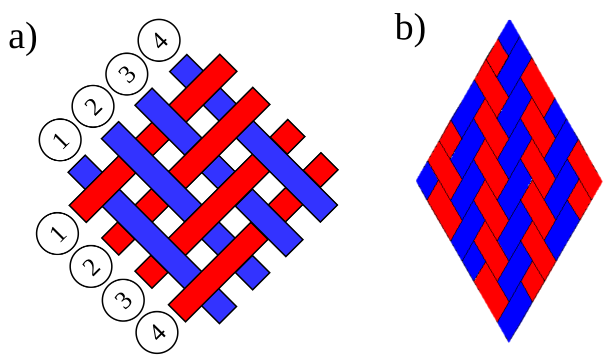

Figure 4-2 a) Open-mesh TBC, where there is a space between yarns, and b) closed-mesh TBC, where yarns are touching each other, and there is no space between them.

There have been efforts to find ways to simulate the TBC to optimize their performance and discover new applications [4], [5]. Alpyildiz [6] proposed a 3D geometrical model for TBCs with different structures that considers the crimp (the curved path that yarns follow) of the braiding yarn and tubular curvature, which can be applied to other braid structures and modified with changes in structural parameters. Rawal et al. [7] developed geometrical models of strand trajectories for

TBC, which can be applied to complex-shaped mandrels for near-net shape structures. Although the geometrical models are constructed based on certain assumptions, the flexible nature of TBCs often results in yarn distortion or movement during manufacturing, which introduces a source of error that simulated geometrical models cannot consider.

Micro-computed tomography (μCT) has been used to accurately evaluate TBC's structure and performance. Samal et al. [8] used μCT to examine the internal structure of a fiber-reinforced geopolymer composite subjected to mechanical impact. This research, a 3D model was utilized to evaluate the impact-induced damage in geopolymer composites reinforced with carbon, E-glass, and basalt fibers. Melenka and Gholami [9] used μCT to extract the geometrical properties of TBC fibers.

Because of the high accuracy of μCT, a high-resolution unit cell out of TBC was created. Gholami and Melenka [10] compared the geometrical model of TBC with their μCT based models and studied the error between them. Also, they modified the mathematical models and introduced new parameters to increase the likelihood of these two models.

Extracting the geometrical parameters of TBCs and analyzing their behaviour of them requires segmenting and separating the yarns. Segmentation of yarns is challenging because of the flexible nature of TBC. This paper will show a segmentation and separation model of yarns in TBCs. First, an algorithm to separate overlapping yarn cross-sections is developed and applied to a set of simulated TBC cross-sectional images created by the TBC-Gen program. Then, the overlapping yarns are separated, and their properties are extracted again. Next, the center points of detected yarns of the stack of images are discovered and connected, and the yarn paths of these models are extracted. After that, a μCT scan is done, and its cross-section is analyzed to segment the yarns.

For overlapping yarns, the previous algorithm separates them and extracts their parameters. Finally, the benefits and limitations of this method are discussed.

4.2 Methodology

4.2.1 Geometrical Models of TBCs

There are three patterns for TBCs, as shown in Figure 1, each with different modelling equations. The equations of each pattern are incorporated in the TBC-Gen program [10], and the models can be generated using this program. This program does not require the user to have a background in composite materials; the user only needs to input the geometrical variables. First, the yarn path of the selected pattern is created and shown in this program, and it can be exported as text files (two for clockwise and two for contour clockwise). Next, these text files can be imported into SolidWorks software packages (version 2022, Dassault Systems SOLIDWORKS Corp., Massachusetts, US). Then, the yarn cross-section is added to the yarn path to sweep it. Finally, two clockwise and two counterclockwise yarns are created and then copied around the mandrel axis to form the complete TBC.

4.2.2 Micro-Computed Tomography (μCT) Method

Micro Computed Tomography (μCT) is a Non-Destructive imaging technique to produce high-resolution 3D images of small objects. The basic principle of μCT is similar to that of medical CT. It involves taking a series of X-ray images from different angles and reconstructing them into a 3D image using computer algorithms. However, μCT uses much higher resolution detectors and X-ray sources to produce images with smaller voxel sizes.

The resolution of μCT images depends on the quality of the X-ray source and detector and the size of the voxels in the reconstructed image. Higher-resolution detectors and X-ray sources can achieve smaller voxel sizes, resulting in higher-resolution images. µCT has many applications in fields such as material science, biology, and engineering. For example, it can be used to study the internal structure of objects, visualize defects or cracks, and analyze the distribution of materials [11].

Figure 4-3 shows the fundamentals of µCT and the setup used to scan the TBCs. As shown there, the TBC is placed on a rotation stage, and X-rays are passed through it. As the TBC rotates, the X-ray detector captures a series of 2D X-ray images. These images are then processed using NRECON software (NRECON 1.7.1.0, Bruker, Belgium) to reconstruct 2D cross-sectional Images.

Next, these 2D cross-sectional images are imported into 3D Slicer software [12] (an open-source software created by a developer community) to create a 3D model. The 3D slicer software has the option for segmenting items. Therefore, the mandrel of the scanned TBC was segmented and removed.

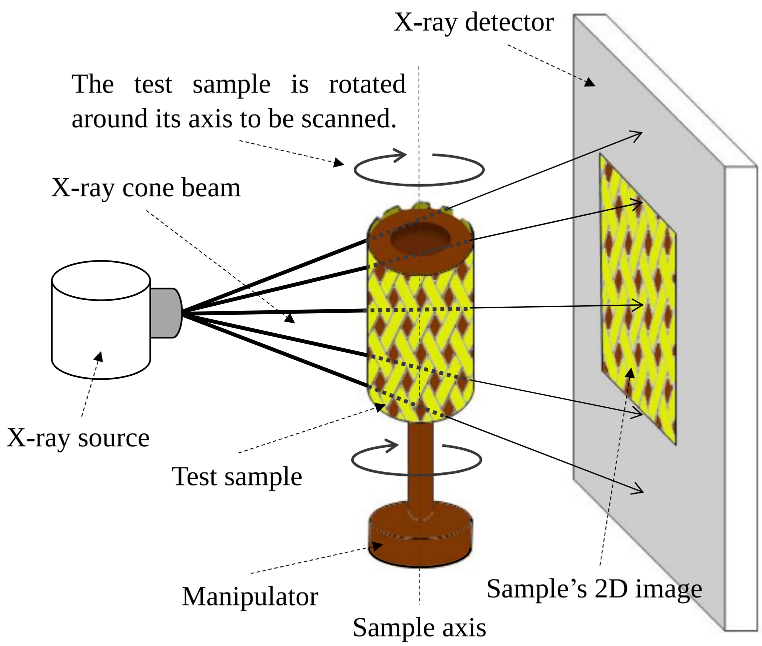

Figure 4-3 Fundamentals of μCT and the results of scanned TBC

4.2.3 Detecting Yarns of TBC

The reconstructed 2D cross-sectional images can be analyzed to segment the yarns. However, the segmentation of yarns might be challenging in some instances. Therefore, MATLAB software packages (R2022b The MathWorks Inc, Natick, Ma, USA) are used to process the cross-sectional images. An algorithm is developed in MATLAB to load the images, remove small unwanted objects using the *bwareaopen* function, close morphological images using the *imclose* function, trace region boundaries using the *bwboundaries* function, and extract parameters of the segmented sectors using the *regionprops* function.

Because of the flexible nature of the TBCs, the yarns sometimes intervene in each other's boundaries, making it difficult for the algorithm to separate them. Therefore, another algorithm is developed that recognizes the number of interfering yarns based on the value of the extracted area for the boundary and then segments them. Next, the center point, major and minor diameters, orientation, and area of the segmented yarns are extracted and stored. Finally, the yarns' extracted center points should be connected to form the yarn path. However, the order of the segmented yarns is not the same in each 2D cross-sectional image. Therefore, the distance between the center point and all the other extracted center points in the following image is measured to find the corresponding center point in the following image. The center point that shows the minimum distance is the corresponding center point to that specific center point. This algorithm is repeated for the rest of the center points to find the corresponding center points in the stack of images. Next, all the corresponding center points are connected, and the yarn paths are formed.

4.3 Results

4.3.1 Geometrical Image Results

Using the TBC-Gen program, a Regular TBC with 48 yarns, Braid angle = 40°, and the diameter of the yarn = 0.9 mm was generated. Then, two clockwise and two contour clockwise yarn paths were imported into SolidWorks. A circle with a 1mm diameter was added as the cross-section. The solid models of these four yarns were created and then copied around the mandrel's diameter to form the complete TBC. The cross-sectional images of these models with a 0.05 mm distance were captured and saved. Subsequently, the edited images were imported into MATLAB software packages, and the developed algorithm for segmenting yarns was applied to the cross-sections. Since the diameter of the TBC was 1 mm, and the designed yarn path was for a 0.9 mm yarn path, the cross-sections of yarns interfered. The designed simulated TBC was intended to simulate the interfering situation of the actual TBCs. The algorithm detected the interfering yarns as a single yarn. Therefore, it detected 24 boundaries. The interfering yarns were detected by comparing the area of the detected boundary to the average yarn area.

A line was drawn using the interfering yarns' center points and the detected boundary's extracted orientation. Next, the boundary is burned from the line, and the cross-section is divided into two yarns. Next, each part is analyzed again, and its properties, including the center points, the area, and the orientation of each section, are recorded. Figure 4-4 a) shows the detection and segmentation of the geometrical model's yarn.

The extracted center points need to be connected to form the TBC's yarn path. However, as explained in the previous section, the order of the detected center points is inconsistent with the cross-sectional image. Thus, the distance between each detected yarn path and all the detected yarn paths in the following cross-sectional images is measured.

Accordingly, the center point that shows the minimum distance is the corresponding center point for that yarn. After repeating this process for all the yarn cross-sections and all 2D images, the yarn path of each yarn is detected. The result is shown in Figure 4-4 b), where all 48 yarns are plotted, including 24 clockwise and 24 contour-clockwise yarns.

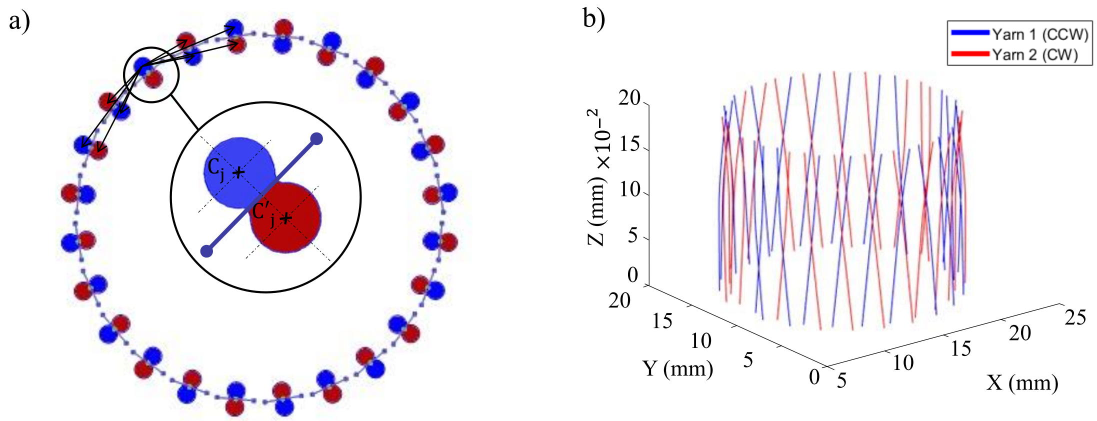

Figure 4-4 Segmentation of the geometrical model. a) detecting boundaries of the geometrical model and separating the interfering yarns (the distance between each center point and all of the center points in the following image is measured to find the corresponding yarn), b) connecting the detected center points and forming the yarn path of the TBC geometrical model

4.4 µCT Model's Results

A Regular Kevlar open-mesh TBC with 48 yarns and a 20 mm mandrel was scanned by µCT for this research. The braid angle and the yarn width of this TBC were measured using the image taken by a digital camera (Nikon Digital Camera D3500 with AF-P NIKKOR 18-55 mm 1:3.5-5.6G lens). The taken image is shown in Figure 4-5 a). 10 yarns were selected to measure yarn width and braid angle. The average value of these measurements was 0.88 mm and 40.53°, respectively. The setting of this scan is tabulated in Table 4-1. The pixel size of the obtained images in this scan was 10.88 µm. The 3D model of the scanned TBC was generated using the 3D Slicer software, and its results are shown in Figure 4-5 b). This Figure includes both the scanned TBC and the mandrel. The mandrel has been segmented and displayed with a different colour. Next, the mandrel is removed, and the TBC is shown in Figure 4-5 c).

Table 4-1 The setting of the µCT scan

μCT parameters	Value
Image pixel size	10.88 μm
Source Voltage	55 kV
Source Current	166 μA
Number of scanned Images	1533
Exposure	1876 ms
Rotation step	0.1°
Rotation angle	180°
Frame Averaging	4
Duration	4 hours and 35 minutes

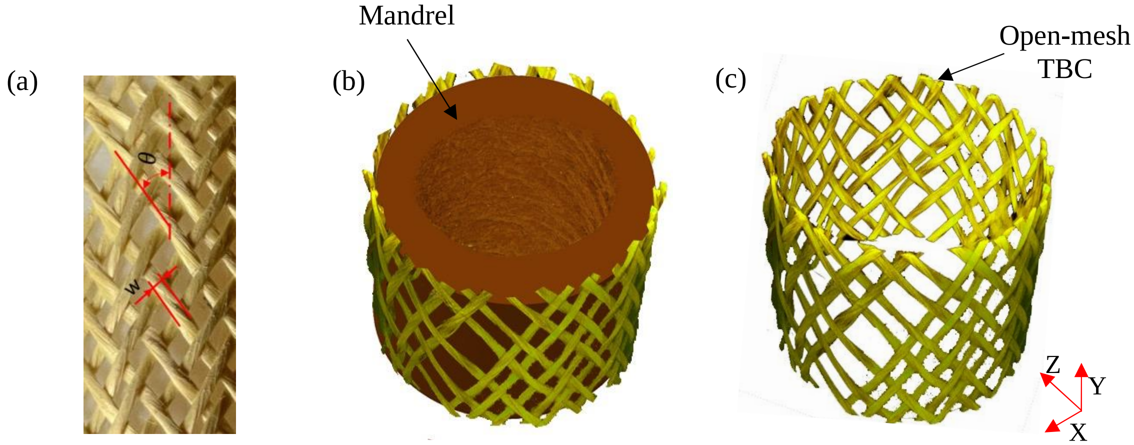

Figure 4-5 a) The actual open-mesh TBC with mandrel, b) the µCT scanned TBC with mandrel, c) the scanned TBC without the mandrel.

The 2D cross-sectional images were imported into MATLAB software packages, and the segmentation algorithm was applied. The results of the segmented images are shown in Figure 4-5 a). In this figure, the single yarns and their parameters (center point, major and minor diameter, area, and orientation) are detected. Sometimes, the yarns interfere, and the previous separating method is applied. Figure 4-6 shows the separation of the two overlapping yarns. The newly separated yarns are analyzed again, and their properties are extracted. The segmentation process of µCT cross sections is more challenging than the simulated geometrical model. One reason is the flexible nature of TBCs, making them move around and be distorted easily. Also, since the scanned TBC was not cured, the yarns could move freely during the scan and cutting, which makes the yarns less stable.

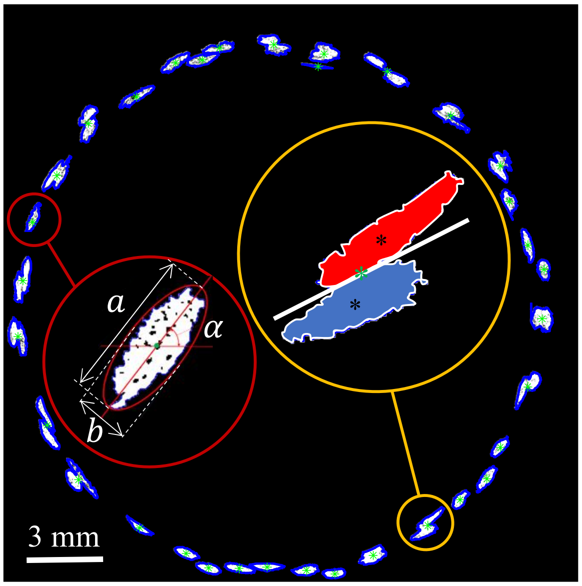

Figure 4-6 The results of the μCT scan. The detected boundaries and the single yarn detected and the parameters extracted. Also, interfering yarns, including two yarns, are detected, and the yarns are separated. a: major diameter, b: minor diameter, α:orientation

In some cases, more than two yarns interfere, making the segmentation process more challenging. Because of these issues, separating more than two interfering yarns is impossible with the current segmentation algorithm.

One of the TBCs was segmented manually, as shown in Figure 4-7. After the yarn is segmented in the entire stack of images, the center points of these two yarns and their other properties are extracted using a similar segmentation algorithm. Finally, their point is connected, and the yarn paths are generated and plotted.

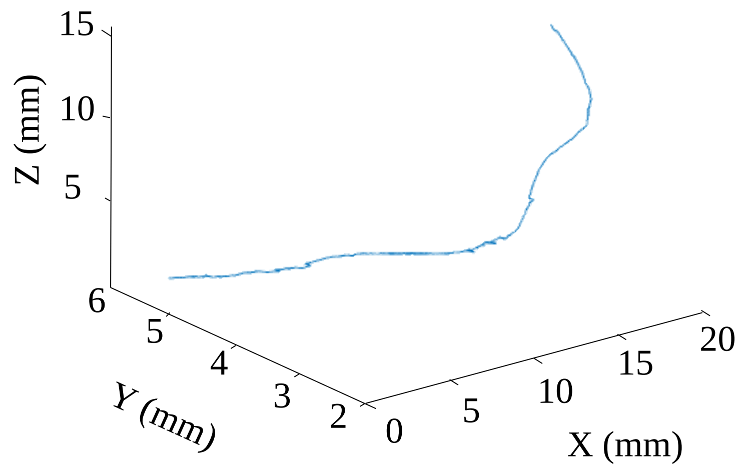

Figure 4-7 One of the extracted yarns out of the scanned TBC

4.5 Conclusion

The segmentation of the TBC yarns is challenging, but it is helpful to understand the behaviour of TBCs and study them more in-depth. This study is the initiation of the segmentation process. The algorithm proposed in this paper can detect the yarns' boundaries within the TBC cross-section. First, a sample geometrical model was created using the TBC-Gen program and the SolidWorks software. Then some 2D cross-sectional images were extracted from the model and imported into MATLAB. The boundaries of the yarns were detected, and their properties, including the center points, the major and minor diameters, orientation, and area, were extracted. Next, the average cross-section area of yarns was calculated, and if the area of the boundary was more than that average, it was recognized as the overlapping yarn with more than one yarn. Then, a line crossed from the center point, separating the two overlapping yarns. Next, the properties of the newly segmented yarns were extracted.

To form the yarn path, the extracted center yarns must be connected. However, since the order of the detected center points was not similar in all of the 2D images, another algorithm was designed to match the yarns in different cross-sections. This algorithm worked based on calculating the distance of the yarn compared to all of the other yarn centers in the following image.

A µCT test was done on a TBC, and an actual model was created. First, the segmentation algorithm was applied to the µCT model, and the properties of the single yarns were extracted. The algorithm successfully separated the overlapping yarns consisting of two yarns. However, because of the complex nature of TBCs, the algorithm could not separate boundaries comprised of more than two yarns. Then, two yarns were segmented manually, and their properties were extracted using the algorithm. Finally, the yarn paths were plotted and shown in this paper.

While this work is the initial step for segmenting the yarns, the preliminary results show excellent potential for improving this algorithm to automatize it and make it more robust. Furthermore, other image processing techniques, such as machine learning and artificial intelligence, might be useful in improving the segmentation of yarns. Finally, this algorithm can be helpful in different industries, including medical devices such as Stents and Catheters, because open mesh TBCs are used for them.

4.6 Acknowledgment

The authors would like to acknowledge the funding support of the Natural Sciences and Engineering Research Council of Canada (NSERC) RGPIN- 2018–05899.

4.7 References

[1] Z. M. Huang, "The mechanical properties of composites reinforced with woven and braided fabrics," *Compos Sci Technol*, vol. 60, no. 4, pp. 479–498, Mar. 2000, doi: 10.1016/S0266-3538(99)00148-7.

[2] L. Xu, S. J. Kim, C.-H. Ong, and S. K. Ha, “Prediction of material properties of biaxial and triaxial braided textile composites,” *J Compos Mater*, vol. 46, no. 18, pp. 2255–2270, Aug. 2012, doi: 10.1177/0021998311431353.

[3] A. Gholami and G. W. Melenka, “Generating Geometrical Models for Tubular Braided Composites,” *CSME Conference, Charlottetown, PE, Canada*, 2021, [Online]. Available: https://library.upei.ca/islandora/object/csme2021%253A102

[4] A. Gholami and G. W. Melenka, “Finite element analysis of 2-D tubular braided composite based on geometrical models to study mechanical performances,” *https://doi.org/10.1080/15376494.2021.2001879*, pp. 1–17, Nov. 2021, doi: 10.1080/15376494.2021.2001879.

[5] Y. Zhang, H. Li, Y. Gao, R. Lou, L. Ge, and D. Fang, “Multi-scale modelling and elastic properties prediction of 3D four-directional tubular braided composites,” *Compos Struct*, vol. 292, p. 115632, Jul. 2022, doi: 10.1016/J.COMPSTRUCT.2022.115632.

[6] T. Alpyildiz, “3D geometrical modelling of tubular braids,” *Textile Research Journal*, vol. 82, no. 5, pp. 443–453, Nov. 2011, doi: 10.1177/0040517511427969.

[7] A. Rawal, S. Gupta, H. Saraswat, and A. Sibal, “Geometrical modeling of near-net shape braided preforms,” *Textile Research Journal*, vol. 85, no. 10, pp. 1055–1064, Jun. 2015, doi: 10.1177/0040517514559587.

[8] S. Samal, M. Kolinova, H. Rahier, G. Dal Poggetto, and I. Blanco, “Investigation of the Internal Structure of Fiber Reinforced Geopolymer Composite under Mechanical Impact: A Micro Computed Tomography (μCT) Study,” *Applied Sciences 2019, Vol. 9, Page 516*, vol. 9, no. 3, p. 516, Feb. 2019, doi: 10.3390/APP9030516.

[9] G. W. Melenka and A. Gholami, "Fiber identification of braided composites using micro-computed tomography," *Composites Communications*, vol. 27, p. 100813, Oct. 2021, doi: 10.1016/j.coco.2021.100813.

[10] A. Gholami and G. W. Melenka, "Studying the geometrical models of tubular braided composite using micro computed tomography and particle swarm optimization," *Compos B Eng*, p. 110758, Apr. 2023, doi: 10.1016/J.COMPOSITESB.2023.110758.

[11] E. L. Ritman, "Current status of developments and applications of micro-CT," *Annu Rev Biomed Eng*, vol. 13, pp. 531–552, Aug. 2011, doi: 10.1146/ANNUREV-BIOENG-071910-124717.

[12] A. Fedorov *et al.*, "3D Slicer as an Image Computing Platform for the Quantitative Imaging Network," *Magn Reson Imaging*, vol. 30, no. 9, pp. 1323–1341, 2012, doi: 10.1016/j.mri.2012.05.001.

Chapter 5. Studying the Geometrical Models of Tubular Braided Composite Using Micro-Computed Tomography and Particle Swarm Optimization

A version of this Chapter was published as:

Gholami, Ali, and Garrett W. Melenka. "Studying the geometrical models of tubular braided composite using micro-computed tomography and particle swarm optimization." Composites Part B: Engineering 260 (2023): 110758.

Nomenclature

X_{ccw}	coordination of counter-clockwise yarn paths in the X direction
Y_{ccw}	coordination of counter-clockwise yarn paths in the Y direction
Z_{ccw}	coordination of counter-clockwise yarn paths in the Z direction
X_{cw}	coordination of clockwise yarn paths in the X direction
Y_{cw}	coordination of clockwise yarn paths in the Y direction
Z_{cw}	coordination of clockwise yarn paths in the Z direction
R	the radius of the helix
φ	the winding angle of the TBC helix
θ	braid angle measured relative to the braid longitudinal axis
$X0$	the offset of the mandrel's centre in the X direction
$Y0$	the offset of the mandrel's centre in the Y direction
$Z0$	the offset of the mandrel's centre in the Z direction
$S(\varphi)$	crimp path
n	number of yarns moving in one direction
N	total number of yarns
i	the counter between 1 to $n/2$
ω	shift angle of the TBC helix
σ	parameter vector of the geometrical model
$P_{g(\sigma)}$	yarn path of the geometrical model
v_i^k	speed of particles
X_i^k	position of particles
k	counter of repetition

pbest_i^k	the most optimal position of the particle i
gbest^k	the most optimal position of the swarm
C_1	Speed controlling variable
C_2	Speed controlling variable
r_1	Random numbers for PSO (between 0 and 1)
r_2	Random numbers for PSO (between 0 and 1)
β	Rotation angle

Abstract:

This paper compares the geometrical model of a 2DTBC with its actual model generated by the Micro-Computed Tomography (μCT) method. First, the geometrical models' equations are edited to simulate the manufacturing process more accurately, and the equations are incorporated into the TBC-Gen program. Then, a μCT scan is done on a cured carbon fiber TBC, and 2D and 3D models are created. Next, two yarns of the scanned models are extracted and modelled. The segmented yarns are analyzed, and their geometrical data, including cross-section area, major and minor yarn diameters, orientation, mandrel diameter, portion angle and centre points, are extracted. Next, a yarn path simulating the scanned yarn is generated using the TBC-Gen and the extracted parameters. Then, the generated geometrical model is compared with the μCT model. A parameter named portion angle is introduced to help the geometrical model better fit the μCT model. Finally, Particle Swarm Optimization (PSO) is used to optimize the rotation angle. The result of the fitting algorithm shows the accuracy of the geometrical model (less than 1% error) to simulate actual TBC. Understanding the amount of error between a geometrical model and the actual model will help to evaluate the application of geometrical models more thoroughly. Also, the more accurate geometrical model will contribute less error to the FEM simulation. The quantitative comparison between these two models can give a clear understanding of the amount of error existing in the geometrical model compared to an accurate model generated by μCT.

Keywords:

Braided Composite Material, Mico-CT, Geometrical model, Inverse Problem, Particle Swarm Optimization Algorithm

5.1 Introduction

Composite materials play an essential role in today's industry. The usage of composite materials ranges from aerospace to sport, marine to medical equipment, and home construction to the automobile industry [1], [2]. Furthermore, they are also used in disruptive industries because of the advanced features of composite materials, such as low weight, better corrosion resistance, higher strength and fatigue strength [3]. For example, as the automobile industry is shifting from an internal combustion engine (ICE) to an electrical vehicle (EV), composite materials are essential for reducing the weight of the vehicle and increasing the driving range [4].

Braided composites are a class of woven composite materials which consist of long fibers impregnated by a matrix. Because of the interwoven structure of the braided composites, they provide higher toughness compared to unidirectional laminate composites. On the other hand, because of the undulation of the yarns in braided composite, they show less stiffness than laminated composite [1]. Therefore, one of the essential steps for analyzing the behaviour of these materials and making simulation models is developing geometrical models.

Braids are described as two-dimensional (2D) or three-dimensional (3D) fabrics with even thread density and a closed fabric look, whose braiding threads cross one another in a diagonal direction to their edges, according to the German Industry Standard Din 60,000 [1]. In the 2D braids, the yarns are only woven in mandrel directions. However, in the 3D braids, another set of yarn is added in the through-thickness direction [5]. The 2D braids are manufactured with different patterns. Diamond, Regular, and Hercules are different patterns of 2D braids. In the Diamond pattern, the yarn is above the other yarn in a different direction and goes under the next one (the pattern is one by one). In the Regular pattern, the yarn moves on top of two yarns in the other direction and goes under the next two ones (the pattern is two by two). Finally, in the Hercules pattern, the yarn moves above three yarns in the other direction and goes under the following three yarns (the pattern is three by three). The shapes of these patterns are shown in Figure 5-1. Also, the angle between the axis of the mandrel and the yarns is known as the braid angle. The Regular pattern is the most common braid configuration among these three patterns because of its better mechanical properties.

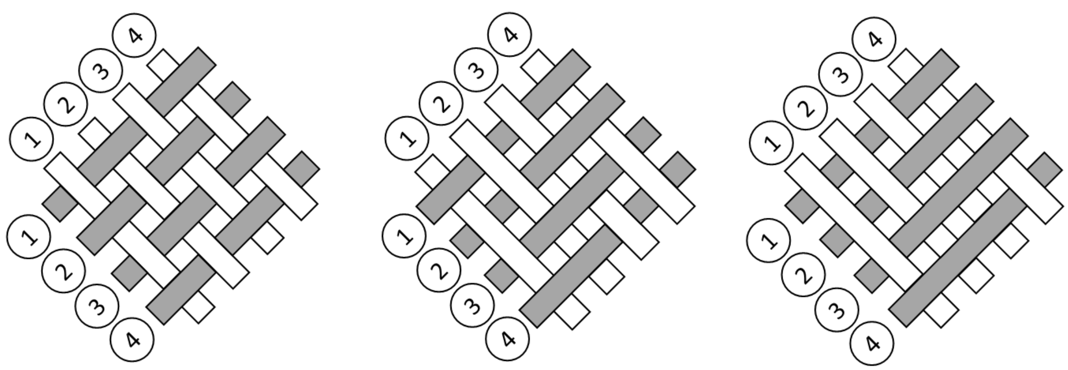

Figure 5-1 Different patterns of TBC a) Diamond, b) Regular, and c) Hercules

Rawal *et al*. [6] developed a geometrical model for three types of TBCs (Diamond, Regular, and Hercules). These models were able to fit cylindrical and conical mandrels. Alpyildiz [7] proposed a 3D model for Diamond and Regular 2D braids and Regular triaxial patterns. Kyosov [8] developed a geometrical model for a Regular tubular braided composite in which the direction of ridges was parallel to the axis of the TBC. Ning *et al*. [9] proposed a geometrical model based on a different mathematical model compared to the previous works. This paper uses the rose curve to develop the geometrical model. He *et al.* [10] proposed two methods for developing a rope model bent over a sheave. The first one is based on the mathematical method, where mathematical equations generate the yarn paths. The second method is developed based on braiding movement, and intersecting helical surfaces create the model by braiding surfaces. The accuracy of these models was not studied, and no error analysis against the actual model has been done.

These geometrical models can be used to provide the input model in simulation methods. Gholami and Melenka [11] developed a Finite Element Model (FEM) based on the geometrical model and compared the results with analytical and experimental results. Different sources of error contribute to the simulation models' accuracy. One of the primary sources of error is the imported geometrical model. If the imported model is more similar to the actual model, the FEM results would be more similar to the reality. One method for obtaining an actual geometrical model is using the μCT technique. Also, μCT has been used in different research to study braided composite materials in detail [12]–[14].

Li *et al.* [15] analyzed the shear fracture of 3D braided composites using μCT and compared the results with a developed FEM. In this research, several failure modes were categorized, and it was concluded that each failure mode depends on the geometry and structure of the braided composite. Wu *et al*. [16] compared the mechanical properties of two braided composite materials reinforced by aramid and carbon fiber. They used μCT to obtain the results of the tests and then compared them. The effect of the reinforced material on the resulting failure modes was also studied using the μCT. Gu *et al*.[17] studied the impact of braid angle on the damage and failure mechanism of 2D TBC by having a torsion experiment. The 3D Digital Image Correlation (DIC) records progressive torsional strain and crack propagation. Also, μCT measures the volume of damages and the torsional damage morphologies. Liu *et al.* [18] analyzed a 3D five-directional braided composite using μCT. A Representative Volume Element (RVE) was generated statistically by analyzing μCT data. The simulated model was fitted to the reference model to validate the ability of the generated model to capture appropriate compaction and torsion of yarns. Wu et al. [19] examined the impact of axial yarns on the damage behaviour of 2D TBC. The combination of Infrared thermography and μCT was used in this research. One method for comparing the geometrical and μCT models is developing an inverse problem and minimizing the Mean Square Error (MSE) between the models. In all of these studies, the geometrical models have not been fitted to the models created by μCT. Therefore, the accuracy of the currently available models has not been studied.

An inverse problem is a problem that analyzes the current observation to extract the parameters of the data. Depending on the nature of the problem, there may not be a unique solution for the problem. Different algorithms are used to solve an inverse problem. Tam *et al*. [20] used a combination of Genetic Algorithms (GA), Ant Colony Optimization (ACO), and PSO to extract the natural frequency of composite materials. Combining these algorithms eliminates each algorithm's disadvantages and takes advantage of each algorithm. Jianqiao *et al*. [21] used PSO and FEM to optimize the design of a pressure vessel made of composite structures. The proposed method provided good stability and efficiency in solving probabilistic optimization designs. Gholami *et al.* [22] solved an inverse problem to extract the parameters of ultrasonic waves. They used Particle Swarm Optimization (PSO) and Levenberg-Marquardt (LM) to solve the objective function.

In this paper, a generalized geometrical model is presented for 2D TBC. This generalized geometrical model can be shifted in X, Y, and Z directions. Also, a closed-mesh TBC will be scanned by μCT, and their yarns will be identified and segmented through image segmentation. Different image processing techniques are used to extract some of the parameters of the scanned μCT model and the extracted yarns. A new parameter (rotation angle) is defined to fine-tune the fitted model's accuracy. An inverse problem is designed to do that, and an objective function is defined between the extracted yarn path and a geometrical model. PSO algorithm is used to solve the designed objective function. The parameter that resulted in the minimum MSE is the global solution of the objective function.

An accurate geometrical model created by mathematical equations is essential for creating a precise FEM simulation model. The better the geometrical model presents the actual model (a model made out of μCT scan, for example), the less error is incorporated into the simulation FEM. Also, creating a geometrical model is less expensive and less time-consuming compared to creating an actual model through actual tests like micro-computed tomography. The capital cost of purchasing a μCT machine or renting one for the scan is substantially high. Also, because of the high resolution required, a large amount of data is captured after any scan, which causes high storage, computational, and time costs [23].

However, the amount of error in the geometrical model is unknown, and researchers do not know how much error it contributes to the model. Also, the acceptable error between the geometrical and actual models is unknown. In this research, a quantitative study is done on the geometrical model for TBC, and the errors between an actual model and a geometrical model with similar geometrical properties are compared. This process is done on a 2D TBC. However, it can be extended to 3D braided composites or other types of composite materials.

5.2 Method

5.2.1 Geometrical Model of TBC

The geometrical models for TBCs combine a helix curve and a crimp path. The Helix curve is similar for all three yarn patterns (Diamond, Regular, and Hercules); however, the crimp path changes based on the pattern of the TBC. The details of a helix curve and crimp paths for different patterns are presented in the appendix of the author's recent publication [24]. Each TBC consists of two sets of yarns, one clockwise and one counter-clockwise. The equations of clockwise and counter-clockwise yarn paths are shown in Equation 5-1 and Equation 5-2.

$$X_{ccw} = R\cos\varphi + X0$$
$$Y_{ccw} = R\sin\varphi + Y0$$
$$Z_{ccw} = R\,\varphi\cot\theta + Z0$$

Equation 5-1

$$X_{cw} = R\cos\varphi + X0$$
$$Y_{cw} = -R\sin\varphi + Y0$$
$$Z_{cw} = R\varphi\cot\theta + Z0$$

Equation 5-2

where X_{ccw}, Y_{ccw}, and Z_{ccw} are coordination of counter-clockwise yarn paths, and X_{cw}, Y_{cw}, and Z_{cw} are coordination of clockwise yarn paths. R is the radius of the helix, φ is the winding angle, and θ is the helix angle (braid angle). $X0$, $Y0$, and $Z0$ are offset of the mandrel's centre in X, Y and Z directions, respectively.

A sample clockwise and a counter-clockwise helix path are shown in Figure 5-2. In these samples, the $0 < \varphi < 2\frac{3}{4}$, R = 10mm, $\theta = 45°$, X0 = 4mm, Y0 = 3mm, and Z0 = 5mm.

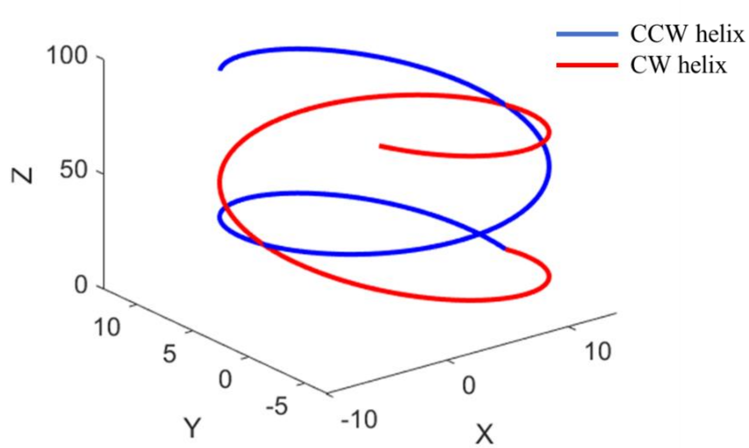

Figure 5-2 One clockwise (red) and one counter-clockwise (blue) sample Helix curve.

One important feature to consider in designing the geometrical model is the correct direction of the ridges. As discussed in [8], the correct direction of the ridges should be parallel to the axis of the TBC. However, in some of the publications [6], [7], the direction of the axis is assumed to be perpendicular to the axis. Therefore, to generate the corrected Regular pattern's path, two types of yarns in each direction (clockwise and counter-clockwise) need to be defined, which are shown in Equation 5-3 – Equation 5-6. The perpendicular and parallel axis of the ridges are shown in Figure 5-3.

$$\begin{aligned} X_{cw1i} &= \left(R + S_{cw1}(\varphi)\right)\cos(\varphi + (i-1)\times 2\omega) + X_0 && i = 1,2 \ldots n/2 \\ Y_{cw1i} &= \left(R + S_{cw1}(\varphi)\right)\sin(\varphi + (i-1)\times 2\omega) + Y_0 && i = 1,2 \ldots n/2 \\ Z_{cw1i} &= R\varphi\cot\theta + Z_0 && i = 1,2 \ldots n/2 \end{aligned} \qquad \text{Equation 5-3}$$

$$\begin{aligned} X_{cw2i} &= \left(R + S_{cw2}(\varphi)\right)\cos(\varphi + (2i-1)\times \omega) + X_0 && i = 1,2 \ldots n/2 \\ Y_{cw2i} &= \left(R + S_{cw2}(\varphi)\right)\sin(\varphi + (2i-1)\times \omega) + Y_0 && i = 1,2 \ldots n/2 \\ Z_{cw2i} &= R\varphi\cot\theta + Z_0 && i = 1,2 \ldots n/2 \end{aligned} \qquad \text{Equation 5-4}$$

$$\begin{aligned} X_{ccw1i} &= \left(R + S_{ccw1}(\varphi)\right)\cos(\varphi + (i-1)\times 2\omega) + X_0 && i = 1,2 \ldots n/2 \\ Y_{ccw1i} &= -\left(R + S_{ccw1}(\varphi)\right)\sin(\varphi + (i-1)\times 2\omega) + Y_0 && i = 1,2 \ldots n/2 \\ Z_{ccw1i} &= R\varphi\cot\theta + Z_0 && i = 1,2 \ldots n/2 \end{aligned} \qquad \text{Equation 5-5}$$

$$\begin{aligned} X_{ccw2i} &= \left(R + S_{ccw2}(\varphi)\right)\cos(\varphi + (2i-1)\times \omega) + X_0 && i = 1,2 \ldots n/2 \\ Y_{ccw2i} &= -\left(R + S_{ccw2}(\varphi)\right)\sin(\varphi + (2i-1)\times \omega) + Y_0 && i = 1,2 \ldots n/2 \\ Z_{ccw2i} &= R\varphi\cot\theta + Z_0 && i = 1,2 \ldots n/2 \end{aligned} \qquad \text{Equation 5-6}$$

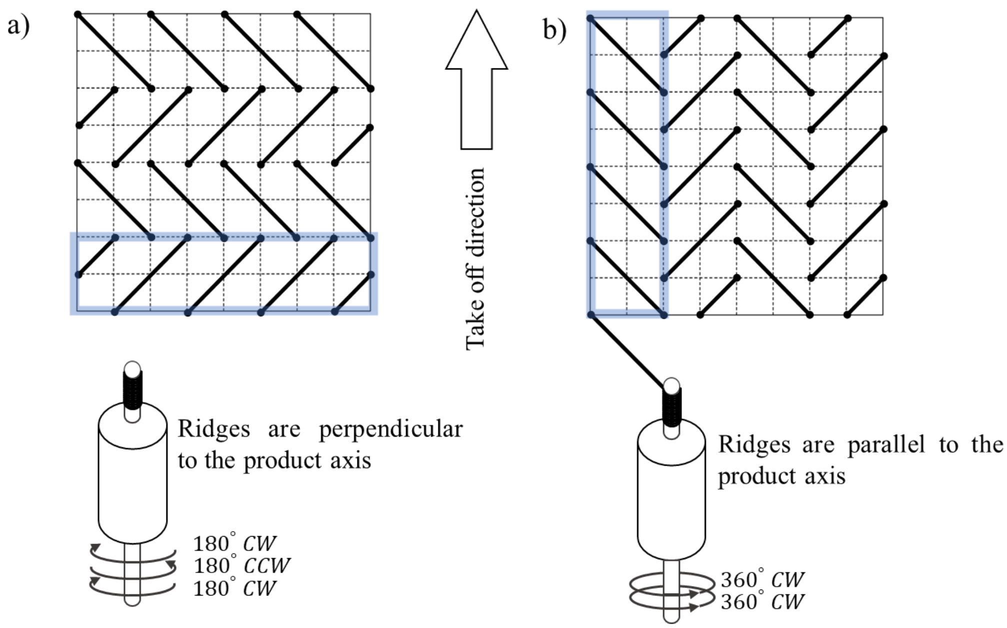

Figure 5-3 The ridges' direction compared to the TBC's axis. a) the ridges perpendicular to the TBC's axis, b) the ridges parallel to the TBC's axis [8]

where $S(\varphi)$ is the crimp path, n is the number of yarns moving in one direction, and N is the total number of yarns in the TBC (i.e. $n = N/2$), i is a counter between 1 to $n/2$, ω is the shift angle which is calculated as the angle between every two strands (i.e., ω =2π/n). The two differences between X_1, Y_1, Z_1 and X_2, Y_2, Z_2 are the value of $S(\varphi)$ and the initial angle, defined by a portion of the ω. There would be four $S(\varphi)$ equations. Two for clockwise and two for counter-clockwise. The difference between $S_1(\varphi)$ and $S_2(\varphi)$ is the order of parametric equations, which makes them half a period apart. While the $S_1(\varphi)$ starts from its minimum value, the $S_2(\varphi)$ starts from its maximum. This half-period shift will make the ridges of the TBC parallel to the axis. The clockwise and counter-clockwise equations for $S_1(\varphi)$ and $S_2(\varphi)$ are shown in Equation 5-7 to Equation 5-10.

$$S_{cw1}(\varphi_j) = \begin{array}{ll} -r & ; 0 \le \varphi_j < \theta/2 \\ r\sin\left(\frac{N\varphi_j}{2} + \frac{\pi}{2}\right) & ; \theta/2 \le \varphi_j < \theta \\ r & ; \theta \le \varphi_j < 3\theta/2 \\ -r\sin\left(\frac{N\varphi_j}{2} + \frac{\pi}{2}\right) & ; 3\theta/2 \le \varphi_j < 2\theta \end{array} \quad \text{Equation 5-7}$$

$$S_{cw2}(\varphi_j) = \begin{cases} r & ; 0 \le \varphi_j < \theta/2 \\ -r\sin\left(\frac{N\varphi_j}{2} + \frac{\pi}{2}\right) & ; \theta/2 \le \varphi_j < \theta \\ -r & ; \theta \le \varphi_j < 3\theta/2 \\ r\sin\left(\frac{N\varphi_j}{2} + \frac{\pi}{2}\right) & ; 3\theta/2 \le \varphi_j < 2\theta \end{cases}$$ Equation 5-8

$$S_{ccw1}(\varphi_j) = \begin{cases} r\sin\left(\frac{N\varphi_j}{2} + \frac{\pi}{2}\right) & ; 0 \le \varphi_j < \theta/2 \\ -r & ; \theta/2 \le \varphi_j < \theta \\ -r\sin\left(\frac{N\varphi_j}{2} + \frac{\pi}{2}\right) & ; \theta \le \varphi_j < 3\theta/2 \\ r & ; 3\theta/2 \le \varphi_j < 2\theta \end{cases}$$ Equation 5-9

$$S_{ccw2}(\varphi_j) = \begin{cases} -r\sin\left(\frac{N\varphi_j}{2} + \frac{\pi}{2}\right) & ; 0 \le \varphi_j < \theta/2 \\ r & ; \theta/2 \le \varphi_j < \theta \\ r\sin\left(\frac{N\varphi_j}{2} + \frac{\pi}{2}\right) & ; \theta \le \varphi_j < 3\theta/2 \\ -r & ; 3\theta/2 \le \varphi_j < 2\theta \end{cases}$$ Equation 5-10

All the equations represented above are incorporated into a program in MATLAB (R2022b The MathWorks Inc, Natick, Ma, USA) software package named TBC-Gen. This program can generate the yarn path for all three patterns: Diamond, Regular, and Hercules [25].

Two Regular TBCs with similar input parameters are created and shown in Figure 5-4, where the counter-clockwise yarns are coloured red, and the clockwise yarns are blue. Figure 5-4 a) illustrates the geometrical model with ridges perpendicular to the axis. As shown in Figure 5-4 a), all the counter-clockwise yarns are located inside, and all the clockwise yarns are outside. However, Figure 5-4 b) shows the result of the TBC-Gen in which a Regular TBC with similar geometrical variables as the TBC shown in Figure 5-4 a) is generated. In this figure, the direction of the ridge is parallel to the axis. Therefore, the clockwise and counter-clockwise yarns in the cross-section images change their inner and outer positions, respectively.

A carbon-fiber Regular TBC with 52 yarns, 45degrees braid angle, and 1.52 mm yarn width is scanned by mu cap C cap T, and the generated cross-section image is shown in Figure 5-4 c). In this actual model generated based on μCT, the location of clockwise and counter-clockwise change in and out, respectively. This pattern is similar to the pattern seen in Figure 5-4 b) generated by TBC-Gen, in which the direction of the ridge is parallel to the mandrel.

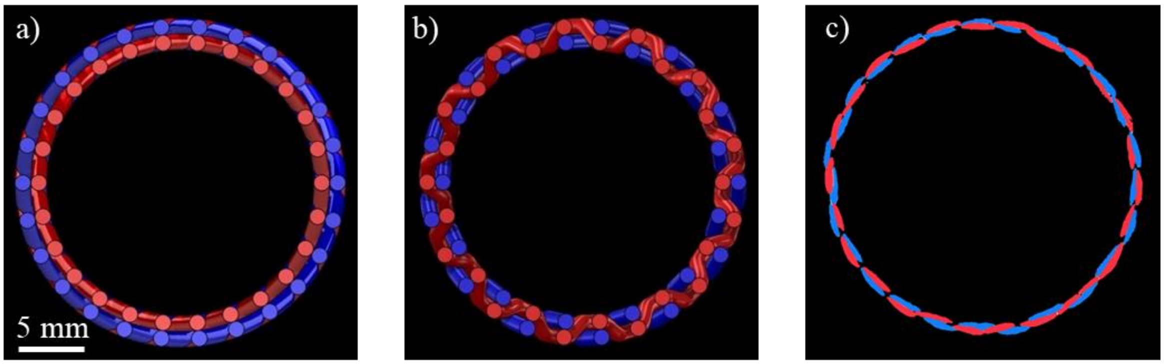

Figure 5-4 Regular TBCs cross-section (red: counter-clockwise, blue: clockwise) a) geometrical model where ridges direction is perpendicular to the axis of the mandrel, b)geometrical model created by TBC-Gen where ridges direction is parallel to the mandrel axis, and c) The cross-section of a μCT Regular TBC with 52 yarns, $45°$ braid angle, 1.52 mm yarn diam

5.2.2 Micro-Computerized Tomography (μCT)

μCT is a non-destructive testing method that can generate high-resolution 3-D models. The fundamentals of μCT are like clinical CT used for body analysis[26]. However, the size of the samples is smaller, and their resolution is in the range of 20-50 μm. Because of the high resolution of the obtained images, the detailed behaviour of the sample can be captured. Therefore, one of the advantages of μCT is taking dynamic images from samples under thermal or mechanical forces [27].

In μCT tests, the sample is placed between the X-ray source and the X-ray detector [28]. As a result, the sample will attenuate part of the X-ray sent to the detector. The X-ray's attenuation depends on the sample's density and thickness. In other words, the denser the sample, the more X-ray attenuation. Therefore, fewer X-rays will pass to the detector, making the relevant section of the recorded image darker. In the μCT test, the sample holder can turn with a predefined step size and be moved vertically to scan different sample sections. The images are then imported into an image processing software to create the cross-sectional images alongside a 3-D model of the scanned sample. The schematic of the μCT test is shown in Figure 5-5.

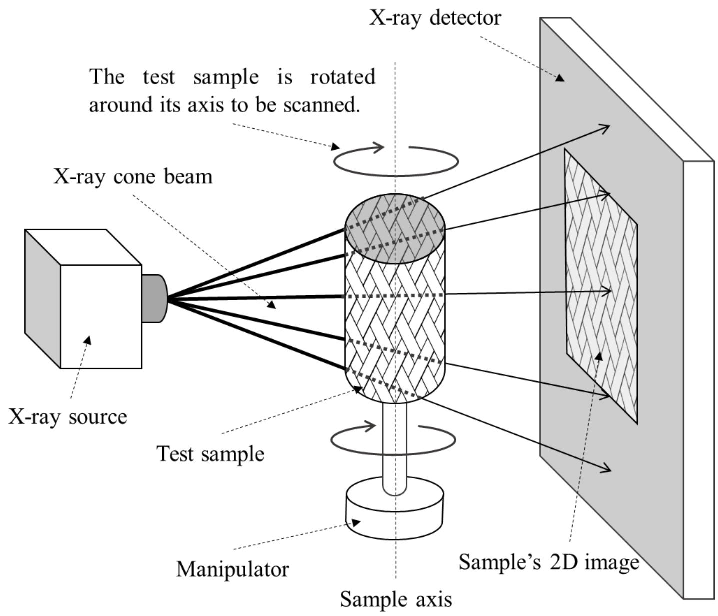

Figure 5-5 The fundamental schematic of the micro-CT test used for scanning the tubular braided composite [26]

This study scans the TBC samples using a desktop µCT scanner (SkyScan 1272, Bruker-MicroCT, Kontich, Belgium). The quality of the obtained images depends on the voltage, current and other variables used for testing the sample [29]. These parameters vary from sample to sample and are selected according to the settings, providing the best contrast between the different internal sections of the sample. The quality of the images can be increased by using other image processing techniques. However, the best practice for improving the quality of the final result is selecting the optimum parameters for that specific setting. The optimal parameters for scanning a closed-mesh Carbon fiber TBC with 52 yarns, 1 inch (25.4 mm) mandrel diameter, and 45degrees braid angle are tabulated in Table 5-1.

Table 5-1 The μCT setting of the open mesh TBC

μCT parameters	**Value (closed-mesh TBC)**
Image pixel size	10.88 μm
Source Voltage	55 kV
Source Current	166 μA
Number of scanned Images	1541
Exposure	1876 ms
Rotation step	0.1°
Rotation angle	180°
Frame Averaging	4
Duration	4 hours and 35 minutes

An example original μCT image of a TBC sample is shown in Figure 5-6 a). These images are imported into NRECON software (NRECON 1.7.1.0, Bruker, Belgium) to reconstruct the cross-sectional images similar to Figure 5-6 b). The cross-section image shown in Figure 5-6 b) includes noises that can be filtered using ImageJ software (National Institutes of Health, USA). Also, by binarizing these images, the analysis of them would be more straightforward. The threshold setting was used to obtain braid yarn cross-sections, and the used limit was between 38 and 87. The MATLAB software package was used to create the histogram curve and select the limits for the best presentation. The obtained histogram curve and the selected limit are shown in Figure 5-7. Despeckle techniques are also used to remove some of the noise. The final cross-sectional image is shown in Figure 5-6 c). The 3D model of the scanned TBC is also shown in Figure 5-6 d), and it is created using CTAn software (Bruker- MicroCT, Kontich, Belgium).

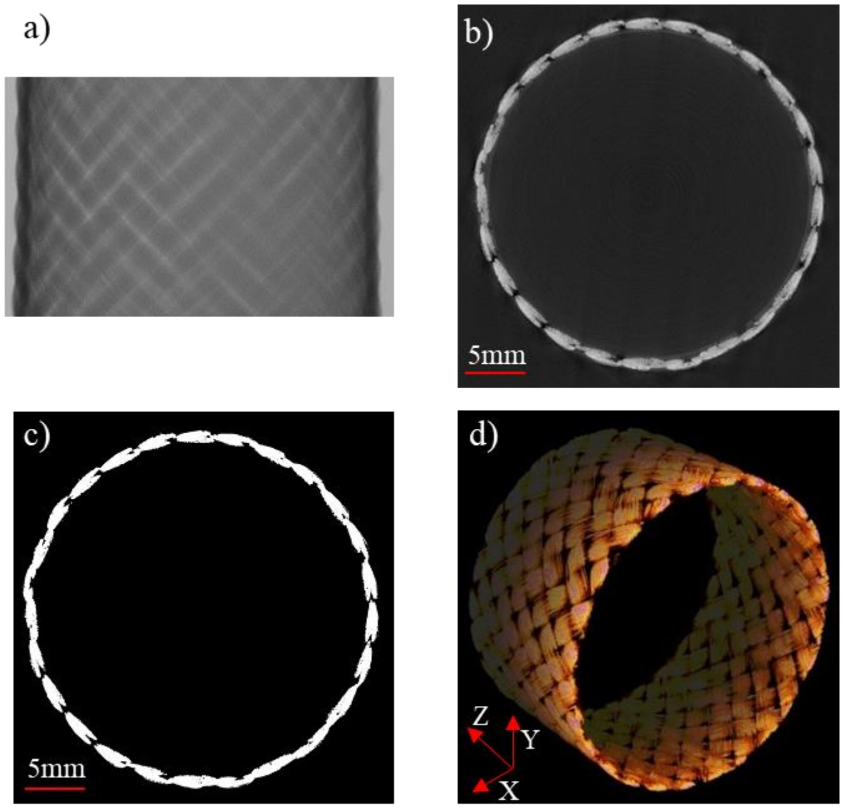

Figure 5-6 The scanned carbon-fiber TBC by µCT a) the original obtained μCT image from the tested TBC, b) the binarized cross-section of μCT scan, c) the original cross-section of μCT scan, and d) the 3D model generated using μCT images

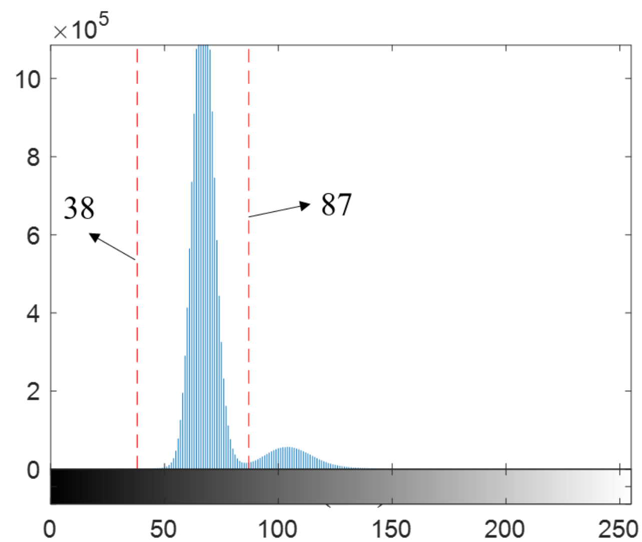

Figure 5-7 The histogram curve of the scanned cross-sectional image and the selected threshold

After applying the image processing techniques to the raw images from the µCT scan, they can be imported into the MATLAB software package to apply more image processing techniques.

However, because the cross-section of yarns intervenes, it would be difficult for the algorithm to segment all the yarns automatically. Due to these challenges, two yarns of the TBC have been extracted manually and inputted into the MATLAB software package. Figure 5-8 a) shows the inputted image. MATLAB's "bwboundaries" function can detect the boundary, centre, area, major and minor diameters, and the orientation of the boundary alongside other features of the detected boundary. The detected boundary and its centre point are shown in Figure 5-8 b). The algorithm fits an ellipse into the boundary; based on this, it reports the features. Figure 5-8 c) shows the fitted ellipse and the reported major and minor diameters.

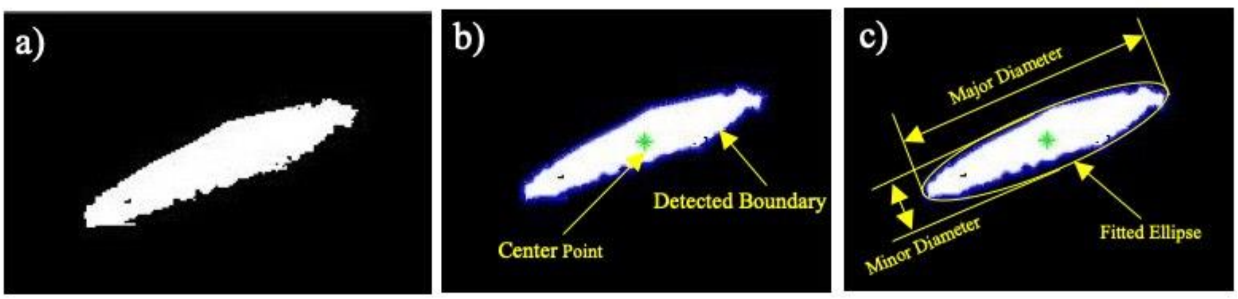

Figure 5-8 The yarn cross-section of the µCT scanned TBC a) segmented single yarn, b) segmented single yarn and detected boundary and centroid, and c) the fitted ellipse and minor and major diameters.

These features of the boundaries will make the quantitative analysis of µCT possible. Collecting all of the centre points of the yarn cross-sections will generate the yarn path of the specific yarn. In the next section, the extracted centre points are plotted and compared against the existing geometrical to evaluate the accuracy of the geometrical models proposed for modelling the TBC yarn path. Also, the measured area of yarns can be used to estimate the average yarn area. Finally, the yarn cross-section can be used to calculate the equivalent diameter for the geometrical model to generate the same cross-section area.

5.2.3 Inverse problem

5.2.3.1 Fundamental of Inverse Problem

An inverse problem can be designed to fit a geometrical model into the μCT model. An objective function needs to be developed to solve an inverse problem. The objective function is the mean square error between the geometrical model and the experimental results (the μCT results). The objective function for the problem discussed in this paper is shown in Equation 5-11.

$$\sigma = \arg(\sigma)\, min\left\|P_{g(\sigma)} - P_{\mu CT}\right\|^2 \quad \text{Equation 5-11}$$

where σ is the parameter vector of the geometrical model, $P_{g(\sigma)}$ is the yarn path of the geometrical model that fits the experimental results, and $P_{\mu CT}$ is the experimental yarn path obtained from the μCT scan. The parameter vector (σ), which minimizes this objective function, solves the inverse problem.

Different algorithms can be used for solving the inverse problem, and their selection of them depends on the nature of the inverse problem. This paper uses the PSO algorithm to fit the simulation yarn path.

5.2.3.2 Particle Swarm Optimization (PSO) Algorithm

Kennedy and Eberhart's Particle Swarm Optimization (PSO) [30] approach uses stochastic populations for optimization. It has effectively solved various issues, including pattern categorization, function optimization, and training artificial neural networks [31]. PSO is a heuristic global optimization technique and a swarm intelligence-based optimization algorithm. In contrast to evolutionary algorithms, which use a selection stage where some elements are picked to continue to the next iteration while the others are dropped, PSO does not employ selection. Instead, all population members remain alive from the start of a trial until the finish. In PSO, the best particle from the previous generation always replaces the poorest particle of the prior generation. Accordingly, when the algorithm develops, better outcomes are obtained. Its key benefits are the simplicity of this algorithm's implementation and the requirement for only a small number of starting particles. The flowchart of the PSO algorithm is shown in Figure 5-9.

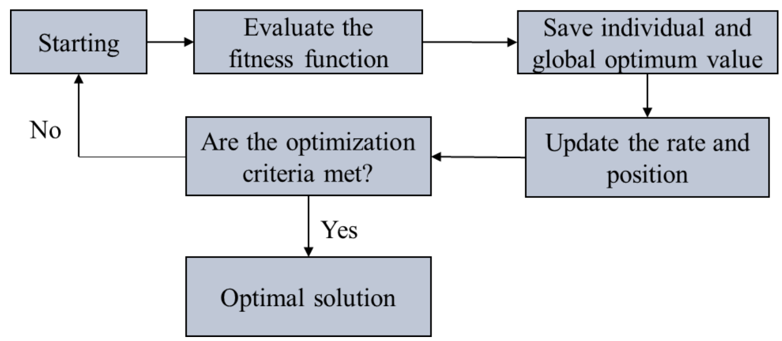

Figure 5-9 The workflow of the PSO algorithm

In PSO, every particle is defined by its current position and speed alongside the most optimal position of each individual and the most optimal position of the surroundings. The speed and position of particles change based on Equation 5-12:

$$v_i^{k+1} = v_i^k + C_1 r_1^k(\mathbf{pbest}_i^k - X_i^k) + C_2 r_2^k(\mathbf{gbest}^k - X_i^k)$$
$$X_i^{k+1} = X_i^k + v_i^{k+1}$$
Equation 5-12

where v_i^k and X_i^k are d-dimensional speed and position of the particle i at its kth iteration and, $pbest_i^k$ and $gbest^k$ designate the most optimal position of the particle i and the most optimal position of the swarm, respectively. C_1 and C_2 control the speed of the flying particle and are usually set to 2, and r_1 and r_2 are random numbers between 0 and 1.

5.2.4 The Flowchart of This Research

This inverse problem will help analyze the efficiency of the geometrical model quantitatively and better understand the accuracy of the geometrical model that might be used for simulation and

Finite Element Analysis of the TBC. The flow chart of the algorithms used in this paper is shown in Figure 5-10.

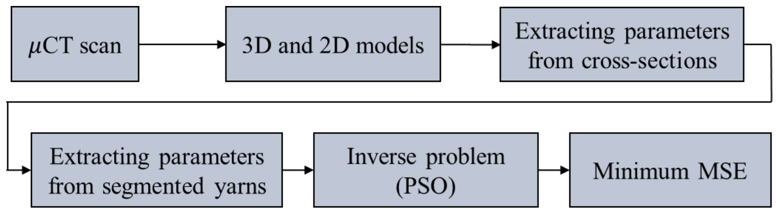

Figure 5-10 The flow chart of the used algorithm

5.3 Results and Discussion

5.3.1 Segmenting Yarns Out of μCT Scanned TBC

Two yarns in different positions are extracted manually from the scanned carbon fiber TBC (one clockwise and one counter-clockwise). The extracted yarns are created by identifying the cross-section of yarns through all of the cross-sections. The selected extracted yarns are shown and highlighted in Figure 5-11 with blue (counter-clockwise) and red (clockwise). After extracting these yarns manually, they are imported into MATLAB software for analysis to extract yarns' boundaries and other properties. One of the extracted parameters is the center points, which are connected and plotted in Figure 5-12. Figure 5-12 a) shows the 3D model of the extracted yarns, and Figure 5-12 b) shows the 2D (X-Y) view of the same yarns.

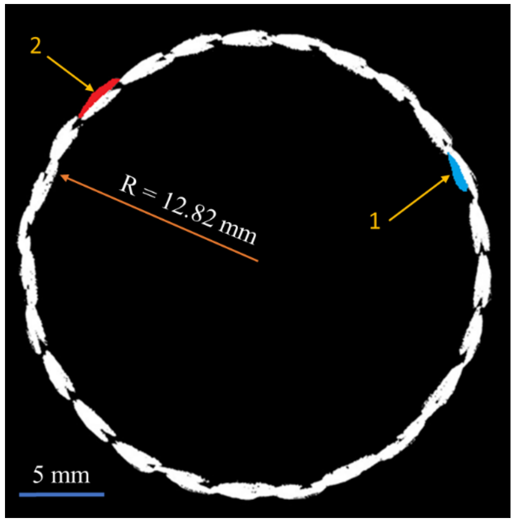

Figure 5-11 Cross-section of a Regular cured TBC with two annotated extracted yarns: 1) the counter-clockwise yarn and 2) the clockwise yarn

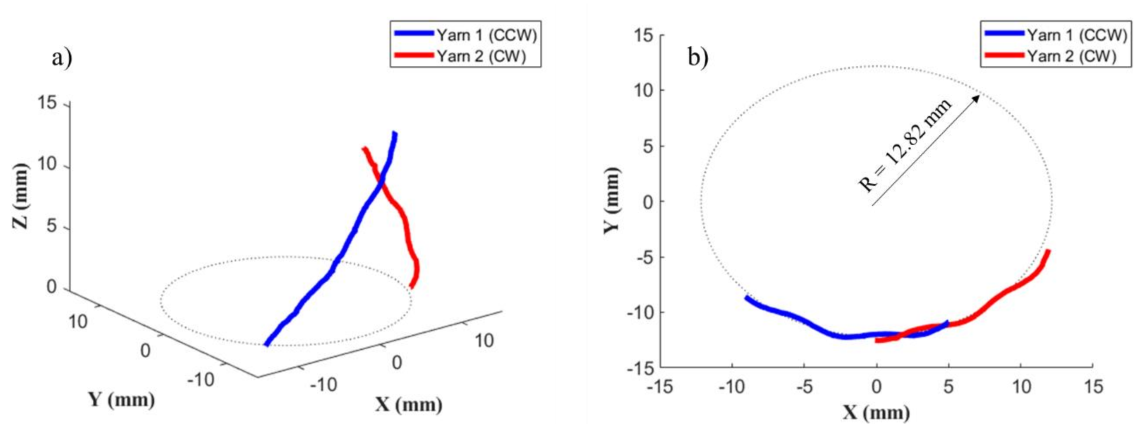

Figure 5-12 Two extracted yarn paths of the scanned TBC. Yarn 1 (counter-clockwise) and Yarn 2 (clockwise). a) yarns in 3D view, and b) in 2-d view (top view)

5.3.2 Extracting Parameters of Scanned TBC

Different algorithms extract the parameters of the scanned and segmented yarns. One of the most critical parameters is the diameter of the mandrel. The scanned image's cross-section is used to extract the mandrel diameter. The complete cross-section is shown in Figure 5-13 a). The threshold of the image has been modified to increase the contrast between the yarns and the background. The filled function fills the image regions and holes in the cross-section in the next step. Figure 5-13 b) shows the result of the filled function. Next, the 'Edge' image algorithm detects the yarns' overall boundaries and skips the yarns' inner side. The result of the 'Edge' image algorithm is shown in Figure 5-13 c). Finally, a circle with the minimum possible diameter is fitted to the data of the proceed image, and the diameter of the fitted image is reported. The final fitted circle to the cross-section image is shown in Figure 5-13 d). This process is repeated for the other 14 cross-sections. The distance between every two cross-sections was 2.5 mm. Four of the fitted circles in the cross-section images are shown in Figure 5-13 f) - h). The 3D model of the extracted yarn and the location of the sample cross-sections are also shown in Figure 5-14. The average diameter of the mandrel measured out of 14 images, and the relevant standard deviations are 25.63 ± 0.066 mm.

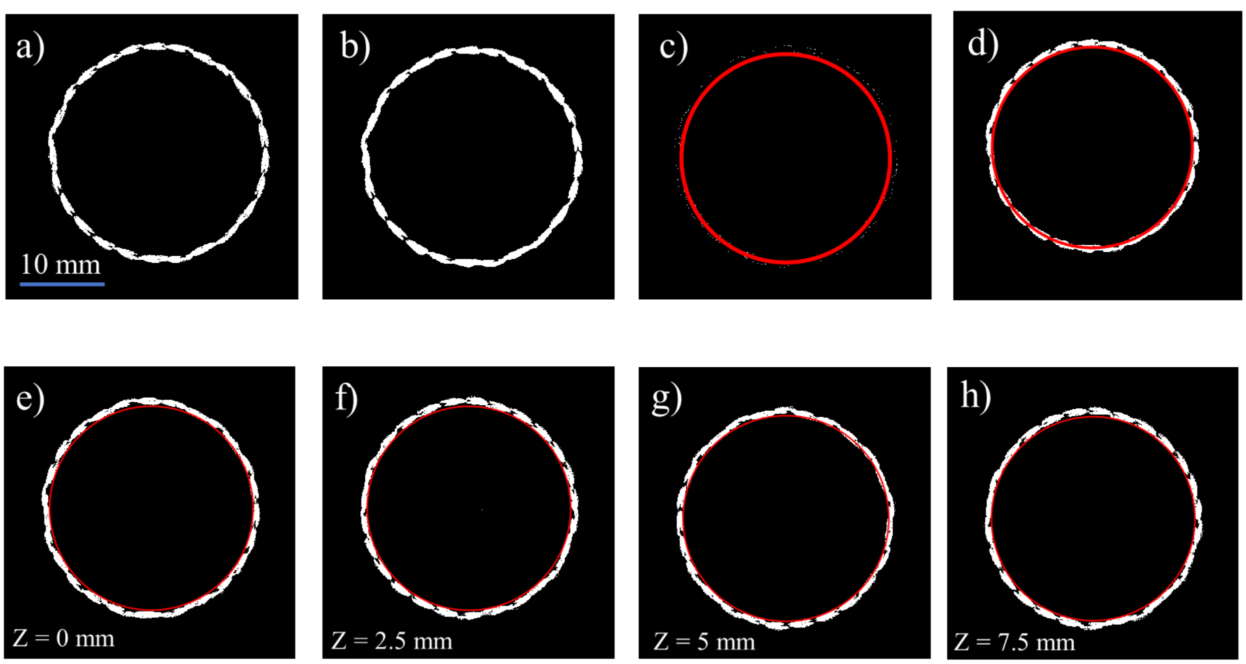

Figure 5-13 Extracting the mandrel's diameter. a) the threshold cross-section, b) the filled cross-section image, c) the 'Edge' cross-section image, d) the fitted circle to the cross-section image of the TBC, e) the fitted circle to the cross-section at Z=0, f) the fitter circle to the cross-section at Z=2.5 mm, g) the fitter circle to the cross-section at Z =5 mm, h) the fitter circle to the cross-section at Z=7.5 mm

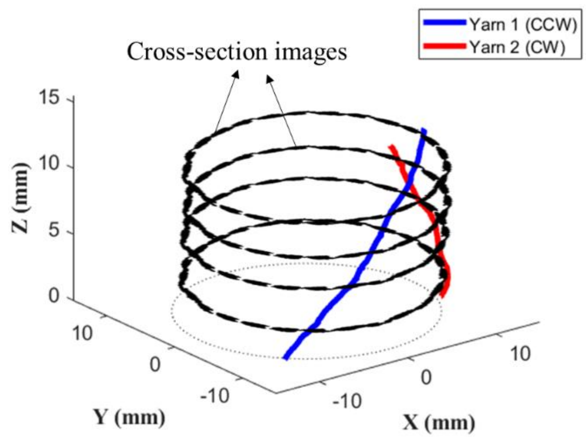

Figure 5-14 Four sample cross-sections of the scanned TBC.

The minimum diameter of the segmented yarns can be extracted using the algorithm shown in Figure 5-8. All cross-section images of the single yarn were scanned and measured. The average minimum diameter of the ellipse covering the extracted yarn was 0.42 mm, and the variation was 0.0013. The number of yarns was 52. The braid angle was extracted by measuring the line angle connecting the yarn path's first and last points with the axis of the TBC. The braid angle of the segmented yarn 1 was 47.64°, which is shown in Figure 5-15 a). The portion angle (the angle between the start and end point of the yarn in the top view) of the segmented yarn one is measured in the X-Y view and shown in Figure 5-15 b). The braid angle of yarn 2 was 52.11°, as shown in Figure 5-15 c). Finally, the portion angle of yarn 2 was 70.38°, shown in Figure 5-15 d). There is around a 10% difference in the braid angle of yarn 1 and yarn 2. One reason for that is the flexible nature of the TBC and the fact that usually, the yarns are not in their ideal shape, and they change slightly. Also, the locations of yarn 1 and yarn 2 in the TBC are different when measured from a fixed plane (X-Z plane). Therefore, it adds another source of error to the measurement.

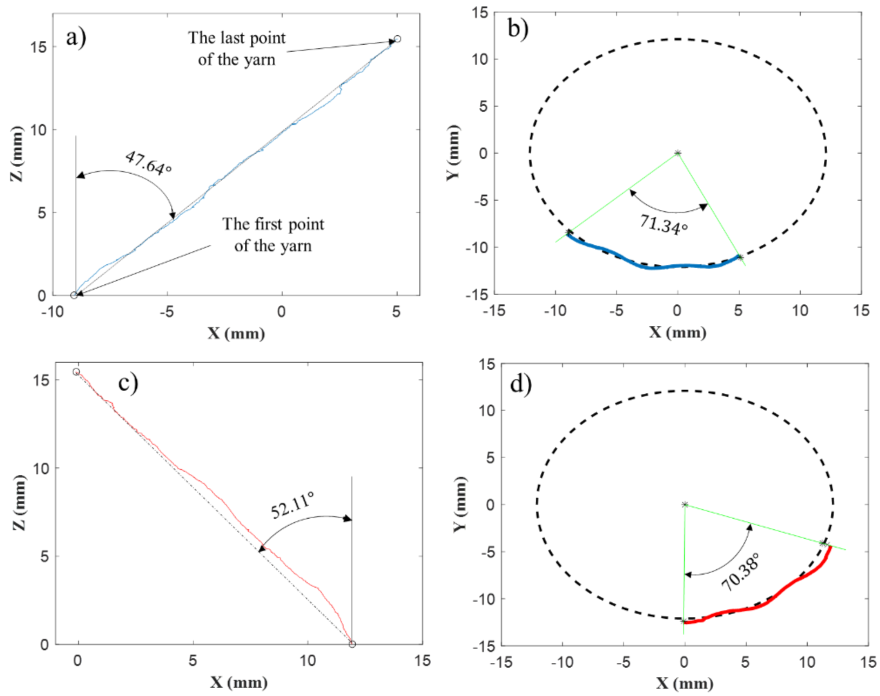

Figure 5-15 a) Measuring the braid angle of yarn 1, b) measuring the portion angle of yarn 1, c) Measuring the braid angle of yarn 2, d) measuring the portion angle of yarn 2

Having these extracted parameters and considering the regular pattern of the TBC, one can design the geometrical model of the yarn using the TBC-Gen program. The designed and segmented yarns are overlayed and shown in Figure 5-16. In Figure 5-16 a), the designed yarn is for a complete 360° yarn path, and it has not been cut for the angle portion. Two green lines were drawn from the center of the mandrel to the beginning and the end of the µCT yarn path. Then, the geometrical yarn was burned from its intersection by the green lines. The section of the geometrical yarn between the lines is kept, and the rest of the yarn path is removed. The result of the removed section is shown in Figure 5-16 b). As shown in Figure 5-16 b), the designed geometrical model does not fit the µCT yarn path well. The MSE between the two models is 14.47%. The MSE value alongside the yarn is calculated at each point using Equation 5-13:

$$MSE_{point} = (Y_{simulation} - Y_{\mu CT})^2 \quad \text{Equation 5-13}$$

The MSE_{point} values are plotted in Figure 5-16 c). Considering the shape of the yarns in Figure 5-16 b) and the wave shape of the MSE in Figure 5-16 c), it is seen that there is a phase difference between the geometrical and µCT models. When the µCT model is in the highest period, the geometrical model is in the lowest. The geometrical model is rotated around the mandrel center ([0 0]) to solve this problem. A new parameter as rotation parameter (β) is defined in the algorithm to define the degree of rotation for the geometrical model.

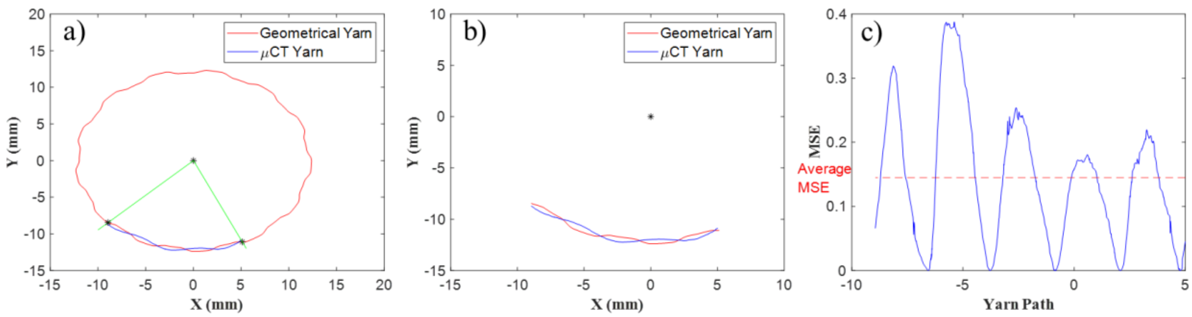

Figure 5-16 The geometrically designed yarn path and the micro-CT yarn path. a) complete geometrical model (red) and µCT yarn 1(blue), b) sectioned geometrical model according to the portion angle (red) and the µCT yarn 1 (blue), c) the value of the MSE alongside the yarn path

Particle Swarm Optimization (PSO) is used for optimizing the β. An objective function between the geometrical model and the µCT model was created to perform this analysis, and it is shown in Equation 5-14.

$$\beta = \arg(\beta)\, min\|S_\beta - S_{\mu CT}\|^2 \quad \text{Equation 5-14}$$

where $S_{\mu CT}$ is the µCT model and S_β is the geometrical model, including the rotation parameter β that minimizes Equation (14) reveals the best fit between the two models. This objective function is incorporated into the PSO algorithm. After running the optimization algorithms, the $\beta = 16.58°$, shows the minimum MSE between two yarn paths ($MSE_{min} = 0.86\%$). The resulting yarn paths are shown in Figure 5-17. Figure 5-17 a) shows the complete geometrical model with $\beta = 16.58°$ and the µCT yarn paths. Figure 5-17 b) shows the segmented rotated geometrical model and the µCT yarn. Figure 5-17 c) shows the MSE between two yarn paths.

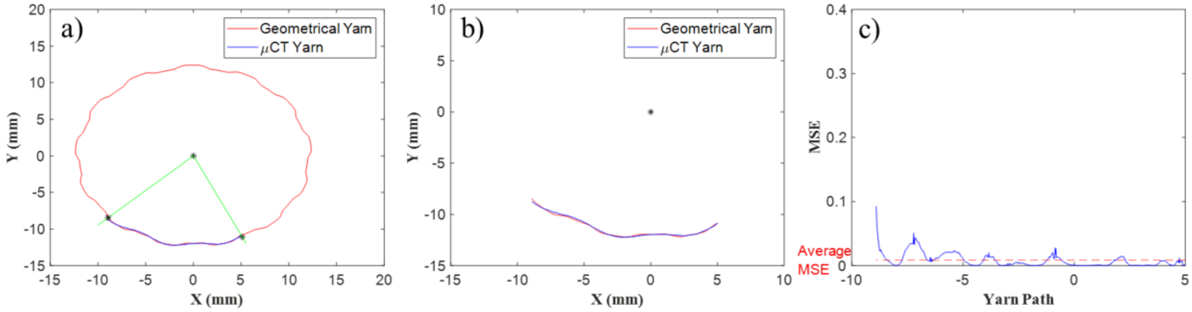

Figure 5-17 Fitted geometrical model to the µCT yarn 1 by optimizing the β parameter. a) complete geometrical model with optimized β parameter (red) and µCT yarn 1(blue), b) sectioned geometrical model according to the portion angle and optimized β parameter (red) and the µCT yarn 1 (blue), c) the value of the MSE between the geometrical model with optimized β parameter and the µCT yarn 1.

5.3.3 Discussion

By introducing the rotation angle parameter (β) and optimizing it, the MSE between the simulation yarn path and the µCT yarn path was about 17 times less than the MSE between the simulation yarn path without β and the µCT yarn path. This significant reduction in MSE is shown in Figure 5-18 where both MSE curves are plotted together. β increased the likelihood of the simulation model with the µCT model and provided a better fit.

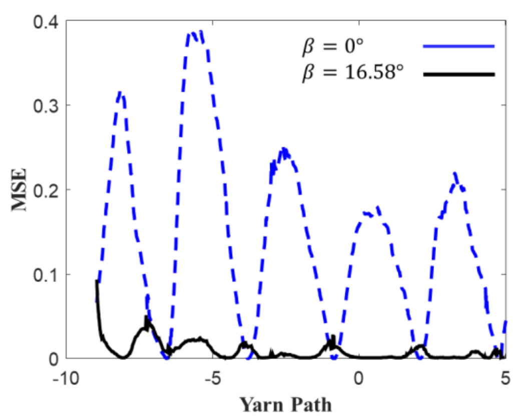

Figure 5-18 Comparing the MSE curve of the yarn path with $\beta = 0°$ (the blue dashed curve) and the yarn path with $\beta = 16.58°$ (the black solid curve)

This study evaluated the accuracy of the TBC geometrical model. However, this method can evaluate other composite materials such as textiles and 3D. Since textile composite materials yarns do not have tubular shape curvature, their analysis is expected to be less complicated. Also, the segmentation method could be improved by automating the process. The main challenge with segmentation is recognizing the yarn cross-sections because they usually interfere with each other. This interference is mainly because the yarns are under pressure in manufacturing. One solution for solving this issue is changing the material of one of the yarns. For example, some copper yarns can be used in carbon fiber composite material. In this case, the carbon fiber yarns can be removed by changing the threshold of the µCT images, and only cupper yarns will remain, and they can be analyzed automatically.

Another method for automating the segmentation process is developing an Artificial Intelligent method for recognizing the yarns. Automating the segmentation process without changing the manufacturing process will expedite the analysis steps and help evaluate all of the yarns of the TBC.

In this paper, only the 2D Regular pattern TBC was examined. Other patterns can be scanned and analyzed too. Also, a significant study has been done in the µCT scan of 3D braided composites [32]–[34]. The geometrical model of the 3D models can be fitted into these models too. Therefore, the accuracy of those models can be studied too.

5.4 Conclusion

This paper presents the algorithm for generating a geometrical model for Regular TBC with ridges parallel to the axis. The presented model can move in X, Y, and Z directions, making it more versatile than other existing models. Furthermore, the algorithms were incorporated into a computerized program called TBC-Gen, enabling users to generate the path of the yarn without deep knowledge of braiding model algorithms.

A μCT scan of a cured Carbon fiber TBC was performed, and two yarns were extracted manually. Different image processing algorithms were applied to extract the properties of the extracted yarns. A geometrical model was generated and compared with the μCT model using the extracted properties. To improve the fitness of the geometrical and μCT model, a rotation angle (β) was introduced to the algorithm, and the PSO algorithm was used to optimize the value of β. After introducing the β parameter and optimizing it, the MSE between the geometrical model and the μCT models was reduced to 0.86%.

The minor error (less than 1%) between the geometrical and μCT models shows that the developed geometrical model can provide acceptable results for simulating TBCs. A more accurate geometrical model will help to use this model for other analyses like FEM more confidently. This study shows a quantitative comparison between a TBC geometrical model and a μCT model. This quantitative comparison will help the researchers better evaluate the geometrical model's accuracy. A simulation model based on both geometrical and μCT models needs to be done to study the error of the geometrical model more thoroughly, and the output results need to be compared.

5.5 Acknowledgments

The authors would like to acknowledge the funding support of the Natural Sciences and Engineering Research Council of Canada (NSERC) RGPIN- 2018-05899.

5.6 References

[1] J. P. Carey, *Handbook of advances in braided composite materials: Theory, production, testing and applications*. Woodhead Publishing, 2016.

[2] A. Mendoza, R. Trullo, and Y. Wielhorski, “Descriptive modeling of textiles using FE simulations and deep learning,” *Compos Sci Technol*, vol. 213, p. 108897, Sep. 2021, doi: 10.1016/J.COMPSCITECH.2021.108897.

[3] A. Kaw, *Mechanics of Composite Materials, Second Edition*, vol. 29. CRC Press, 2005. doi: 10.1201/9781420058291.

[4] D. Carlstedt and L. E. Asp, “Performance analysis framework for structural battery composites in electric vehicles,” *Compos B Eng*, vol. 186, p. 107822, Apr. 2020, doi: 10.1016/J.COMPOSITESB.2020.107822.

[5] C. Ayranci and J. Carey, “2D braided composites: A review for stiffness critical applications,” *Compos Struct*, vol. 85, no. 1, pp. 43–58, Sep. 2008, doi: 10.1016/j.compstruct.2007.10.004.

[6] A. Rawal, S. Gupta, H. Saraswat, and A. Sibal, “Geometrical modeling of near-net shape braided preforms,” *Textile Research Journal*, vol. 85, no. 10, pp. 1055–1064, Jun. 2015, doi: 10.1177/0040517514559587.

[7] T. Alpyildiz, “3D geometrical modelling of tubular braids,” *Textile Research Journal*, vol. 82, no. 5, pp. 443–453, Mar. 2012, doi: 10.1177/0040517511427969.

[8] Y. Kyosev, “Generalized geometric modeling of tubular and flat braided structures with arbitrary floating length and multiple filaments,” *Textile Research Journal*, vol. 86, no. 12, pp. 1270–1279, Jul. 2016, doi: 10.1177/0040517515609261.

[9] F. Ning, P. Potluri, W. Yu, and J. Hearle, “Geometrical modeling of tubular braided structures using generalized rose curve,” *Textile Research Journal*, vol. 87, no. 4, pp. 474–486, Mar. 2017, doi: 10.1177/0040517516632471.

[10] G. He *et al.*, “Mathematical and geometrical modeling of braided ropes bent over a sheave:,” *https://doi.org/10.1177/1558925020939726*, vol. 15, Jul. 2020, doi: 10.1177/1558925020939726.

[11] A. Gholami and G. W. Melenka, “Finite Element Analysis Of 2-D Tubular Braided Composite Based on Geometrical Models to Study Mechanical Performances,” *Mechanics of Advanced Materials and Structures*, 2021.

[12] G. W. Melenka, B. M. Bruni-Bossio, C. Ayranci, and J. P. Carey, “Examination of voids and geometry of bio-based braided composite structures,” *IOP Conf Ser Mater Sci Eng*, vol. 406, no. 1, p. 012012, Sep. 2018, doi: 10.1088/1757-899X/406/1/012012.

[13] G. W. Melenka and C. Ayranci, “Advanced measurement techniques for braided composite structures: A review of current and upcoming trends,” *J Compos Mater*, vol. 54, no. 25, pp. 3895–3917, Oct. 2020, doi: 10.1177/0021998320903105.

[14] L. Ge, H. Li, J. Zhong, C. Zhang, and D. Fang, “Micro-CT based trans-scale damage analysis of 3D braided composites with pore defects,” *Compos Sci Technol*, vol. 211, p. 108830, Jul. 2021, doi: 10.1016/J.COMPSCITECH.2021.108830.

[15] Y. Li, B. Sun, and B. Gu, “Impact shear damage characterizations of 3D braided composite with X-ray micro-computed tomography and numerical methodologies,” *Compos Struct*, vol. 176, pp. 43–54, Sep. 2017, doi: 10.1016/J.COMPSTRUCT.2017.04.067.

[16] L. Wu *et al.*, “Short Beam Shear Behavior and Failure Characterization of Hybrid 3D Braided Composites Structure with X-ray Micro-Computed Tomography,” *Polymers (Basel)*, vol. 12, no. 9, p. 1931, 2020.

[17] Y. Gu *et al.*, “Torsion damage mechanisms analysis of two-dimensional braided composite tubes with digital image correction and X-ray micro-computed tomography,” *Compos Struct*, vol. 256, p. 113020, Jan. 2021, doi: 10.1016/J.COMPSTRUCT.2020.113020.

[18] X. Liu *et al.*, “Refine reconstruction and verification of meso-scale modeling of three-dimensional five-directional braided composites from X-ray computed tomography data,” *Compos Struct*, vol. 245, p. 112347, Aug. 2020, doi: 10.1016/J.COMPSTRUCT.2020.112347.

[19] Z. Wu, S. Qin, P. Zhang, Z. Pan, X. Hu, and L. Shi, “Damage evolution in braided composite tubes under axial compression studied by combining infrared thermography and X-ray computed tomography,” *Compos Struct*, vol. 307, p. 116634, Mar. 2023, doi: 10.1016/J.COMPSTRUCT.2022.116634.

[20] J. H. Tam, Z. C. Ong, Z. Ismail, B. C. Ang, S. Y. Khoo, and W. L. Li, “Inverse identification of elastic properties of composite materials using hybrid GA-ACO-PSO algorithm,” *https://doi.org/10.1080/17415977.2017.1411911*, vol. 26, no. 10, pp. 1432–1463, Oct. 2017, doi: 10.1080/17415977.2017.1411911.

[21] J. Chen, Y. Tang, R. Ge, Q. An, and X. Guo, “Reliability design optimization of composite structures based on PSO together with FEA,” *Chinese Journal of Aeronautics*, vol. 26, no. 2, pp. 343–349, Apr. 2013, doi: 10.1016/J.CJA.2013.02.011.

[22] A. Gholami, F. Honarvar, and H. A. Moghaddam, “Modeling the ultrasonic testing echoes by a combination of particle swarm optimization and Levenberg–Marquardt algorithms,” *Meas Sci Technol*, vol. 28, no. 6, p. 65001, 2017.

[23] S. Prohaska, A. Hutanu, R. Kähler, and H. C. Hege, "Interactive exploration of large remote micro-CT scans," *IEEE Visualization 2004 - Proceedings, VIS 2004*, pp. 345–352, 2004, doi: 10.1109/VISUAL.2004.51.

[24] A. Gholami and G. W. Melenka, "Finite element analysis of 2-D tubular braided composite based on geometrical models to study mechanical performances," *https://doi.org/10.1080/15376494.2021.2001879*, pp. 1–17, Nov. 2021, doi: 10.1080/15376494.2021.2001879.

[25] Ali Gholami, "TBC-Gen Program," *github*, 2022. https://github.com/aligholamiYork/TBC-Gen (accessed Nov. 07, 2022).

[26] "Micro-computed Tomography (micro-CT) in Medicine and Engineering," *Micro-computed Tomography (micro-CT) in Medicine and Engineering*, 2020, doi: 10.1007/978-3-030-16641-0.

[27] J. Holmes, S. Sommacal, Z. Stachurski, R. Das, and P. Compston, "Digital image and volume correlation with X-ray micro-computed tomography for deformation and damage characterisation of woven fiber-reinforced composites," *Compos Struct*, vol. 279, p. 114775, Jan. 2022, doi: 10.1016/J.COMPSTRUCT.2021.114775.

[28] S. Y. Chung, J. S. Kim, D. Stephan, and T. S. Han, "Overview of the use of micro-computed tomography (micro-CT) to investigate the relation between the material characteristics and properties of cement-based materials," *Constr Build Mater*, vol. 229, p. 116843, Dec. 2019, doi: 10.1016/J.CONBUILDMAT.2019.116843.

[29] N. Kotwaliwale, K. Singh, A. Kalne, S. N. Jha, N. Seth, and A. Kar, "X-ray imaging methods for internal quality evaluation of agricultural produce," *J Food Sci Technol*, vol. 51, no. 1, p. 1, Jan. 2014, doi: 10.1007/S13197-011-0485-Y.

[30] J. Kennedy, R. E.-P. of ICNN'95-international, and undefined 1995, "Particle swarm optimization," *ieeexplore.ieee.org*, Accessed: Nov. 08, 2022. [Online]. Available: https://ieeexplore.ieee.org/abstract/document/488968/

[31] M. R. Bonyadi and Z. Michalewicz, "Particle Swarm Optimization for Single Objective Continuous Space Problems: A Review," *Evol Comput*, vol. 25, no. 1, pp. 1–54, Mar. 2017, doi: 10.1162/EVCO_R_00180.

[32] L. Xun, S. Huang, B. Sun, and B. Gu, "Torsional cracks development in carbon-fiber 3-D braided composite tubes," *Thin-Walled Structures*, vol. 184, p. 110477, Mar. 2023, doi: 10.1016/J.TWS.2022.110477.

[33] D. Shi, B. Zhang, C. Liu, L. Wang, X. Yang, and R. Luo, "In-situ study on compressive behaviors of different types of 3D SiC/SiC composites using X-ray computed tomography and digital image correlation," *Journal of Materials Research and Technology*, Jan. 2023, doi: 10.1016/J.JMRT.2022.12.178.

[34] G. Fang, C. Chen, S. Meng, and J. Liang, "Mechanical analysis of three-dimensional braided composites by using realistic voxel-based model with local mesh refinement," *J Compos Mater*, vol. 53, no. 4, pp. 475–487, Feb. 2019, doi: 10.1177/0021998318786541/ASSET/IMAGES/LARGE/10.1177_0021998318786541-FIG2.JPEG.

Chapter 6. Finite Element Analysis Of 2-D Tubular Braided Composite Based on Geometrical Models to Study Mechanical Performances

A version of this Chapter was published as:

Gholami, Ali, and Garrett W. Melenka. "Finite element analysis of 2-D tubular braided composite based on geometrical models to study mechanical performances." Mechanics of Advanced Materials and Structures 29.28 (2022): 7542-7558.

Abstract: Tubular Braided Composites (TBC) have a higher strength-to-weight ratio than conventional materials and better mechanical properties than laminated composite materials. The optimization of the TBC and the introduction of new applications requires a comprehensive understanding of TBC's behaviour. One efficient way to study the behaviour of TBC is using Finite Element Modelling (FEM). This paper will introduce a method for generating geometrical models with different patterns and variables. Micro-computed tomography (μCT) is also used to create an actual 3-D model of a TBC. The geometrical model and the μCT models are visually compared. The geometrical model is inputted into the FEM software package and is studied in different conditions. Finally, the result of FEM is compared against experimental and analytical results.

Keywords: composite material, tubular braided composite, open-mesh braided composite, finite element analysis, tensile test, micro-computed tomography, mechanical performances, geometrical model, periodic boundary condition, unit-cell model

6.1 Introduction

Composite materials contain two or more materials with different mechanical properties. The combination of these materials provides improved mechanical properties over the individual components [1]. Braided composites are a form of continuous fiber-based reinforced materials used in aerospace, automotive, petroleum, medical treatments, sporting, and marine applications [2-4]. For example, they can increase performance in hoses, pipes, or medical catheters [5]. Braided composites have significant advantages compared to conventional laminate composites. These advantages include out-of-plane stiffness, strength, toughness properties, net-shape fabrication, lower fabrication cost, and better impact and delamination resistance [6-7]. Because of these advantages, the number of studies investigating braided composites and their application is increasing significantly.

In two-dimensional braided composites, yarns are interlaced only in one plane and two directions (clockwise and counterclockwise). The preform can be manufactured in flat or Tubular Braided Composite (TBC) configurations. In addition, two-dimensional braided composites can be produced using a Maypole braider [8].

One way to categorize 2-D TBC is based on the pattern of yarns. Different patterns of braided composites are formed depending on the arrangement and movement of carriers. The patterns of the braided composites are Diamond (one tow passing above and then below the other tows, 1/1), Regular (two tows passing above and then below the other tows, 2/2), and Hercules (three tows passing above and then below the other tows, 3/3). Different patterns of braided composites are shown in Figure 6-1.

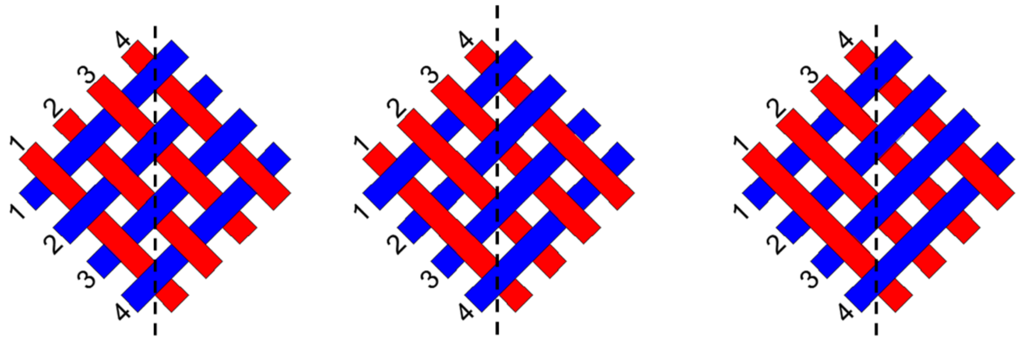

(a) (b) (c)

Figure 6-1 Different pattern of TBC's (a) Diamond (one by one), (b) Regular (two by two), and (c) Hercules (three by three),

The pattern shown in Figure 6-2 a) is known as the open-mesh Regular pattern, and Figure 6-2 b) shows a closed-mesh Regular pattern. There is a space between yarns in open-mesh TBC, while in the closed-mesh TBC, yarns contact each other. While closed-mesh TBCs are more frequently used in industry, open-mesh TBCs are used in the medical field as braided catheters and stents because the size of the stents should be as small as possible to prevent discomfort and provide easier manipulation [8,2,9]

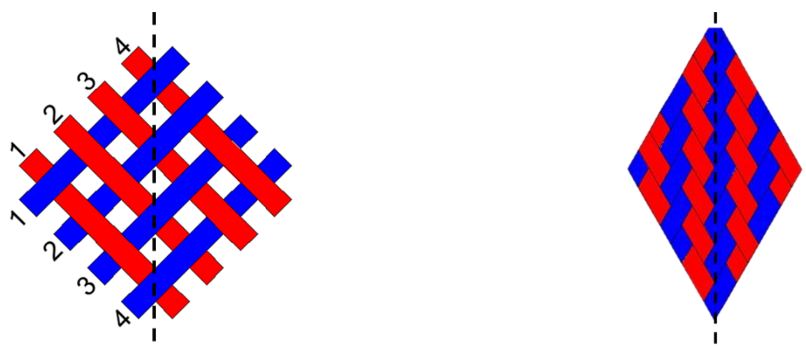

(a) (b)

Figure 6-2 A Regular patter of TBC a) open mesh, b) closed-mesh

Several studies have provided mathematical models for TBC. Liao and Adanur [10] developed an external and an internal 3-D circular braid model. They used a Frenet frame technique for sweeping the cross-section over the yarn path. Rawal and Potluri [11-12] developed an algorithm to produce 3-D braided preforms over different mandrel cross-sections: cylinder, square prism, cones with circular and elliptical cross-sections, and square pyramids. The yarn paths are modelled as straight lines, and undulations are ignored in their model. Gholami and Melenka [13] developed an algorithm for generating a yarn path and solid model for TBC. Alpyildiz [14] proposed a 3-D geometrical model for tubular braids. In this research, the braiding yarn's crimp is considered together with the tubular curvature of the tubular braided structure in the model. The provided model worked with different braid structures, braid angles, the number of yarns in a set, yarn, and mandrel diameter. Rawal et al. [15] developed geometrical models in cylindrical and conical mandrels with Diamond, Regular and triaxial forms. They simulated the model using the Virtual Reality Modelling Language (VRML). Finally, the geometrical models were verified by visually comparing them with camera images of actual models. One of the issues in the models developed [11], [12], [13], [14], [15] is that the orientation of the ridges in TBC is assumed to be perpendicular to the axis of the TBC. However, as explained in [16], manufacturing such a TBC is impossible with conventional braiding machines. Therefore, the models should be edited to produce TBCs with ridges orientation parallel to the TBC's axis.

In the papers introducing the geometrical model of TBC, the proposed models are not compared against physical braid samples to study the relevant error and the effect of the existing assumptions. Ning et al. [17] provided a geometrical model for TBC using the generalized rose curve. They generated their model in different mandrel shapes and compared their cylindrical geometrical model with an actual cylindrical TBC by comparing their images taken by a camera. However, the actual TBC they were comparing their result with were a closed-mesh TBC, and they did not compare their results with an open-mesh TBC.

Having an accurate geometrical model of TBC is the primary step for having a precise and comprehensive simulation model to predict their mechanical properties. Geometrical equations for TBC must be accurate and easy to implement. In addition, geometrical models should be realistic enough to provide precise models simulating TBC's actual shape and behaviour. However, creating a geometrical model without assumptions is not possible. For the geometrical model in this paper, the following assumptions have been made [11]:

Assumption (1): The cross-section of the yarns is assumed to be circular with r radius.

Assumption (2): The yarns are solid and uncompressible. In the actual models, the cross-section of the yarns will change depending on the force applied to the TBC. However, since the yarns in this paper are assumed to be single, solid fiber, they are uncompressible.

Assumption (3): The braid paths do not slip and keep the constant sinusoidal pattern throughout the braid length. TBCs are flexible in nature, specifically open-mesh uncured TBCs. Some yarns might shift from their ideal shapes when inserting an uncured open-mesh TBC into a mandrel. This can happen during the manufacturing process of the cured braid as well. However, the yarns stay in an ideal path in the geometrical model and do not change their position.

The above assumptions consider TBC's overall characteristics; however, they ignore some specifications, such as the flexible nature of yarn paths and variable cross-section shapes. To have a real-shape model that considers all the details and characteristics of a real TBC, other methods like micro-computed Tomography (μCT) can be used [16-17].

μCT is a non-destructive imaging method that can acquire high-resolution 3-D images (voxel size can be less than one micrometre). By using μCT, essential information about TBC is obtained. Bale et al. [20] statistically analyzed the shape and positioning of fiber tow of two ceramic-matrix textile composites in the 3-D woven architecture. Melenka et al. [21] used μCT to analyze porosity/void in braided composites and extract the geometrical parameters of yarns. Wang et al. [22] discussed the microstructure of 3D braided composites and provided a modelling approach based on the Free Form Deformation (FFD) theory. Melenka et al. [23] used high-resolution μCT to identify the fibers of yarns in a 2D TBC.

Different studies have been done to study the behaviour of braided composite by using the FEM method [24– 30]. Lomov et al. [31] developed meso-FE modelling for textile composite. They provide a road map for creating a mesoscale model for obtaining mechanical properties, studying the stress-strain field, and simulating damage in the textile composite within a unit cell. Finally, they compared the developed meso-FEM with Chamis' analytical model [32] and experimental results. The FEM results show closer results to experimental results compared to the analytical model. The WiseTex software package [33] was used to generate the geometrical model, which does not support generating TBC. As a result, the simulation of TBC is not considered in this study.

Xu et al. [34] analyzed flat braided composite by FEM. They modelled braided composite with different braid angles and studied the braid angle's effect on braided composite mechanical properties. They considered unit cells in each case and applied periodic boundary conditions (PBC) to their model. Zhang et al. [35] used the FEM method to simulate braided composite tubes to study the energy absorption of braided composites to improve the crashworthiness of components. In their research, the cross-section of each yarn is assumed to be rectangular and remains constant along the entire yarn path. Also, the axial yarns were assumed to be completely straight, and braiding yarns were considered to follow a straight path. Finally, simulated results were validated by comparing them with experimental test results.

Wang et al. [36] provided a FEM analysis based on a geometrical model. They created a rectangular braided composite by TexGen software, an open-source software package, and used a mapping method to convert the rectangular model into a tubular form. Zhang et al. [37] developed a mesoscale voxel-based FEM for analyzing the effect of the voxel size on the 3D angle-interlock woven composites subjected to axial tensile loading.

In this paper, a new FEM model for braided composites is introduced. The linear solver is used for this modelling. The TBC-Gen program for generating geometrical TBC models is utilized. TBC-Gen can produce yarn paths for all three yarn patterns using different variables. TBC-Gen was created using existing geometrical models from the literature. The program is developed in MATLAB software package, and the generated path will be imported into SolidWorks to make the solid model. A μCT scan was also performed for an open-mesh TBC, and the developed 3-D model was compared against the geometrical model generated by TBC-Gen and SolidWorks. Finally, a FEM based on the geometrical model for analyzing TBC's mechanical performance under the tensile test is developed. Also, the effect of braid angle and braid patterns on the displacement of the TBC is studied. The FEM results are compared against experimental and analytical results for validation purposes. The methodology presented in this manuscript will provide a method to understand the mechanical behaviour of TBC more thoroughly.

6.2 Method

6.2.1 Geometrical Models

The geometrical variables for generating a geometrical model are the number of yarns, braid angle, yarn diameter, mandrel diameter, length, or the number of turns of TBC. Some of the geometrical variables of a Regular braided composite pattern are shown in Figure 6-3. The indicated variables are braid angle (θ), yarn diameter (d), and undulation length. The braid angle is the most critical geometrical variable that significantly affects the mechanical properties of the TBC [38]. Other parameters of TBC and the process for developing each yarn pattern are introduced in Appendix 1.

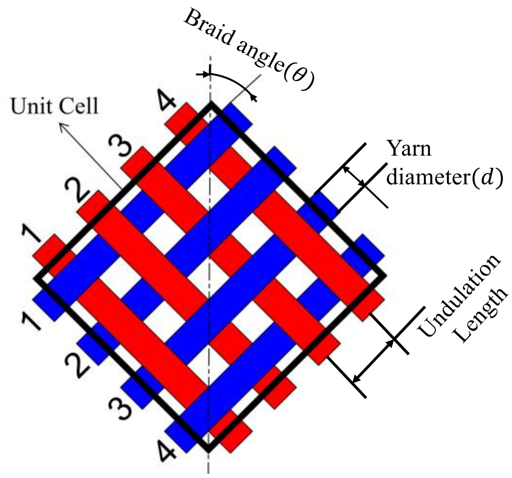

Figure 6-3 A unit cell of a Regular braided composite pattern showing geometrical variables

6.2.2 MATLAB Algorithms Used for Generating Yarn Patterns

To generate all the patterns discussed in the previous sections, a custom-made program named TBC-Gen is designed in the MATLAB software package (R2020B, The MathWorks Inc, Natick, Ma, USA). The algorithm followed in this paper is shown in Figure 6-4. This algorithm starts by defining and importing geometrical values into the TBC-Gen, creating a solid model, and finally importing it into the FEM software package. The complete details for the TBC-Gen geometrical model are presented in Appendix 1.

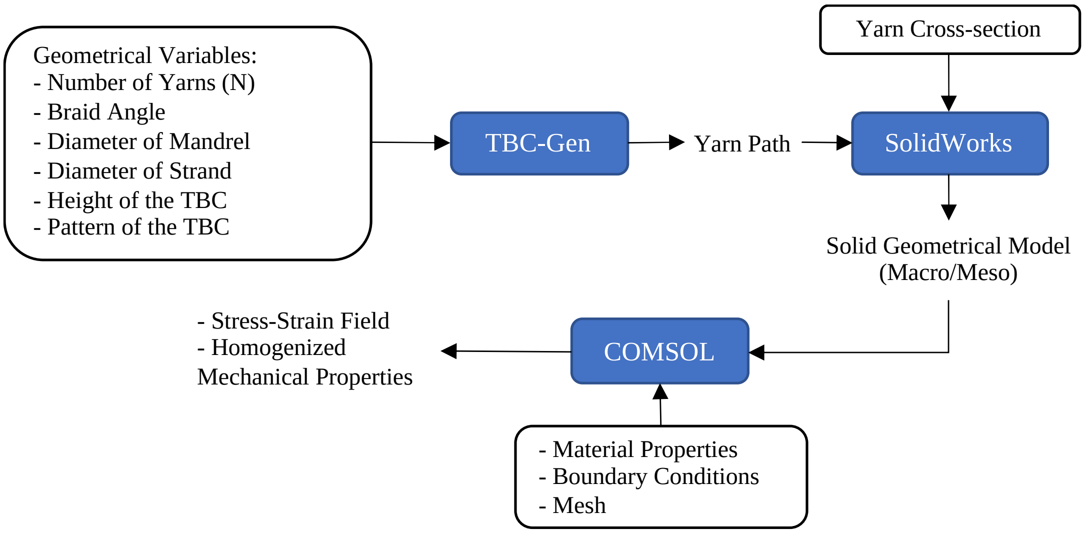

Figure 6-4 The flow chart of the algorithm followed in this paper.

The TBC-Gen needs five input geometrical variables to design the yarn path. Number of yarns, braid angle (in degrees), the diameter of the mandrel in mm (inner diameter of the tubular braid, it should also be considered that the diameter of the mandrel is $2(R-2r)$ in mm), the diameter of the strand ($2r$) in mm, and the number of turns or height of the tubular braid in millimetres (only one of these two variables is required to be inputted, the other variable will be calculated based on the prescribed value). TBC-Gen can produce all three yarn patterns, i.e. Diamond, Regular, and Hercules. The user can select to see the single path of clockwise or counterclockwise yarn or both simultaneously. The updated path will automatically be displayed in the plot section as the user changes the parameters. Finally, the XYZ centre points of the designed yarn path for two counterclockwise yarns and two clockwise yarns and a properties file, including the input parameters, the designed pattern, and date and time, can be exported as five separate text files. Created clockwise or counterclockwise yarn paths can be uploaded and displayed in the TBC-Gen's display window. The XYZ values are also displayed in the program for control purposes. Alternatively, the generated properties file can be uploaded as well. By uploading the properties file, the program will scan and read the parameters and the pattern of the TBC path and change the program's settings accordingly.

6.2.3 Generating the Solid Geometrical Model

The SolidWorks software (version 2020, Dassault Systèmes SOLIDWORKS Corp., Massachusetts, USA) is used to create the geometrical model by adding a cross-section to the designed yarn path in the previous section. First, one clockwise and one counterclockwise yarn path generated in TBC-Gen is imported into SolidWorks. Next, the generated text file in the developed MATLAB program is imported into SolidWorks using the "Curve though XYZ Points…" function. After importing both yarn paths, two circular cross-sections are sketched in the XY plane. At the same time, the circle's centre coincides with the yarn path. The cross-section sweeps the designed path and creates the yarn solid geometrical model using the "Sweep" function. Finally, using the "Circular Pattern," n number of yarns are patterned around the TBC's axis for each of the counterclockwise and clockwise directions (for the Regular pattern, two sets of clockwise and two sets of counterclockwise yarn paths are generated. Therefore, $n/2$ of yarns are patterned around the TBC's axis).

6.2.4 Micro-Computed Tomography (μCT)

μCT is considered a microscopic version of clinical Computed Tomography (CT). For generating 3-D models out of a μCT, the testpiece will rotate around its axis with a predefined step size. The smaller the step size, the more accurate the results. Because of the cylindrical shape of the TBC, only half of the TBC (180°) is required to be scanned. The 2-D images are combined, resulting in a stack of cross-sectional 2-D images. By sticking these 2-D cross-sectional images, a 3-D model of the testpiece is created [39], as shown in Figure 6-5. In Figure 6-5, the X-ray tube produces X-rays and sends them toward the test piece. Then, the X-ray CCD (Charge Coupled Device) detector captures the X-rays that pass the test piece. A motor controls the rotation step of the test piece to take images in different rotations. All the acquired images are transferred to a computer for further image processing.

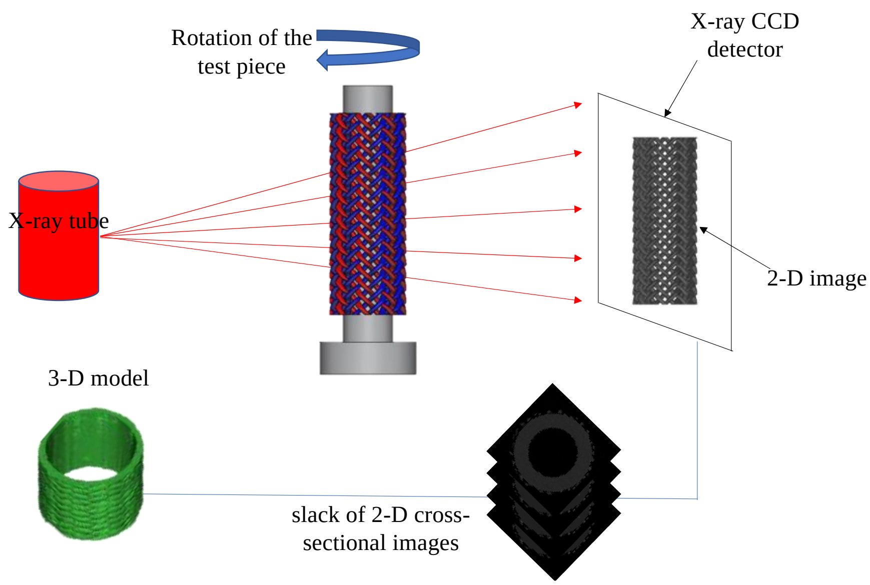

Figure 6-5 μCT component used for scanning a Tubular Braided Composite.

This study examined the TBCs using a desktop μCT scanner (SkyScan 1272, Bruker-MicroCT, Kontich, Belgium). The μCT settings for this scan are tabulated in Table 6-1. An open-mesh, dry (no resin) Kevlar 49 fiber TBC with 48 yarns were used for this experiment. Also, ten different measurements were done at different points of the TBC. The average value for braid angle was 40.53°(with a 5.75° standard deviation), and the average value of yarn width was 0.88 mm (with a 0.14 mm standard deviation). Braid angle and yarn thicknesses were measured by analyzing images taken directly from TBC with a camera and using ImageJ software (National Institutes of Health, USA). Because of the open-mesh TBC's flexible nature, some yarns are distorted and do not stay in their ideal shape. As a result, they do not have a consistent braid angle through the yarn path. A specific 20 mm hollow cylinder mandrel is 3D printed to hold the TBC, and a 5 mm steel mount is inserted at the bottom of the mandrel, shown in Figure 6-6 a). The measured yarn width and braid angle are shown in Figure 6-6 b). After analyzing the µCT images, the cross-section is shown in Figure 6-6 c). 1533 images were taken by scanning 180° of the TBC. By multiplying the number of images by the resolution of the scan (10.88 μm), the height of the scanned TBC would be 16.68 mm. A circular subtractive region of interest is defined within the mandrel cross-section to remove the mandrel from the cross-section. The resulting cross-section is shown in Figure 6-6 d). Next, the cross-section images are binarized to increase the contrast between the background and yarns. By doing so, the yarn detection process would be more straightforward. As shown in Figure 6-6 e), the mandrel diameter is measured by fitting a circle into the inner side of the cross-section.

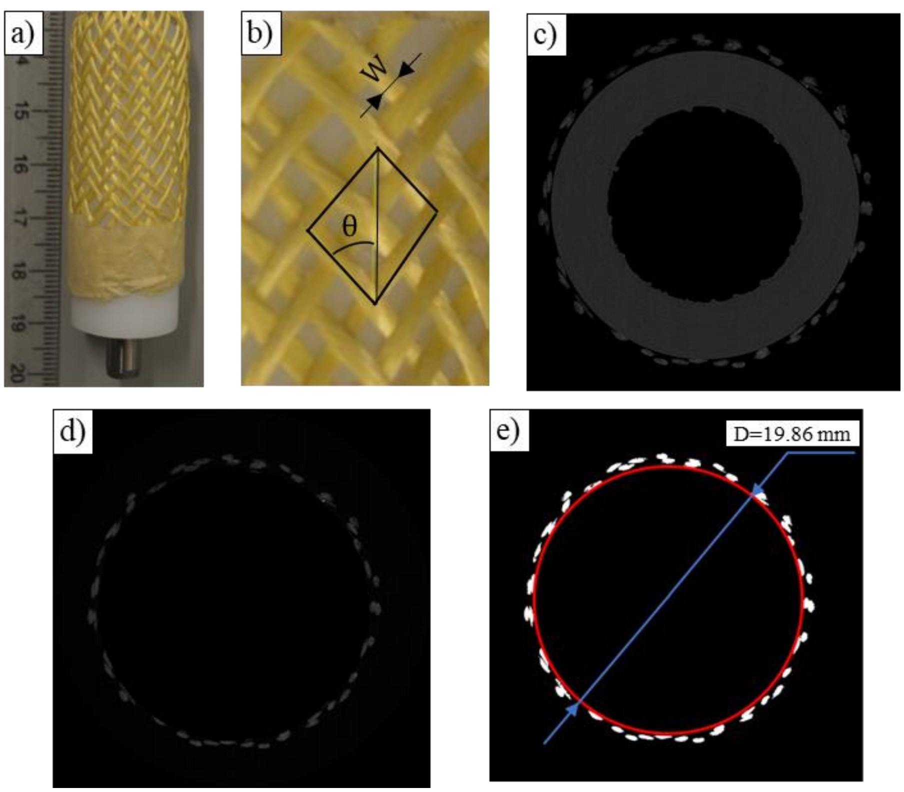

Figure 6-6 a) The tested TBC inserted into the mandrel next to a ruler, b) measuring the actual geometrical variable of TBC by evaluating the image in ImageJ software, c) the μCT result of the cross-section of the scanned TBC, d) removing the mandrel by defining a subtractive region on the interest mask, and e) binarized cross-section and measuring the mandrel diameter in ImageJ software.

Table 6-1 The setting of the μCT experiment

μCT parameters	Value
Image pixel size	10.88 μm
Source Voltage	55 kV
Source Current	166 μA
Number of scanned Images	1533
Exposure	1876 ms
Rotation step	0.1°
Rotation angle	180°
Frame Averaging	4
Duration	4 hour and 35 minutes

The 2D images taken by μCT were imported into NRECon software (NRECON 1.7.1.0, Bruker, Belgium) to reconstruct the 2D cross-sectional images like the image shown in Figure 6-6 c). These images are 8-bit bitmap (BMP), and the size of the created images was 2452 × 2452 pixels. A 3-D model of the scanned TBC is generated after importing the cross-section images into CTAn software (Bruker-MicroCT, Kontich, Belgium). The result is shown in Figure 6-7 a). Also, the virtual geometrical model of the scanned TBC is generated by the TBC-Gen and SolidWorks and is shown in Figure 6-7 b) for comparison with the μCT model.

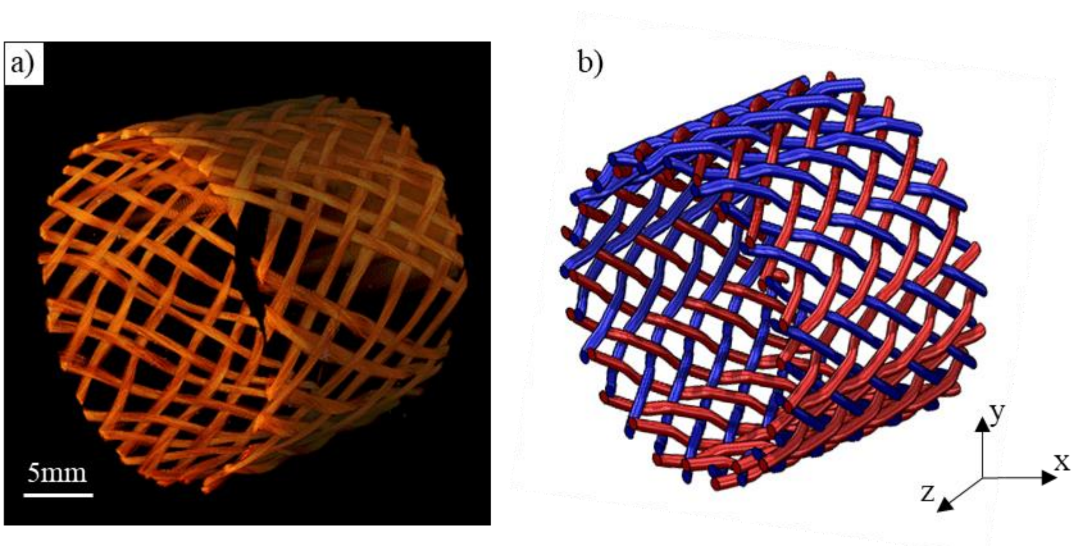

Figure 6-7 a) The 3D result model of the TBC generated by CTAn software, b) the generated geometrical model using the TBC-Gen program. Red: counterclockwise, blue: clockwise

Image processing algorithms of MATLAB are used to analyze the yarn cross-sections. First, the binarized images are scanned using “bwboundaries” function. The scanned cross-section image and the detected yarn boundaries are shown in Figure 6-8 a). A closer view of six yarn cross-sections with their calculated area is shown in Figure 6-8 b). By detecting the yarn boundaries, other parameters of the yarns, like major and minor diameters, area, orientation, and centre, are obtained, as shown in Figure 6-8 c). The major and minor diameters of the detected boundary are the major and minor diameters of an assumed ellipse fitted to the detected cross-section boundary. Also, the boundary orientation is the angle between the yarn's major diameter and horizontal axis in degrees.

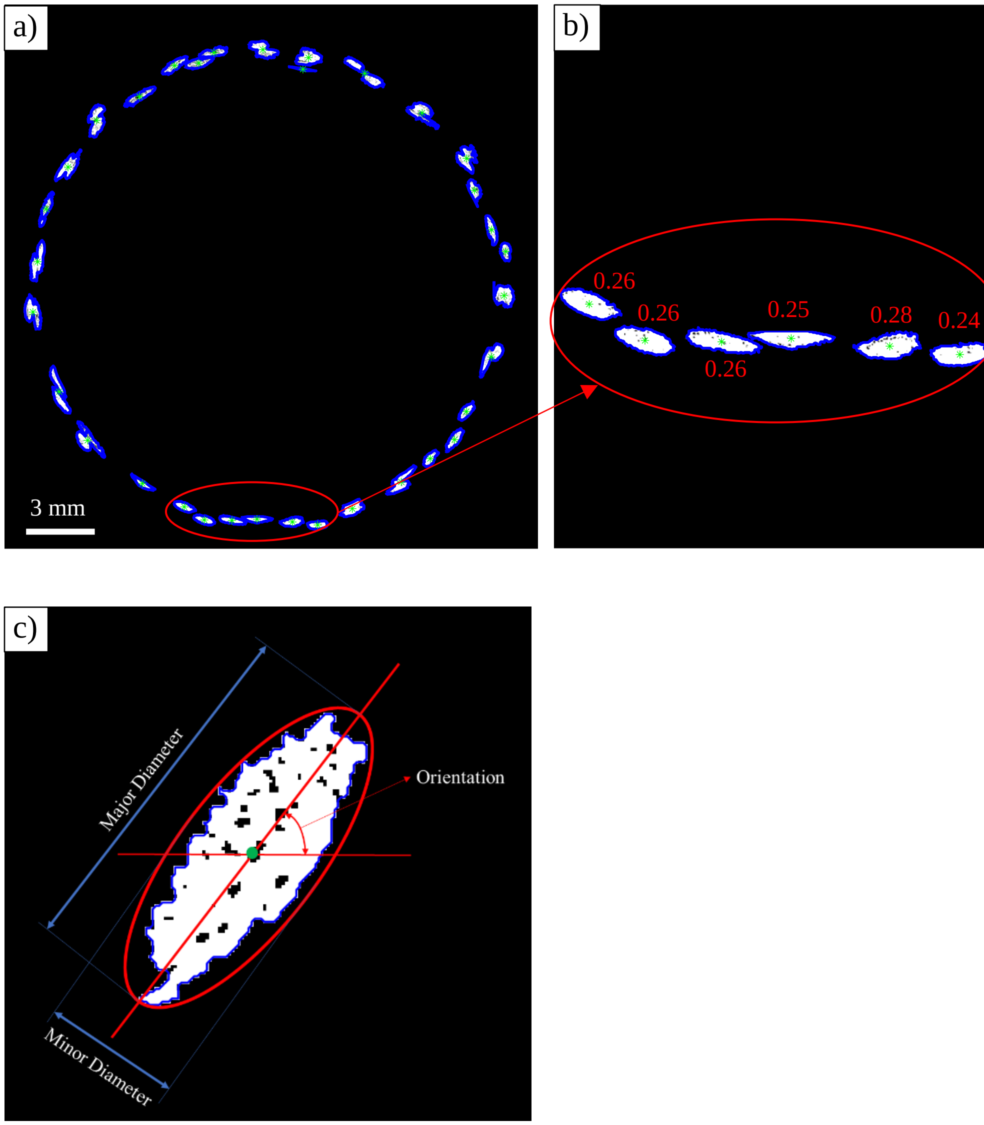

Figure 6-8 a) Detected boundaries of yarn cross-sections, b) six detected yarn boundaries, the center of yarns, and the area of yarn cross-section (mm^2), and c) a detected yarn cross-section showing major and minor diameters, yarn canter, and orientation in MATLAB software.

6.2.5 Finite Element Modelling

The constitutive behaviour of complex material like TBC can be studied by experimental tests or numerical simulation. TBC can be studied at three hierarchical structural levels: macro, meso, and micro levels [31]. The macro-level consists of the overall geometry of the TBC material. The global condition at the macro-scale refers to the complete loading condition of the TBC. The micro-scale deals with the arrangement of the fibers in the impregnated yarn. Local properties on a micro-scale refer to the actual properties of fiber and matrix. The size and mechanical properties of the mesoscale are between the macro-scale and micro-scale. In other words, the local properties on mesoscales refer to global properties on a micro-scale. Also, global properties on a mesoscale refer to local properties on a macro scale [31]. A sample of micro-scale, mesoscale and macro-scale models of a TBC is shown in Figure 6-9. For the FEM of the TBC, it is assumed that the fibers are perfectly bonded to the matrix [40].

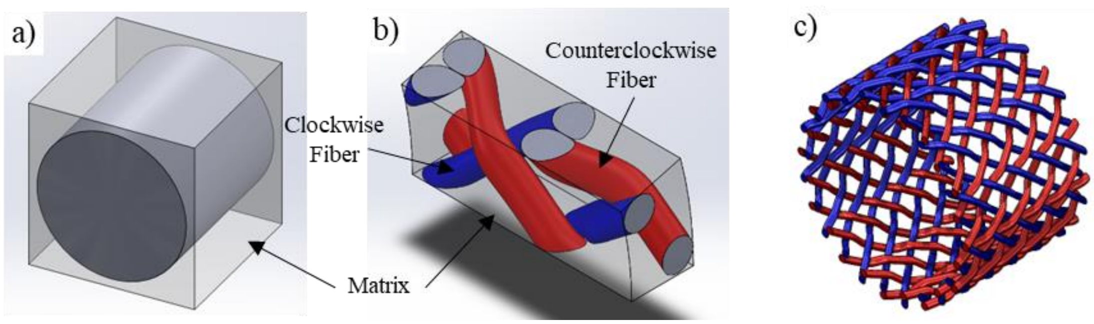

Figure 6-9 a) micro-scale, b) mesoscale, and c) macro-scale models of tubular braided composite clockwise (red) and counterclockwise (blue)

For generating the FEM, a geometrical model of an open-mesh Diamond TBC with 18 yarns, 30° braid angle, 24.71 mm inner diameter (diameter of the mandrel), 1.51 mm strand diameter, and 30 mm length is designed. The matrix is added to the designed geometry. The thickness of the matrix is intended to be more than the fibers to prevent zero thickness when generating the geometrical model and meshing step. As a result, the inner diameter of the matrix is 24 mm. The macro-scale and mesoscale (40° cross-section of the complete model, $2\pi/n$) models are shown in Figure 6-9 a) and Figure 6-9 b), respectively. The designed model is imported into the FEM software package (COMSOL Multiphysics 5.5, Stockholm, Sweden) for analysis.

6.2.5.1 Periodic Boundary Conditions

Geometric periodicity in structures is an important feature that can be used to reduce the size of the structure under analysis by introducing a unit cell. In some research, the rectangular coordinate system is used, while in others, the coordinates are updated to consider similar conditions for cylindrical frames [41]. In this research, the cylindrical coordinates are used.

Periodic Boundary Condition (PBC) is a set of boundary conditions used for evaluating a large component only by solving a small part of the problem (unit cell). Assuming the unit cell is characterized by a transition vector ($\overrightarrow{b_1}$) as shown in Figure 6-10 c), the translation equation would be as Equation 6-1.

$$A' = A + \overrightarrow{b_1} \qquad \text{Equation 6-1}$$

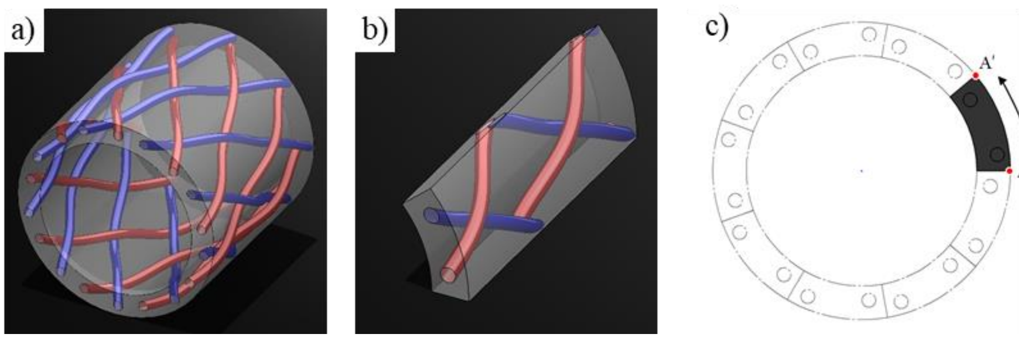

Figure 6-10 The geometrical designed model with 18 yarns, 30° braid angle, 24.71 mm inner diameter, 1.51 mm strand diameter, and 30 mm length. a) macro-scale model, b) mesoscale model

In COMSOL, the boundary condition expressed in Equation 6-1 can be applied by choosing cyclic symmetry under the periodic boundary condition. A critical point for using PBC is keeping the meshes consistent, and COMSOL automatically considers this point. One method for manually controlling the consistency of the meshing is copying the nodes from one side of the unit cell to the other side and then meshing the area between these two surfaces. In this case, the meshes on both sides of the unit cells are identical [31].

The imported model into COMSOL software under the tensile test is shown in Figure 6-11. The yarn material is assumed to be Kevlar 49 fiber, and for the matrix Epon825/Ancamine 1482 resin. The properties of both materials are tabulated in Table 6-2.

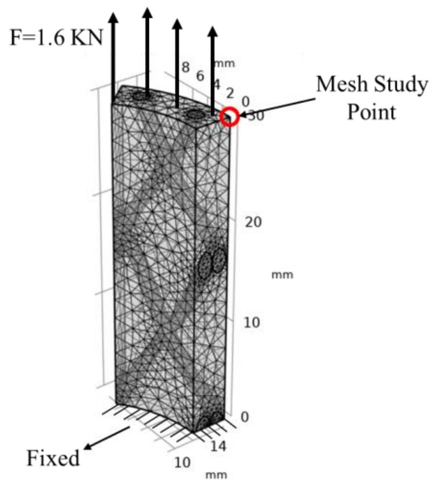

Figure 6-11 Imported mesoscale geometrical model into COMSOL software after meshing, under tensile test, and after applying PBC

Table 6-2 Properties of the material used in FEM [42]

Kevlar 49 fiber		Epon825/Ancamine 1482 resin	
$\{E_1, E_2, E_3\}$	{130,7.3,7.3} (GPa)	E	3.5 (GPa)
$\{G_{12}, G_{23}, G_{13}\}$	{2.86,6.89,2.86} (GPa)	υ	0.3
$\{\upsilon_{12}, \upsilon_{23}, \upsilon_{13}\}$	{0.35,0.35,0.35}	ρ	1100 (Kg/m^3)
ρ	1800 (Kg/m^3)		

Figure 6-12 a) and Figure 6-12 b) show the local coordination of a single yarn and the global coordination of a TBC, respectively. In the local coordination, direction 1 is alongside the yarn. Directions 3 and 2 are perpendicular to direction 1, and direction 3 is perpendicular to the image shown in this figure. The yarn properties are assigned based on local coordination, and the procedure explained in [43] can be followed to transfer these properties to global coordination.

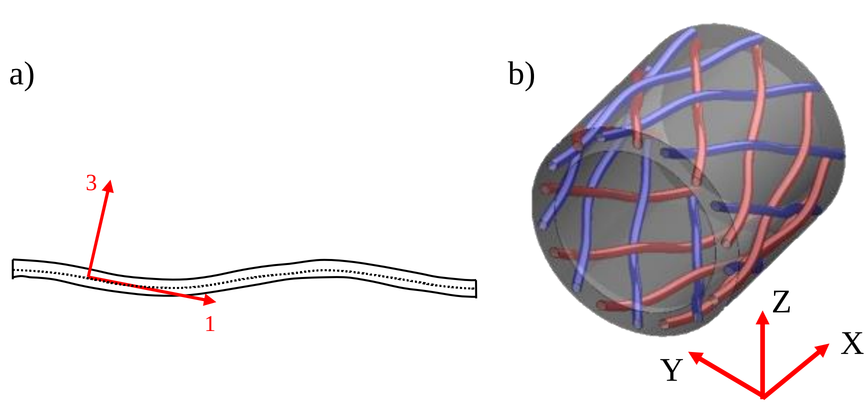

Figure 6-12 Coordination system for tubular braided composites. a) local coordination of a yarn where 1 is alongside the yarn, b) global coordination of the TBC

A free tetrahedral mesh (with four nodes, six elements, and three faces) is used to analyze the model, as shown in Figure 6-11. However, a mesh study is required to find the optimum size of the mesh. Therefore, nine mesh categories are used to analyze the mesoscale model represented in Figure 6-11. The mesh categories start from coarse to fine. The number of elements (NO_e), maximum element size (max_e), minimum element size (min_e), maximum element growth rate (growR), curvature factor (ResCurv), and resolution of narrow regions (ResNar) are parameters of each category which are tabulated in Table 6-3.

Table 6-3 Parameters of each mesh category used for the mesh study

Mesh Category	Extremely course (1)	Extra course (2)	Coarser (3)	Coarse (4)	Normal (5)	Fine (6)	Finer (7)	Extra fine (8)	Extremely fine (9)
NO_e	2313	3013	4552	10284	29519	65008	182757	388722	942064
max_e	10.7	6.39	4.05	3.2	2.13	1.7	1.17	0.746	0.426
min_e	1.49	1.15	0.852	0.597	0.384	0.213	0.0852	0.032	0.00426
growR	2	1.85	1.7	1.6	1.5	1.45	1.4	1.35	1.3
ResCurv	1	0.9	0.8	0.7	0.6	0.5	0.4	0.3	0.2
ResNar	0.1	0.2	0.3	0.4	0.5	0.6	0.7	0.85	1

Three outputs are captured at the mesh study point using each mesh category shown in Figure 6-11: the von Mises stress, the first principal stress, and the displacement. Von-misses stress is equivalent to yield point stress. The stress value at the plastic or yield point stages can be determined using the von Mises stress. The yield point refers to the starting point of plastic deformation. When the von Mises stress reaches a specific value, referred to as yield strength, the material is considered to have begun to yield. The von Misses stress is used to predict the yielding of materials under complex loading from the result of a uniaxial tensile test [43].

A 1.6 KN force is applied to the upper side of the model alongside the TBC. The recorded values of each mesh category and their relevant percentage differences are plotted separately and shown in Figure 6-13. The percentage difference is calculated as (the value of mesh size (2) − the value of the mesh size (1)) / the value of mesh size (1).

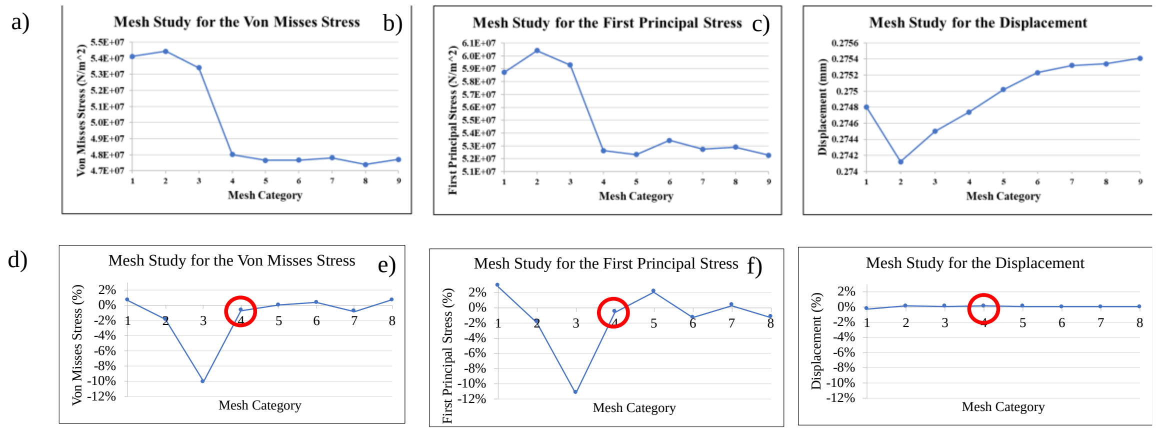

Figure 6-13 Mesh study on a mesoscale model at one point under tensile test. a) mesh study result for von Misses stress, b) mesh study result for first principle stress, c) mesh study result for displacement, d) percentage difference between Von Misses results in different mesh sizes, e) percentage difference between First Principal stress results in different mesh sizes, f) percentage difference between Displacement results in different mesh sizes.

After category 4 (coarse mesh), the stress value does not change significantly for Von Misses stress; the difference is below 1%. The stress values converge after mesh category 4 (coarse mesh) for the first principal stress, and the percentage difference is below 2%. Finally, the percentage difference in all the mesh categories is below 0.25% for the displacement. As a result, category mesh 4 (coarse mesh) will provide enough accurate results for this study, and finer mesh will refine the results by less than 2%. At the same time, it would be more computationally expensive.

6.3 Results

6.3.1 Geometrical Model

A TBC solid geometrical model sample from each TBC pattern (Diamond, Regular, and Hercules) with similar geometrical parameters is generated using TBC-Gen and SolidWorks. The inputted parameters are the Number of yarns $= 32$, Yarn radius $= 0.5\ mm$, Mandrel radius $= 10\ mm$, Braid angle $= 45°$, and length of TBC = 50 mm. The generated solid models are shown in Figure 6-14.

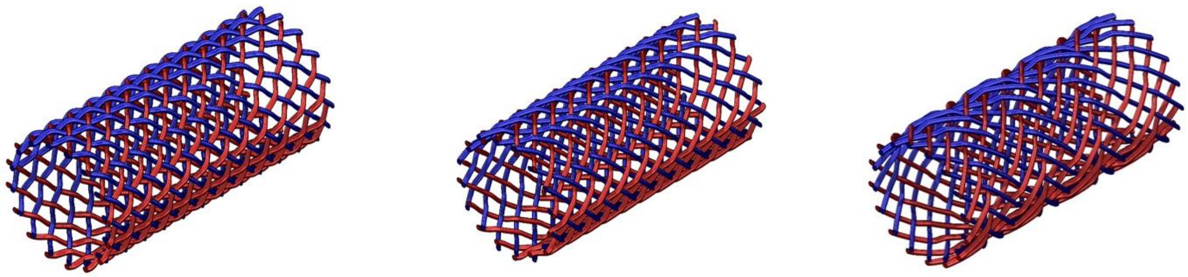

a) Diamond	b) Regular	c) Hercules
N = 32	N = 32	N = 32
r = 0.5 mm	r = 0.5 mm	r = 0.5 mm
R = 10 mm	R = 10 mm	R = 10 mm
$\alpha = 45°$	$\alpha = 45°$	$\alpha = 45°$
L = 50 mm	L = 50 mm	L = 50 mm

Figure 6-14 3-D solid model of a TBC, red: counterclockwise, blue: clockwise a) Diamond pattern, b) Regular pattern, and c) Hercules pattern

For validation of the developed geometrical model in this paper, a Regular TBC with Number of yarns = 16, Braid angle = 35°, Mandrel radius = 10 mm, Yarn radius = 0.5 mm, and length of the TBC = 98.7 mm is designed in both the TBC-Gen and a commercial software package, TexMind Braided software [44]. The output results of the two software are shown in Figure 6-15. The visual comparison between the two models shows a good agreement between them.

a)

b)

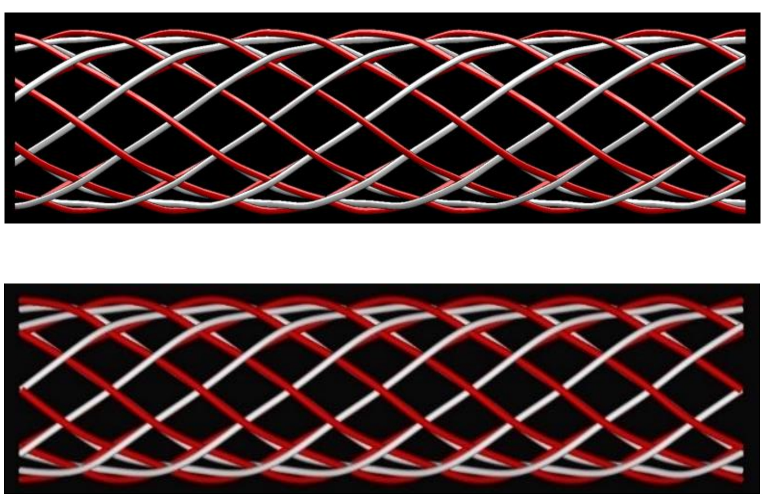

Figure 6-15 Comparing the result of the generated geometrical TBC model designed by the algorithm developed in this paper a), with the results of the same TBC designed in TexMind Braided software commercial software b). ($N = 16$, α = 35°, R = 10.5 mm, r = 0.5 mm, and the length of the TBC = 98.7 mm)

The TBC-Gen can generate yarn paths as X, Y, and Z coordination points. Then, this yarn path will be imported into SolidWorks software to add a cross-section. This cross-section can be in various shapes, while in the TexMind software, the only cross-section is circular. Also, in the TBC-Gen, the composite material can be modelled in SolidWorks software by adding a matrix to the designed TBC.

6.3.2 Micro-Computed Tomography (μCT)

The cross-sectional images shown in Figure 6-8 demonstrate the process for detecting the yarn cross-sections and obtaining other data of a TBC. Some valuable data from the yarns can be extracted by analyzing all the cross-sectional images and detecting yarn cross-section boundaries. The average value of major diameter for all the single yarn cross-sections is 1.078 ± 0.222 mm. Also, the average value of 10 measurements of the actual TBC using a camera and ImageJ software reveals the major diameter of 0.887 ± 0.146 mm. The measured major diameters and the relevant SD are shown in Figure 6-16. However, the μCT measured the major diameter of yarns, which shows a bigger value than the measured major diameter using the camera. One reason for this difference is the curvature of the TBC. Since the camera measurements are based on a single image taken in the longitudinal direction of the TBC, the measured values will be smaller than the actual diameter. However, the μCT measurements are based on the TBC's cross-sectional images, which also consider curvature.

Additionally, the camera measurements are the mean of 10 measurement samples. However, the μCT measurements represent the average value of all the single cross-sectional yarns, making them more accurate.

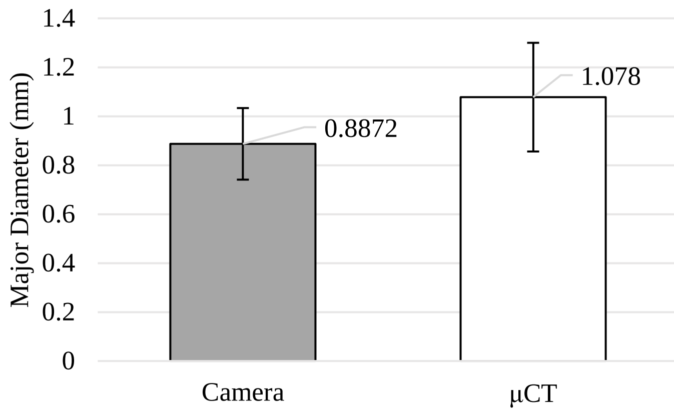

Figure 6-16 Major diameter of a TBC measuring by a camera and μCT

The average value of the cross-section area of the scanned TBC is 0.2803 ± 0.0386 mm^2. The relevant radius resulting in the same area with a circular cross-section is 0.3 mm to achieve an equivalent cross-sectional area. This radius can be used in TBC-Gen to generate the solid geometrical model that can be used for FEM analysis. The average value of the minor diameter of the scanned TBC was 0.3631 ± 0.0523 mm.

By visually comparing the virtual simulated model with the μCT model in Figure 6-7, the assumptions made for developing the simulation model are apparent. As one can see, the yarns in actual open-mesh TBC are not located in their ideal location, and some are significantly distorted. Additionally, the cross-section of yarns in the simulated model is assumed to be incompressible and circular, which is not entirely similar to the μCT results. However, the overall shape of both models is identical. For better comparison, a quantitative comparison between the two models must be done in further studies. To make this quantitative comparison, all the cross-section images of the selected yarn should be scanned. After extracting the data of boundary, centre points, and the area of the yarn cross-section, they can be compared against the geometrical yarn path generated by TBC-Gen.

6.3.3 Finite Element Modelling

6.3.3.1 The Effect of Braid Angle on Displacement

This section will evaluate seven models with similar geometries and mechanical properties but different braid angles. The displacement of each model will be recorded and compared against each other. The braid angles range from 30° to 60° with a five-degree incremental step. The mechanical properties of the fiber and matrix are according to Table 6-2, and the applied force is 12.5 KN in the Z direction. Other geometrical variables of the TBC are similar to the TBC shown in Figure 6-11. Three FEM results ($\theta = 30°$, $\theta = 40°$, $\theta = 60°$) out of seven cases are shown in Figure 6-17.

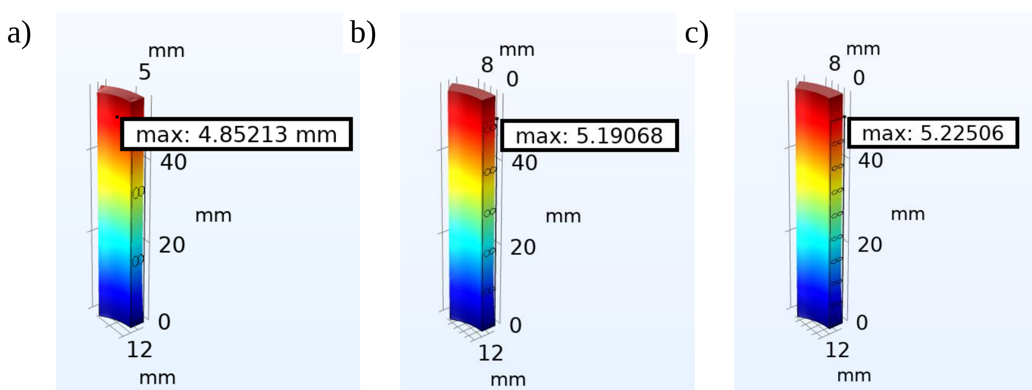

Figure 6-17 Displacement of Diamond tubular braided composite with $N = 18$, $R = 12.35\ mm$, $r = 0.75\ mm$ with braid angles between 30° to 60° under 12.5 KN tensile load. a) $\theta = 30°$, b) $\theta = 45°$, c) $\theta = 60$

The displacement value of all seven cases and the trending line is shown in Figure 6-18. As one can see, by increasing the braid angle, the longitudinal strength of the braid decreases, and as a result, the displacement of the TBC increases.

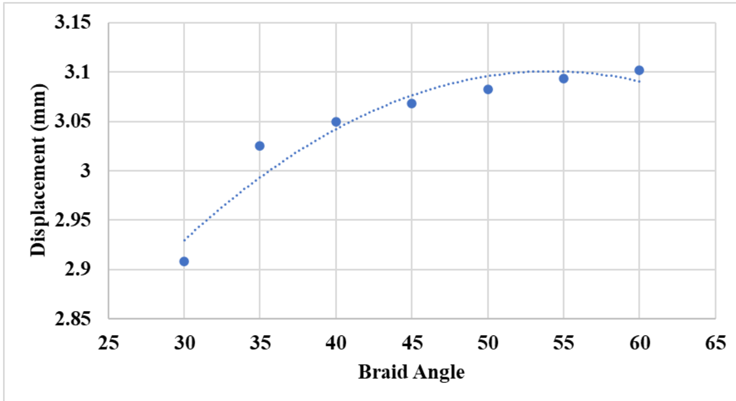

Figure 6-18 The effect of changing the braid angle on the displacement of the TBC.

6.3.3.2 The Effect of Yarn Pattern on Displacement

Three geometrical models with similar geometrical variables but different yarn patterns, as shown in Figure 6-14, are imported into COMSOL. A tensile test is designed for braid patterns, PBC, and a 12.5 KN longitudinal force is applied. The fiber material is assumed to be Carbon fiber, and the matrix is Epson 825/Ancamine 1482 resin. The mechanical properties of fiber and matrix are tabulated in Table 6-4. Roller boundaries constrain the lower part of the TBC.

Table 6-4 Properties of fiber and matrix used for the experimental test, analytical model, and FEM [42]

	$E_{f11}(GPa)$	$E_{f22}(GPa)$	$G_{f11}(GPa)$	$v_{f11}(GPa)$
Kevlar 49 fibers	130	7.3	2.86	0.35
Carbon fiber	220	13.8	9.0	0.2
S2-glass	96.5	96.5	39.2	0.23
	$E_m\ (GPa)$		$G_m\ (GPa)$	$v_m\ (GPa)$
Epson 825/Ancamine 1482 resin	3.5		1.3	0.3

The displacement in the Z direction of each braid pattern is calculated and shown in Figure 6-19. The figure shows that Diamond's maximum displacement in the Z direction is 0.8118 mm, Regular 0.8104 mm, and Hercules = 0.8098 mm. Also, the maximum displacement is located on the top surface of the TBC. Thus, diamond patterns show maximum displacement compared to the two other patterns. It is because of the one-by-one woven structure of the Diamond that it causes less longitudinal stiffness.

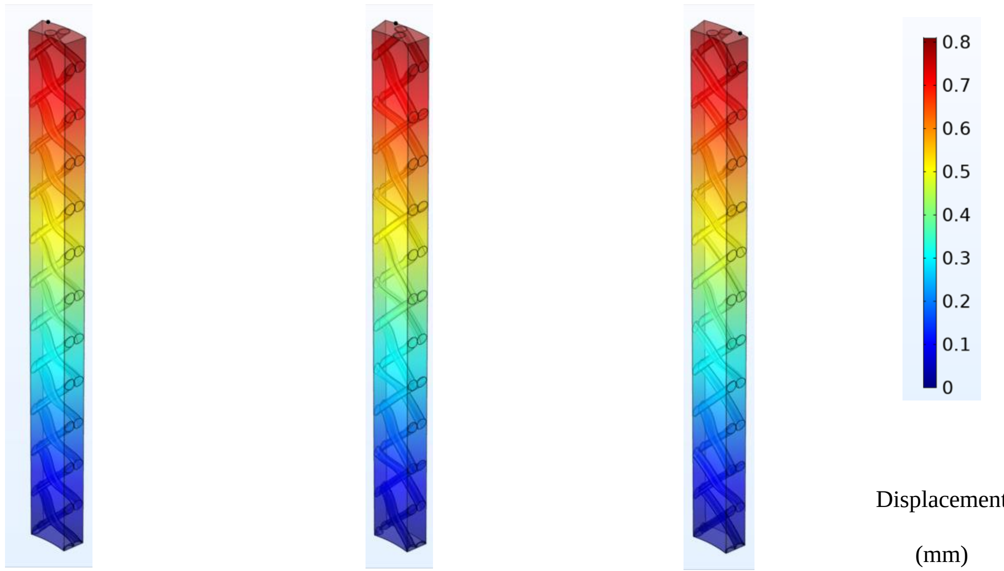

a) max displacement: 0.8118 mm

b) max displacement 0.8102 mm

c) max displacement: 0.8098 mm

Figure 6-19 Tensile test of three carbon fiber TBC’s with different yarn patterns under 625 N longitudinal force. a) Diamond, b) Regular, and c) Hercules

6.3.4 Validation

For Validation, the longitudinal modulus (E_{xx}) of three TBCs with different geometry and material properties are calculated by the FEM and compared against the tensile experiment and analytical results reported in [42]. The material of three fibers is Kevlar 49 fibers, Carbon fibers, and S2-glass fibers. The matrix is also Epson 825/Ancamine 1482 resin.

Five samples of Kevlar and Carbon fibers and four samples of S2-glass were prepared for the experimental test. The average dimensions of the samples are tabulated in Table 6-5.

Table 6-5 Average geometry of the three used TBCs [42]

	Number of Yarn (N)	Diameter of Mandrel (mm)	Braid angle (deg)	Diameter of yarn (mm)
Kevlar 49 fibers	18	24.71 $\pm$0.28	44.19 $\pm$1.63	1.51 $\pm$0.15
Carbon fiber	18	24.54 $\pm$0.19	41.80 $\pm$0.11	1.58 $\pm$0.09
S2-glass	18	24.53 $\pm$0.47	46.00 $\pm$1.30	1.48 $\pm$0.04

The experimental longitudinal modulus was measured from a tensile test. The curved model based on Classical Laminate Plate Theory (CLPT) was used to predict the analytical results for each case. In modelling the FEM, a predefined displacement was applied to the TBC model. Then, the relevant stress and strain were calculated accordingly. The mandrel and yarn diameters were considered constant for each sample, and the reported average value was used. However, the three braid angles (the nominal braid angle, the maximum braid angle, and the minimum braid angle as tabulated in Table 6-5.) were used for generating solid models and estimating the value and standard deviation of the E_{xx}. Since n = 9, 1/9 ($2\pi/9 = 40°$) of the complete TBC was used to model the FEM, and the PBC was applied to that partial model. E_{xx} was calculated by dividing the stress values by strain.

In the experimental test, the E_{xx} was also calculated as the slope of the stress-strain curve, and the test was repeated for all the samples. For Kevlar 49 TBC, the average value of the experimental E_{xx} was 2.85 ± 0.49 GPa, and for the curved model, it was 4.15 ± 0.67 GPa. Therefore, the difference between the experimental and analytical models is 46%. The FEM reported $E_{xx} = 3.19$ $\pm$ 0.19 GPA, which resulted in an 18% difference compared to the experimental results. A T-test is applied to each comparison for further comparison of the obtained values, and the Probability Value (P-value) of each comparison is reported in Table 6-6.

The t-test is a statistical method used to determine whether there is a significant difference between the means of two groups. It is commonly employed when the sample sizes are small and the data is assumed to follow a normal distribution.

The t-test operates under the null hypothesis, which shows that there is no significant difference between the means of the two groups being compared. It calculates the probability that the observed difference in sample means could have occurred under the null hypothesis. The resulting t-value is then compared against a critical t-value from the t-distribution, determined by the degrees of freedom and the chosen significance level (commonly 0.05) [45]. Then, a P-value is calculated using Equation 6-2.

$$Z = \frac{\hat{p} - p0}{\sqrt{\frac{p0(1-p0)}{n}}} \qquad \text{Equation 6-2}$$

Where $\hat{p}$ is the sample proportion, $p0$ is the assumed population proportion in the null hypothesis, and n is the sample size.

If the P-value is greater than 0.05, the null hypothesis is not rejected, and there is no significant difference between the data points. If the P-value is smaller than 0.05, the null hypothesis is rejected, meaning there is a significant difference between the data sets.

The P-value between Experimental and FEM results for Kevlar 49 TBC is about 14%. As a result, it does not reject the null hypothesis, which means there is not a significant difference between FEM and Experimental results.

Table 6-6 P-Value of the estimated E_{xx}

Material of the TBC	Type of the test	FEM	Experiment
Kevlar 49 fiber	Experiment	0.1415	
	Curved Model	0.1376	0.0565
Carbon fiber	Experiment	0.2582	
	Curved Model	0.0024	0.0027
S2-glass	Experiment	0.0013	
	Curved Model	0.0154	0.0005

The estimated values of the Curved model for E_{xx} of Carbon fiber is 8.88 $\pm$1.35 GPa, and the reported experimental value is 3.03 $\pm$0.77 GPa. The error between analytical and experimental values for Carbon TBC is 193%. The FEM E_{xx} value for Carbon fiber TBC is 3.61 plus or minus 0.015 GPa which shows a 19% error compared to the value of the experimental test for Carbon fiber. Also, the T-test P-value between Experimental and FEM values is 26%, not rejecting the null hypothesis. Therefore, there is no significant difference between the two values.

Finally, the reported experimental value for E_{xx} of S2-glass fiber is 1.44 ± 0.11 GPa, and the analytical Curved model result is 6.41 ± 0.82 GPa. The error between the curved model and the experimental result is 345%. However, the FEM reported 4.11 ± 0.56 GPa for E_{xx} which results in a 185% error. The T-test P-value between Experimental and FEM values is almost 0%, and it rejects the null hypothesis. Therefore, there is a significant difference between FEM and Experimental results. This significant difference might be because of the assumed mechanical properties of S2-glass, which is to be isotropic. Also, the reported mechanical properties might not be accurate.

As a result, there is no significant difference between FEM and experiment results for Kevlar 49 fiber and Carbon fiber material. For the S2-glass material, the result of FEM shows a minor error than the curved model's result. The bar chart of tests for the three materials with their error bars is shown in Figure 6-20.

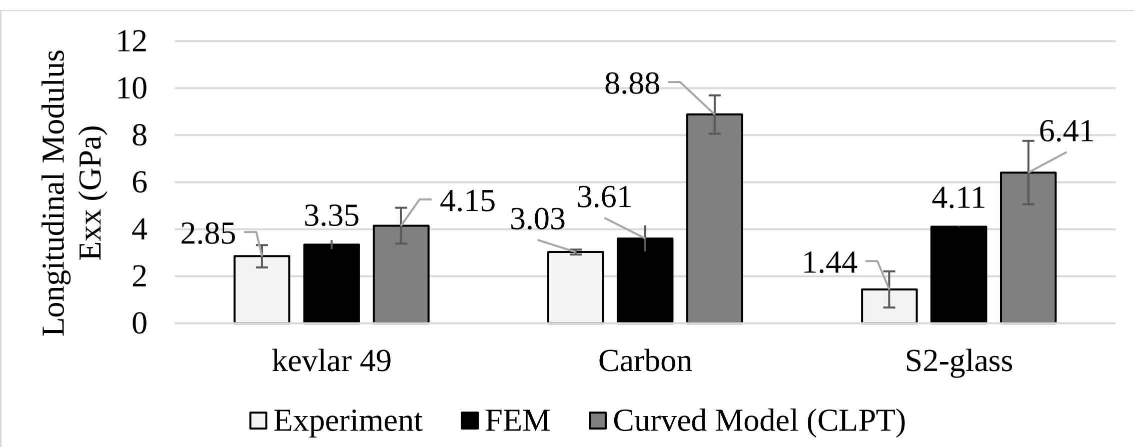

Figure 6-20 Comparing the results of experimental tensile tests for Kevlar 49 fiber, Carbon fiber, and S2-glass fiber with the relevant results of FEM and Curved-model

There might be several different sources contributing to an error in the FEM. One of the reasons might be the geometrical models used for the analysis. The geometrical model is made based on assumptions. For example, in actual open-mesh TBCs, the yarns are usually distorted from their location, as shown in Figure 6-7, while in the geometrical model, they are assumed to be in their ideal shape. Also, the cross-section of the yarns changes throughout the yarn path in the actual model, while they are constant in the geometrical model. These assumptions add error to the model, and they can be reduced by using the actual geometrical model created by the μCT method.

6.4 Conclusion

In this paper, the geometrical models for TBC patterns were introduced. Also, the process for generating these models using the TBC-Gen program developed in the MATLAB software package was explained. Finally, the generated yarn paths were imported into SolidWorks for adding cross-section and creating a solid model, which can be used for further analysis in FEM software packages.

Micro-computed tomography (μCT) was also used to obtain an accurate model of a TBC sample. Using the TBC-Gen, a geometrical model with the same geometrical variables of the µCT scanned TBC was generated and visually compared with the resulting 3-D model of mu cap C cap T. Also, the μCT measured yarn cross-section area can create an equivalent area for the geometrical model.

A FEM was developed under tensile testing, and the effect of braid angle on the displacement was studied. It was seen that as the braid angle increases, the displacement increases respectively. Also, the effect of the braid pattern on displacement was studied, and the Diamond pattern showed the maximum displacement compared to the other patterns. A mesh study was carried out to choose the appropriate mesh size. Finally, the FEM tensile tests were simulated for three different materials. The resulting longitudinal modulus was compared against the experimental and analytical models by running a T-test. The FEM results were estimating the longitudinal modulus values more accurately than the analytical Curved model. The FEM model estimated the longitudinal modulus of Kevlar 49 fiber and Carbon fiber with 18% and 19% error, respectively.

The methodology represented in this manuscript will help to quickly design and analyze TBCs with different yarn patterns and geometrical variables for the desired application. Also, the represented μCT results show this method's potential and accuracy for obtaining valuable geometrical variables. However, for having a quantitative comparison between μCT model and the geometrical model, more studies are required. It is expected that using μCT models for FEM will provide more accurate results.

6.5 Conflict of Interest

The author declares no conflicts of interest with respect to the research, authorship or publication of this article.

6.6 Data Availability Statement

The raw/processed data required to reproduce these findings cannot be shared at this time as the data also forms part of an ongoing study.

6.7 Acknowledgements

The author would like to acknowledge the Natural Sciences and Engineering Research Council (NSERC) Canada RGPIN- 2018-05899. CMC Microsystems provided the software used in this study.

6.8 Supplementary Material

TBC-Gen program is available at the following address: https://github.com/aligholamiYork/TBC-Gen

6.9 References:

[1] A. K. Kaw, *Mechanics of composite materials*. CRC press, 2005.

[2] C. Ayranci and J. Carey, "2D braided composites: A review for stiffness critical applications," *Compos Struct*, vol. 85, no. 1, pp. 43–58, Sep. 2008, doi: 10.1016/J.COMPSTRUCT.2007.10.004.

[3] G. W. Melenka and J. P. Carey, "Development of a generalized analytical model for tubular braided-architecture composites," *J Compos Mater*, vol. 51, no. 28, pp. 3861–3875, Dec. 2017, doi: 10.1177/0021998317695421.

[4] J. Carey, A. Fahim, and M. Munro, "Design of braided composite cardiovascular catheters based on required axial, flexural, and torsional rigidities," *J Biomed Mater Res*, vol. 70B, no. 1, pp. 73–81, Jul. 2004, doi: 10.1002/jbm.b.30017.

[5] Y. Kyosev, *Recent developments in braiding and narrow weaving*. 2016.

[6] Z. M. Huang, "The mechanical properties of composites reinforced with woven and braided fabrics," *Compos Sci Technol*, vol. 60, no. 4, pp. 479–498, Mar. 2000, doi: 10.1016/S0266-3538(99)00148-7.

[7] L. Xu, S. J. Kim, C.-H. Ong, and S. K. Ha, "Prediction of material properties of biaxial and triaxial braided textile composites," *J Compos Mater*, vol. 46, no. 18, pp. 2255–2270, Aug. 2012, doi: 10.1177/0021998311431353.

[8] J. P. Carey, *Handbook of advances in braided composite materials: Theory, production, testing and applications*. Woodhead Publishing, 2016.

[9] F. K. Ko, "Braiding," *ASM Int. Eng. Mater. Handbook.*, vol. 21, 2001, doi: 10.1361/asmhba0003361.

[10] Tianyi Liao and S. Adanur, "3D Structural Simulation of Tubular Braided Fabrics for Net-Shape Composites," *Textile Research Journal*, vol. 70, no. 4, pp. 297–303, Apr. 2000, doi: 10.1177/004051750007000403.

[11] A. Rawal, P. Potluri, and C. Steele, "Prediction of Yarn Paths in Braided Structures Formed on a Square Pyramid," *Journal of Industrial Textiles*, vol. 36, no. 3, pp. 221–226, Jan. 2007, doi: 10.1177/1528083707072354.

[12] A. Rawal, P. Potluri, and C. Steele, "Geometrical Modeling of the Yarn Paths in Three-dimensional Braided Structures," *Journal of Industrial Textiles*, vol. 35, no. 2, pp. 115–135, Oct. 2005, doi: 10.1177/1528083705057574.

[13] A. Gholami and G. W. Melenka, "Generating Geometrical Models for Tubular Braided Composites," *CSME Conference, Charlottetown, PE, Canada*, 2021.

[14] T. Alpyildiz, "3D geometrical modelling of tubular braids," *Textile Research Journal*, vol. 82, no. 5, pp. 443–453, Mar. 2012, doi: 10.1177/0040517511427969.

[15] A. Rawal, S. Gupta, H. Saraswat, and A. Sibal, “Geometrical modeling of near-net shape braided preforms,” *Textile Research Journal*, vol. 85, no. 10, pp. 1055–1064, Jun. 2015, doi: 10.1177/0040517514559587.

[16] Y. Kyosev, “Generalized geometric modeling of tubular and flat braided structures with arbitrary floating length and multiple filaments,” *Textile Research Journal*, vol. 86, no. 12, pp. 1270–1279, Jul. 2016, doi: 10.1177/0040517515609261.

[17] F. Ning, P. Potluri, W. Yu, and J. Hearle, “Geometrical modeling of tubular braided structures using generalized rose curve,” *Textile Research Journal*, vol. 87, no. 4, pp. 474–486, Mar. 2017, doi: 10.1177/0040517516632471.

[18] G. W. Melenka, B. M. Bruni-Bossio, C. Ayranci, and J. P. Carey, “Examination of voids and geometry of bio-based braided composite structures,” *IOP Conference Series: Materials Science and Engineering*, vol. 406, no. 1, p. 012012, Sep. 2018, doi: 10.1088/1757-899X/406/1/012012.

[19] C. Unlusoy and G. W. Melenka, “Flexural testing of cellulose fiber braided composites using three dimensional digital image correlation,” *Composite Structures*, vol. 230, Dec. 2019, doi: 10.1016/j.compstruct.2019.111538.

[20] H. Bale, M. Blacklock, M. R. Begley, D. B. Marshall, B. N. Cox, and R. O. Ritchie, “Characterizing Three-Dimensional Textile Ceramic Composites Using Synchrotron X-Ray Micro-Computed-Tomography,” *Journal of the American Ceramic Society*, vol. 95, no. 1, pp. 392–402, Jan. 2012, doi: 10.1111/j.1551-2916.2011.04802.x.

[21] G. W. Melenka, E. Lepp, B. K. O. Cheung, and J. P. Carey, “Micro-computed tomography analysis of tubular braided composites,” *Composite Structures*, vol. 131, pp. 384–396, Nov. 2015, doi: 10.1016/j.compstruct.2015.05.057.

[22] Y. Wang, Z. Liu, N. Liu, L. Hu, Y. Wei, and J. Ou, “A new geometric modelling approach for 3D braided tubular composites base on Free Form Deformation,” *Composite Structures*, vol. 136, pp. 75–85, Feb. 2016, doi: 10.1016/J.COMPSTRUCT.2015.09.036.

[23] G. W. Melenka and A. Gholami, “Fiber identification of braided composites using micro-computed tomography,” *Composites Communications*, vol. 27, p. 100813, Oct. 2021, doi: 10.1016/j.coco.2021.100813.

[24] X. Ji *et al.*, “Multi-scale simulation and finite-element-assisted computation of elastic properties of braided textile reinforced composites,” *Journal of Composite Materials*, vol. 48, no. 8, pp. 931–949, Apr. 2014, doi: 10.1177/0021998313480198.

[25] A. Shigang, Z. Xiaolei, M. Yiqi, P. Yongmao, and F. Daining, “Finite Element Modeling of 3D Orthogonal Woven C/C Composite Based on Micro-Computed Tomography Experiment,” *Applied Composite Materials*, vol. 21, no. 4, pp. 603–614, Aug. 2014, doi: 10.1007/s10443-013-9353-4.

[26] L. Zhang, D. Hu, R. Wang, Y. Zeng, and C. Cho, “Establishing RVE model composed of dry fibers and matrix for 3D four-directional braided composites,” *Journal of Composite Materials*, vol. 53, no. 14, pp. 1917–1931, Jun. 2019, doi: 10.1177/0021998318815735.

[27] R. Wang, L. Zhang, D. Hu, and C. Cho, “Evaluation of three unit cell models in predicting the mechanical behaviour of 3D four-directional braided composites,” *Journal of*

Composite Materials, vol. 51, no. 27, pp. 3757–3767, Nov. 2017, doi: 10.1177/0021998317692657.

[28] J. J. Gou, W. Z. Fang, Y. J. Dai, S. Li, and W. Q. Tao, “Multi-size unit cells to predict effective thermal conductivities of 3D four-directional braided composites,” *Composite Structures*, vol. 163, pp. 152–167, Mar. 2017, doi: 10.1016/j.compstruct.2016.12.034.

[29] K. Dong, J. Zhang, L. Jin, B. Gu, and B. Sun, “Multi-scale finite element analyses on the thermal conductive behaviors of 3D braided composites,” *Composite Structures*, 2016, doi: 10.1016/j.compstruct.2016.02.029.

[30] Y. H. Chen and M. H. Aliabadi, “Meshfree-based micromechanical modelling of twill woven composites,” *Composites Part B: Engineering*, p. 108190, May 2020, doi: 10.1016/j.compositesb.2020.108190.

[31] S. V. Lomov *et al.*, “Meso-FE modelling of textile composites: Road map, data flow and algorithms,” *Composites Science and Technology*, vol. 67, no. 9, pp. 1870–1891, Jul. 2007, doi: 10.1016/j.compscitech.2006.10.017.

[32] C. C. Chamis, “Mechanics of composite materials: Past, present, and future,” *Journal of Composites Technology and Research*, vol. 11, no. 1, pp. 3–14, Mar. 1989, doi: 10.1520/ctr10143j.

[33] I. Verpoest and S. V. Lomov, “Virtual textile composites software WiseTex: Integration with micro-mechanical, permeability and structural analysis,” *Composites Science and Technology*, vol. 65, no. 15-16 SPEC. ISS., pp. 2563–2574, Dec. 2005, doi: 10.1016/j.compscitech.2005.05.031.

[34] K. Xu, X. Qian, D. Duan, B. Chen, and L. Guo, "A novel macro-meso finite element method for the mechanical analysis of 3D braided composites," *Mechanics of Materials*, vol. 126, pp. 163–175, Nov. 2018, doi: 10.1016/J.MECHMAT.2018.08.007.

[35] P. Zhang, L.-J. Gui, Z.-J. Fan, Q. Yu, and Z.-K. Li, "Finite element modeling of the quasi-static axial crushing of braided composite tubes," *Computational Materials Science*, vol. 73, pp. 146–153, Jun. 2013, doi: 10.1016/j.commatsci.2013.01.026.

[36] Y.-B. Wang, Z.-G. Liu, L. Hu, and Z. Wu, "Predicting the Elastic Modulus of 3D Braided Composite Tubes Using Geometrical Mapping Approach," *21st International Conference on Composite Materials, Xi'an*, 2017.

[37] D. Zhang *et al.*, "Finite Element Analysis of Mesh Size Effect of 3D Angle-Interlock Woven Composites Using Voxel-Based Method," *Applied Composite Materials*, vol. 25, no. 4, pp. 905–920, Aug. 2018, doi: 10.1007/s10443-018-9723-z.

[38] G. W. Melenka and C. Ayranci, "Advanced measurement techniques for braided composite structures: A review of current and upcoming trends," *Journal of Composite Materials*, vol. 54, no. 25, pp. 3895–3917, Oct. 2020, doi: 10.1177/0021998320903105.

[39] J. D. Boerckel, D. E. Mason, A. M. McDermott, and E. Alsberg, "Microcomputed tomography: approaches and applications in bioengineering.," *Stem cell research & therapy*, vol. 5, no. 6, p. 144, Dec. 2014, doi: 10.1186/scrt534.

[40] D. Goyal, X. Tang, J. D. Whitcomb, and A. D. Kelkar, "Effect of various parameters on effective engineering properties of 2× 2 braided composites," *Mechanics of Advanced Materials and Structures*, vol. 12, no. 2, pp. 113–128, 2005.

[41] S. Li, S. Kyaw, and A. Jones, “Boundary conditions resulting from cylindrical and longitudinal periodicities,” *Comput Struct*, vol. 133, pp. 122–130, Mar. 2014, doi: 10.1016/J.COMPSTRUC.2013.11.017.

[42] C. Ayranci, D. Romanyk, and J. P. Carey, “Elastic properties of large-open-mesh 2D braided composites: Model predictions and initial experimental findings,” *Polymer Composites*, vol. 31, no. 12, pp. 2017–2024, Dec. 2010, doi: 10.1002/pc.20999.

[43] R. Karmankar and R. G. Karmankar, “ANALYSIS OF VON-MISES-STRESS FOR INTERFERENCE FIT AND PULL-OUT STATES BY USING FINITE ELEMENT METHOD,” *International Research Journal of Engineering and Technology*, 2018, doi: 10.13140/RG.2.2.26447.79520.

[44] Y. Kyosev, “TexMind Software.” [Online]. Available: http://texmind.com/wp/

[45] Student, “The Probable Error of a Mean,” *Biometrika*, vol. 6, no. 1, p. 1, Mar. 1908, doi: 10.2307/2331554.

Chapter 7. Conclusions and Future Work

7.1 Summary and Conclusions

In summary, this PhD thesis comprehensively explored the design, characterization, and simulation of 2D Tubular Braided Composites (TBCs).

In Chapter 3, a program named TBC-Gen was created for designing different patterns of 2D TBCs with different geometrical models. The results of this program were exported as a yarn path into SolidWorks Software to add the cross-section and create the 3D models. TBC-Gen did not require the user to have an in-depth knowledge of the equations of the TBC models, and it was user-friendly software. Different models with different patterns and shapes were designed and shown in this chapter.

Chapter 4 showed the results of the µCT scanned TBCs and used different image processing techniques to segment out the yarns and extract parameters of the model. Also, an algorithm for separating two overlapping yarns was developed. The separating algorithm was first applied to models created by TBC-Gen, and a tracing algorithm was introduced to find the relevant yarn in the following image. Then, the algorithm was used to µCT images. The results of this algorithm showed the possibility of automating the entire yarn segmentation process.

In Chapter 5, the equations used for developing the geometrical models of different patterns of TBCs were updated. The updated equations helped model the TBCs with better accuracy, matching the pattern of the manufactured TBCs. A µCT scan was done on a cured TBC, and its 3D and 2D images were produced. Then, the image processing and segmentation algorithms were applied to prepare the images for segmentation. Two yarns in different directions were selected and segmented out manually. Then, the properties of the segmented yarns were extracted automatically, and using the extracted center points, the yarn path for each yarn was generated. Other parameters of the yarn paths, like the braid angle and diameter of the mandrel, were extracted using different techniques. Finally, using the updated modelling equations and some of the extracted parameters, two yarn paths were generated and fitted to the μCT yarn paths. To increase the fit to the μCT model, a new parameter was introduced and optimized using Particle Swarm Optimization (PSO) algorithms. Finally, the Mean Square Error (MSE) between the μCT yarn path and the simulated yarn path was calculated to be less than 1%.

In Chapter 6, different Finite Element Modeling (FEM) are developed, and the TBC-Gen is used for generating the solid models of these simulations. A mesh analysis is developed, and the optimum mesh size is obtained. Also, the Periodic Boundary Condition (PBC) is used for reducing the computational expenses of the FEM. Seven TBCs with similar sizes and patterns but different braid angles are analyzed in a simulated tensile test, and the effect of braid angle on displacement is shown. Three other TBCs with similar sizes but different patterns were designed and simulated, too. The impact of the pattern on displacement is demonstrated in this chapter. Finally, the results of this chapter were compared against experimental and analytical results for validation.

Generally, the developed study proposed valuable results in modelling TBCs. It provides the tools for generating and analyzing the TBC models. More importantly, it reported for the first time how accurate these models are and how much error is incorporated into the geometrical models of TBCs. Using the results of this study, researchers can better understand the reliability of the geometrical model. It will let the researchers decide if the geometrical models are adequate for their analysis or if they want to choose more expensive and more accurate models. Also, the open-source TBC-Gen program will facilitate the work of designers and researchers to create models faster and more convenient.

Additionally, the results of the FEM show a good agreement with the experimental results. The effect of the geometrical variables will help the designers and researchers to make wiser decisions. These simulations' results are valuable initial research to expand the study for more in-depth analysis.

7.2 Recommendation for Future Work

Based on the results of this study, future work is recommended to bridge the gap in the literature.

- This research initiated the segmentation of the yarns from the µCT images. However, other methods, like machine learning algorithms, can be employed to fully automate the µCT image yarn segmentation process and extract the braids' geometrical parameters.
- Because of the similarity in the shapes and forms, the methodology presented in this work can be extended to other types of textile materials, 3D-printed structures, ropes, cables, cardiac stents, and similar products.
- The effect of braid angle and pattern type on the TBC's displacements was analyzed in this research. The effect of other geometrical variables can be studied to analyze their behaviour.
- The Mean Square Error (MSE) between a Regular pattern yarn path was compared against its geometrical model contour yarn. However, the other two patterns (Diamond and Hercules) can also be studied. Also, by increasing the number of analyzed yarns, the accuracy of the reported MSE will be improved.
- To increase the accuracy of the FEM simulation, the geometrical models generated by µCT can be used. The µCT models include less error and will provide more reliable results compared to FEM based on a simulated geometrical model. Also, a comparison between µCT based FEM and simulated geometrical model-based FEM can be carried out.

- In this research, only a tensile test was used for FEM simulation. Tension and Torsion tests can be used to analyze the TBC's performance. Also, the combination of these forces can be modelled.
- Different mechanical experimental tests can be carried out, and the FEM simulations can compare their results.
- TBC-Gen program can be improved and incorporate better visualization tools to create the 3D models independent of other solid modeling software (Solidworks).

Chapter 8. Appendix 1

8.1 Mathematical Model of the Tubular Braided Composites

Depending on the pattern of the braided composite (Diamond, Regular, and Hercules), there would be different equations to model them. However, all of them follow a helical path around the mandrel. As a result, they would have similar helical equations and curve with different undulation paths. Furthermore, there are two sets of yarns in braided composites, one counterclockwise (right-hand) and one clockwise (left-hand). Therefore, there would be two separate sets of equations with π phase shift difference between them for these models. For all the equations, X and Y represent the cross-section plane of the TBC. Also, Z represents the longitudinal axis of it (as shown in A- Figure 1).

The counterclockwise (right-hand) and clockwise (left-hand) helix's general equations for a yarn path around a cylindrical mandrel are shown in (A-1) and (A-2), respectively.

$$\begin{aligned} X_{ccw} &= R\cos\varphi \\ Y_{ccw} &= R\sin\varphi \\ Z_{ccw} &= R\,\varphi\cot\theta \end{aligned} \tag{A- 1}$$

$$\begin{aligned} X_{cw} &= R\cos\varphi \\ Y_{cw} &= -R\sin\varphi \\ Z_{cw} &= R\varphi\cot\theta \end{aligned} \tag{A-2}$$

where X_{ccw}, Y_{ccw}, and Z_{ccw} are coordinate of points for a counterclockwise helix in X, Y, and Z directions accordingly, and X_{cw}, Y_{cw}, and Z_{cw} are coordinate of points for a clockwise helix. R is the radius of the helix, φ is the winding angle, and θ is the helix angle (braid angle). The only difference between (A-1) and (A-2) is the π phase difference in Y coordinate which is shown by a negative sign in (A-2) ($\sin(\varphi + \pi) = -\sin(\varphi)$). A set of clockwise and counterclockwise helix paths with R = 15 mm, $0 < \varphi < 2\pi$, and $\theta = 30°$

are shown in A- Figure 1. A- Figure 1 a) shows the 3D model of two helix paths – one clockwise (red) and one counterclockwise (blue), A- Figure 1b) shows the top view (X-Y) of the helix paths, which would be relevant to the cross-section view of the mandrel used for the TBC, and A- Figure 1 c) shows the right plane (X-Z) of the helix path where the helix angle is relevant to the braid angle.

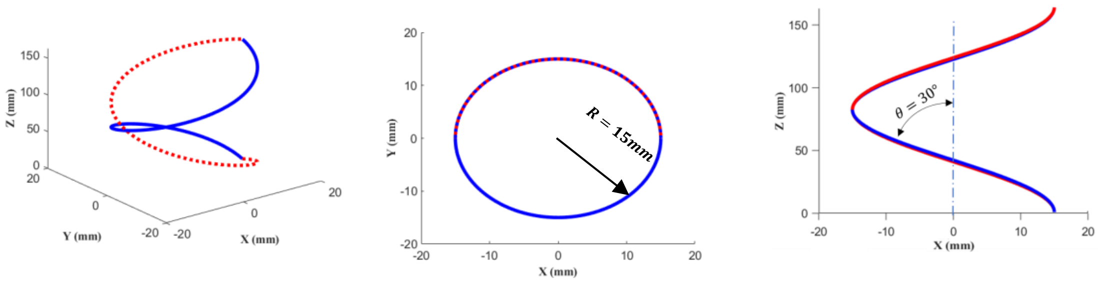

a) b) c)

A- Figure 1 A counterclockwise (right-hand) (blue) and a clockwise (left-hand) (red) helix path with R = 15 mm and $\theta = 30°$ for one period ($0 < \varphi < 2\pi$). a) the 3D view, b) the top view, and c) right (x-z) view

On the other hand, each yarn path follows a sinusoidal path based on its braiding pattern. The equation relating the number of yarns, the radius of the strand, and the winding angle to the sinusoidal yarn path is shown in (A-3) [11].

$$S(\varphi) = r \sin\left(\frac{N\varphi}{2}\right) \tag{A-3}$$

Where r is the radius of the yarn and N is the total number of yarns. One of the undulation paths of a set of a sinusoidal path with r = 0.7 mm, N = 4, and $0 < \varphi < 2\pi$ is shown in A- Figure 2.

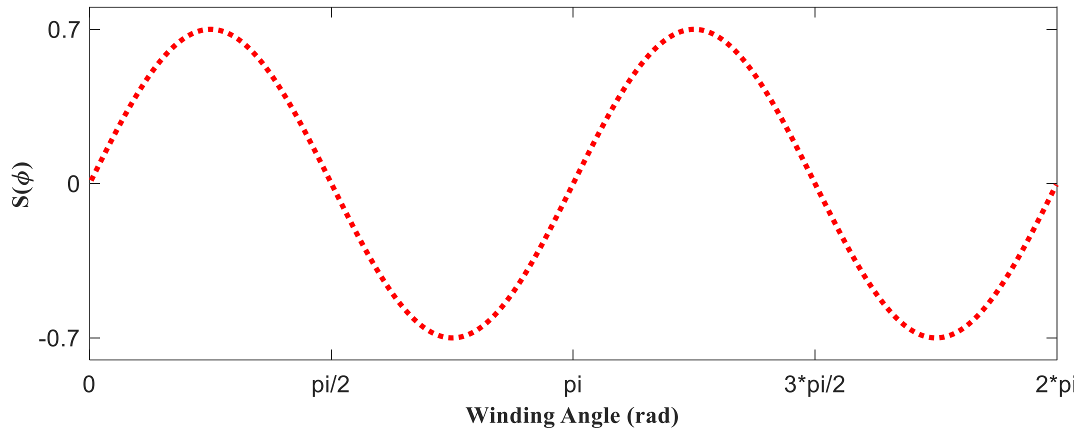

A- Figure 2 General sinusoidal paths of a yarn path with $r = 0.7\ mm$, $N = 4$, and $0 < \varphi \leq 2\pi$

For having the complete yarn path of braided composite, with helix shape and including the undulations, equations (A-1) and (A-2) should be mixed with equation (A-3). By doing so, equations (A-4) and (A-5) are created for counterclockwise and clockwise yarn paths, respectively.

$$\begin{aligned} X_i &= \big(R + S_1(\varphi)\big)\cos(\varphi + (i-1)\omega) && i = 1,2\dots n \\ Y_i &= \big(R + S_1(\varphi)\big)\sin(\varphi + (i-1)\omega) && i = 1,2\dots n \\ Z_i &= R\varphi\tan\theta && i = 1,2\dots n \end{aligned} \qquad \text{(A-4)}$$

$$\begin{aligned} X_i &= \big(R + S_2(\varphi)\big)\cos(\varphi + (i-1)\omega) && i = 1,2\dots n \\ Y_i &= -\big(R + S_2(\varphi)\big)\sin(\varphi + (i-1)\omega) && i = 1,2\dots n \\ Z_i &= R\varphi\tan\theta && i = 1,2\dots n \end{aligned} \qquad \text{(A-5)}$$

Where n is the number of the braiding yarns revolving in the same direction (i.e., $n = N/2$), i is the counter defining the actual braiding yarn revolving in the same direction, and ω is the shift angle which is calculated as the angle between every two strands (i.e., ω =2π/n). These equations are the same for all patterns of TBC. The only factor making the difference for each yarn pattern is $S_1(\varphi)$ and $S_2(\varphi)$ which will be discussed in the following sections.

8.1.1 Diamond Pattern

The Diamond pattern is the most straightforward pattern of the TBC because the whole path is sinusoidal, and no flat section is incorporated into the path. The $S_1(\varphi)$ and $S_2(\varphi)$, representing the counterclockwise and clockwise sinusoidal paths respectively are as follows:

$$S_1(\varphi) = r\sin\left(\frac{N\varphi}{2} + \frac{\pi}{2}\right) \tag{A-6}$$

$$S_2(\varphi) = -r\sin\left(\frac{N\varphi}{2} + \frac{\pi}{2}\right) \tag{A-7}$$

A sample of the sinusoidal path of Diamond pattern with $r = 0.7\ mm$, $N = 2$, and $0 < \varphi \leq 2\pi$ is shown in A- Figure 3.

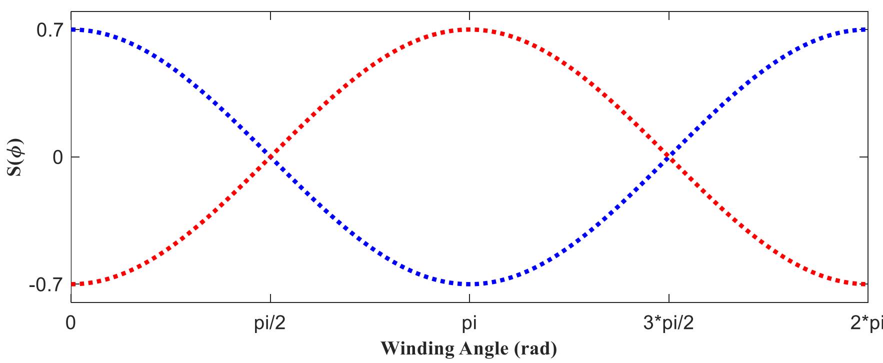

A- Figure 3 Counterclockwise (blue) and clockwise (red) undulation path of Diamond pattern

By adding equations (A-6) and (A-7) to (A-4) and (A-5), the equations for the 3-D path of the Diamond pattern will be generated. A sample of Diamond TBC yarn path (counterclockwise and clockwise) with $N = 32$, $R = 10$ mm, $r = 0.5$ mm, and $\theta = 45°$ is shown in A- Figure 4 (only one of the yarn at each direction is shown for more clarity). The radius of the mandrel is ($R_m = R - 2r$).

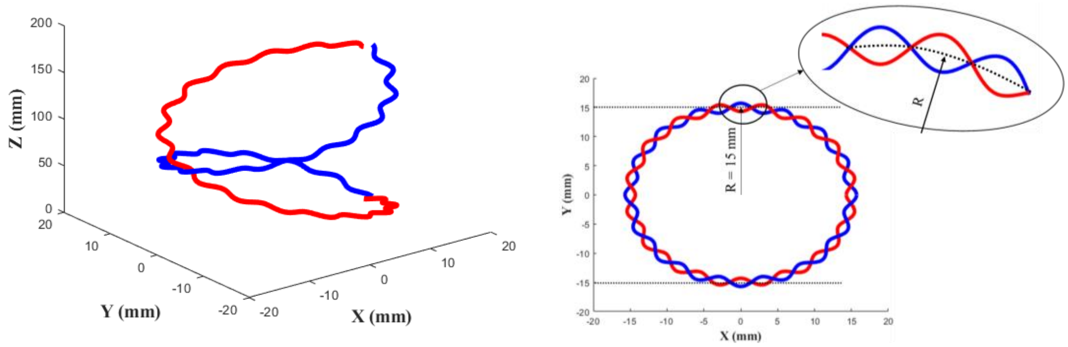

A- Figure 4 Clockwise (red) and counterclockwise (blue) yarn path of Diamond patterns with $N = 32$, $R = 15\ mm$, r=0.7 mm, and α=30° (only one set of yarns are shown)

8.1.2 Regular Pattern

The shape of the Regular pattern is based on the Diamond pattern. Each yarn passes over two yarns moving in the other direction and under two others in the Regular pattern. Because of that, the Regular pattern involves a flat section for the distance between yarns. However, the transient area-going from the top of two yarns to the under the two next and vice versa- is still covered by the sinusoidal equations shown in the previous section. A sample of Regular undulation paths with $r = 0.7\ mm$, $N = 4$, and $0 < \varphi \leq 2\pi$ is shown in A- Figure 5.

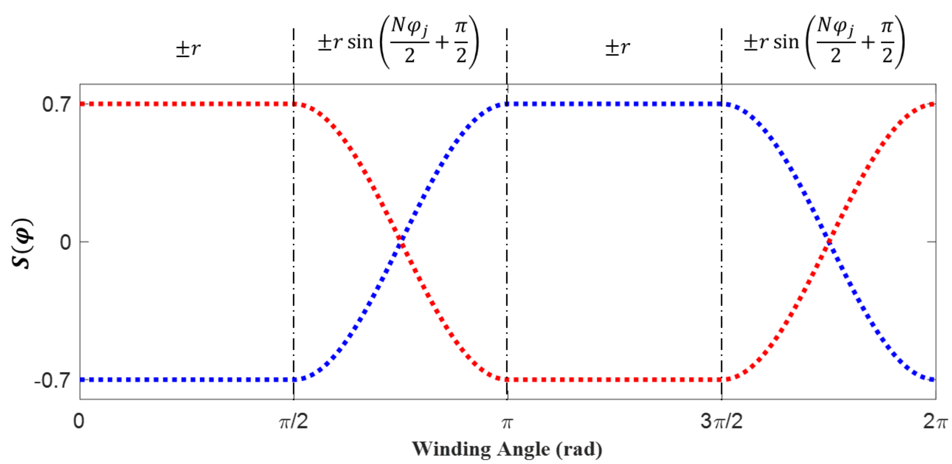

A- Figure 5 Counterclockwise (blue) and clockwise (red) undulation path of Regular pattern with $r = 0.7\ mm$, $N = 4$, and $0 < \varphi \leq 2\pi$

For generating the Regular yarn path, a set of piecewise equations as shown in equations (A-8) to (A-11) should be used. In addition, to make the ridges parallel to the axis of the TBC, two more piecewise equations, compared to the Diamond pattern, with π degree phase difference should be added. Therefore, there would be two sets of equations for counterclockwise undulation (A-8 and A-9) and two sets of equations for clockwise undulations (A-10 and A-11).

$$S_{1a}(\varphi_j) = \begin{cases} r\sin\left(\frac{N\varphi_j}{2}+\frac{\pi}{2}\right) & ; 0 \le \varphi_j < \theta/2 \\ -r & ; \theta/2 \le \varphi_j < \theta \\ -r\sin\left(\frac{N\varphi_j}{2}+\frac{\pi}{2}\right) & ; \theta \le \varphi_j < 3\theta/2 \\ r & ; 3\theta/2 \le \varphi_j < 2\theta \end{cases} \quad \text{(A-8)}$$

$$S_{1b}(\varphi_j) = \begin{cases} -r\sin\left(\frac{N\varphi_j}{2}+\frac{\pi}{2}\right) & ; 0 \le \varphi_j < \theta/2 \\ r & ; \theta/2 \le \varphi_j < \theta \\ r\sin\left(\frac{N\varphi_j}{2}+\frac{\pi}{2}\right) & ; \theta \le \varphi_j < 3\theta/2 \\ -r & ; 3\theta/2 \le \varphi_j < 2\theta \end{cases} \quad \text{(A-9)}$$

$$S_{2a}(\varphi_j) = \begin{cases} -r & ; 0 \le \varphi_j < \theta/2 \\ r\sin\left(\frac{N\varphi_j}{2}+\frac{\pi}{2}\right) & ; \theta/2 \le \varphi_j < \theta \\ r & ; \theta \le \varphi_j < 3\theta/2 \\ -r\sin\left(\frac{N\varphi_j}{2}+\frac{\pi}{2}\right) & ; 3\theta/2 \le \varphi_j < 2\theta \end{cases} \quad \text{(A-10)}$$

$$S_{2b}(\varphi_j) = \begin{cases} r & ; 0 \le \varphi_j < \theta/2 \\ -r\sin\left(\frac{N\varphi_j}{2}+\frac{\pi}{2}\right) & ; \theta/2 \le \varphi_j < \theta \\ -r & ; \theta \le \varphi_j < 3\theta/2 \\ r\sin\left(\frac{N\varphi_j}{2}+\frac{\pi}{2}\right) & ; 3\theta/2 \le \varphi_j < 2\theta \end{cases} \quad \text{(A-11)}$$

Where $j = 0,1,2, \dots length(\varphi)$.

By combining equations (A-8) and (A-9) with equations (A-4) and equations (A-10) and

(A-11) with equation (A-5), the yarn path of the Regular pattern will be achieved. Equations (A-4 and A-5 should be adopted based on the two new sets of equations as well). A sample of braid yarn with a Regular pattern, with $N = 32$, $\alpha = 60°$, $R = 11.4\ mm$, and $r = 0.7\ mm$ is shown in A- Figure 6 (only one of the yarn at each direction is shown for more clarity).

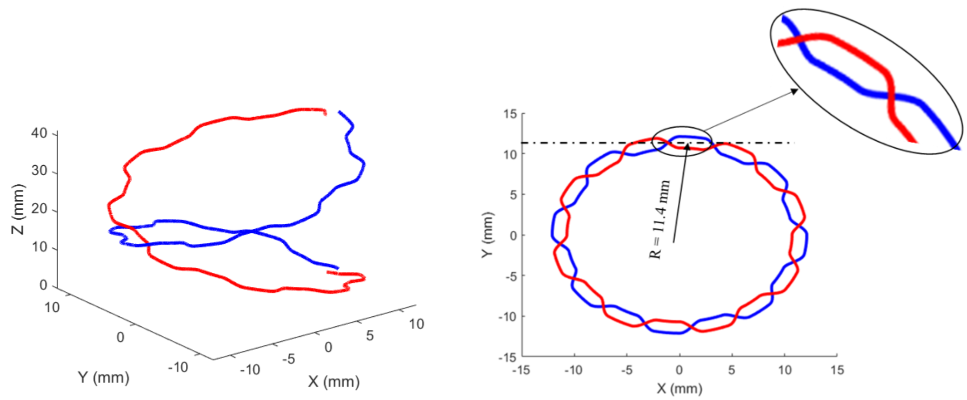

A- Figure 6 Clockwise (red) and counterclockwise (blue) yarn path of Regular pattern with $N = 32$, $R = 11.4\ mm$, $r = 0.7\ mm$, and $\theta = 60°$ (only one set of yarns are shown)

8.1.3 Hercules Pattern

Hercules pattern is similar to Regular and Diamond patterns in terms of the sinusoidal and flat section. However, since in the Hercules pattern, a yarn passes above three yarns and then goes under the next three yarns, the flat section is two times longer than the Regular pattern. A sample of counterclockwise and clockwise undulation path of Hercules pattern with $r = 0.7\ mm$, $N = 8$, and $0 < \varphi \leq 2\pi$ is shown in A- Figure 7. As one can see, the flat sections are twice longer than the Regular pattern. The sinusoidal undulations are the same as for Regular and Diamond patterns.

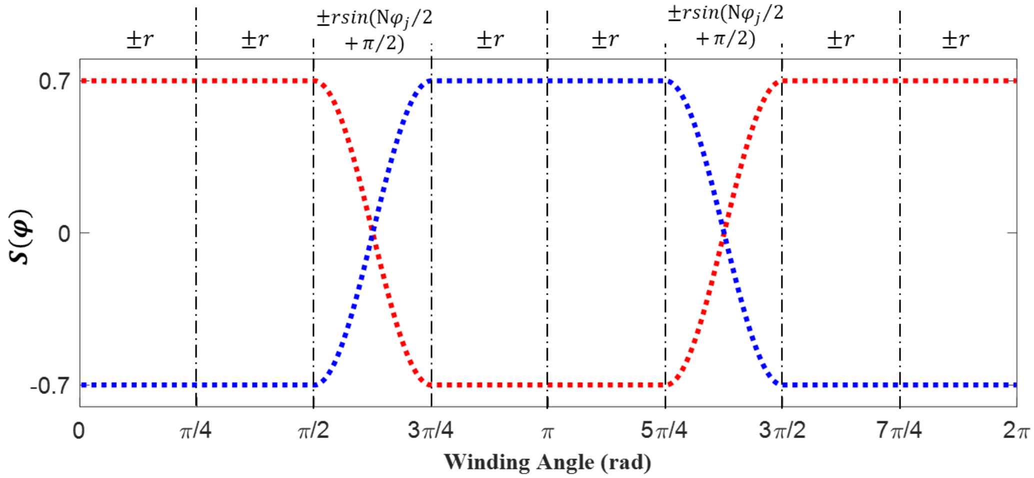

A- Figure 7 Counterclockwise (blue) and clockwise (red) undulation path of Hercules pattern with $r = 0.7\ mm$, $N = 8$, and $0 < \varphi \leq 4\pi$

The counterclockwise and clockwise equations for the Hercules pattern's undulation path are shown in (A-12) and (A-13), respectively.

$$S_1(\varphi_j) = \begin{cases} r & ; 0 \leq \varphi_j < \omega/2 \\ r & ; \omega/2 \leq \varphi_j < \omega \\ r\sin\left(\dfrac{N\varphi_j}{2} + \dfrac{\pi}{2}\right) & ; \omega \leq \varphi_j < 3\omega/2 \\ -r & ; 3\omega/2 \leq \varphi_j < 2\omega \\ -r & ; 2\omega \leq \varphi_j < 5\omega/2 \\ r\sin\left(\dfrac{N\varphi_j}{2} + \dfrac{\pi}{2}\right) & ; 5\omega/2 \leq \varphi_j < 3\omega \end{cases} \tag{A-12}$$

$$S_2(\varphi_j) = \begin{cases} -r & ; 0 \leq \varphi_j < \omega/2 \\ -r & ; \omega/2 \leq \varphi_j < \omega \\ -r\sin\left(\dfrac{N\varphi_j}{2} + \dfrac{\pi}{2}\right) & ; \omega \leq \varphi_j < 3\omega/2 \\ r & ; 3\omega/2 \leq \varphi_j < 2\omega \\ r & ; 2\omega \leq \varphi_j < 5\omega/2 \\ -r\sin\left(\dfrac{N\varphi_j}{2} + \dfrac{\pi}{2}\right) & ; 5\omega/2 \leq \varphi_j < 3\omega \end{cases} \tag{A-13}$$

Similar to Diamond and Regular pattern equations, by combining equations (A-12) and (A-13) by equations (A-4) and (A-5), the equations for the Hercules pattern will be achieved.

A sample of Hercules pattern with $N = 32$, $\gamma = 60°$, $R = 12\ mm$, and $r = 0.7\ mm$ is shown in A- Figure 8 (only one of the yarn at each direction is shown for more clarity).

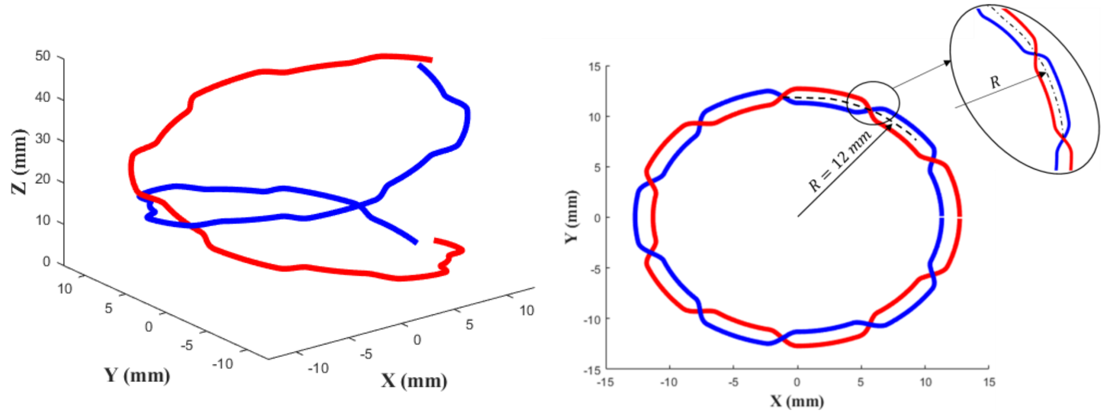

A- Figure 8 Clockwise (red) and counterclockwise (blue) yarn path of Hercules pattern with N=32, R=12 mm, r=0.7 mm, and γ=60° (only one set of yarns are shown